JUSTUS-LIEBIG-
UNIVERSITÄT
GIESSEN

Exploring the Perilipin2 cell lineage during murine lung alveolarization

Inaugural Dissertation

zur Erlangung des Grades Doktor der Naturwissenschaften
(Dr. rer. nat.)
der naturwissenschaftlichen Fachbereiche (Fachbereich 08 Biologie und Chemie) der
Justus-Liebig-Universität Gießen

vorgelegt von
Solmaz Khaghani Raziabad
aus Teheran, Iran

Gießen, 2023

From the Max-Planck-Institute for Heart and Lung Research

Department IV Lung Development and Remodelling

Director: Prof. Dr. med. Werner Seeger of the Faculty of Medicine of the Justus-Liebig-Universität Gießen

Supervisors:

Prof. Dr. Werner Seeger

Prof. Dr. Ivan Manzini

Table of content

Table of content ***1***

1 Introduction ***4***

1.1 Overview of lung evolution *4*

1.2 Respiratory system and lung anatomy in human and mice *4*

1.3 Lung development in mice and human *6*

1.4 Structural lung diseases *7*

1.5 Alveolarization *9*

1.6 Cellular composition of the alveolar region during late lung development *10*

1.6.1 The epithelial cell lineage of alveolar niche *11*

1.6.2 The endothelial cell lineage of the alveolus *12*

1.6.3 Mesenchymal cell types of the alveolar niche during alveolarization *13*

1.6.4 Myofibroblasts during alveolarization *14*

1.6.5 Lipofibroblasts *16*

1.6.6 Perilipin2 (Plin2) *17*

1.7 Single cell RNA sequencing (scRNAseq) *18*

2 Hypothesis ***20***

3 Aims of the study ***20***

4 Materials and Methods ***21***

4.1 Technical equipment *21*

4.2 Consumables *22*

4.3 Reagents and drugs *23*

4.4 Software *25*

4.5 Primary and secondary antibodies *26*

4.6 Approvals for animal experimental studies *26*

4.7 Mouse lines *27*

4.7.1 C57BL/6J wild type mice *27*

4.7.2 Plin2$^{tm1.1\ (Cre/ERT2)\ Mort}$ *27*

4.7.3 Gt (R26)26Sor$^{tm4\ (ACTB\text{-}tdTomato,\ EGFP)\ Luo/J}$ ... 28
4.7.4 B6.129P2-Gt (R26)26Sor$^{tm1\ (DTA)\ Lky/J}$ line ... 28
4.7.5 Plin2$^{tm1.1\ (Cre/ERT2)\ Mort}$; B6.129P2-Gt (R26)26Sor$^{tm1\ (DTA)\ Lky/J}$ line ... 28
4.7.6 Plin2$^{tm1.1\ (Cre/ERT2)\ Mort}$; Gt (R26)26Sor$^{tm4\ (ACTB\text{-}tdTomato,\ -EGFP)\ Luo/J}$ line ... 29
4.8 Genotyping of transgenic mice ... 29
4.9 Genotyping PCR and DNA electrophoresis ... 30
4.10 Tamoxifen administration ... 32
4.11 Paraffin tissue processing ... 32
4.12 Elastica staining ... 33
4.13 Hematoxylin and Eosin staining ... 33
4.14 Total RNA isolation and real-time PCR ... 34
4.15 Flow cytometry ... 36
4.16 Lung isolation and preparation of cell suspension ... 36
4.17 Immunofluorescent labeling for flow cytometry ... 36
4.18 Preparation of precision-cut lung slices from fixed organs ... 37
4.19 Immunofluorescent staining of PCLS ... 37
4.20 Image processing, analysis and figures preparation ... 38
4.21 ScRNAseq sample preparation and data analysis ... 38
4.22 Statistics ... 39
5 Results ... 40
5.1 Depletion of Plin2^{+} cells using Plin2^{creERT2}; R26^{DTA} mice ... 40
5.1.1 Depletion of Plin2^{+} cells during postnatal lung development ... 40
5.1.1.1 Morphology of lungs, liver, kidneys and spleen of Plin2^{+} cell depleted neonatal mice ... 40
5.1.1.2 Quantitative analysis of Plin2^{+} cell depletion in postnatal lungs ... 44
5.1.1.3 Gene expression analyses of lungs and livers from Plin2^{+} cell depleted and control neonatal mice ... 45
5.1.2 Depletion of Plin2^{+} cells in adult mice ... 50
5.2 Labeling of the Plin2^{+} cell lineage in adult mice ... 54
5.2.1 Characterization of lung cells of Plin2 cell lineage by scRNAseq at P7 and P14 ... 56
5.2.2 Plin2^{lin} contribution to alveolar epithelial cell subpopulations ... 59

5.2.2.1 Molecular signatures of alveolar epithelial type II cells at P1 64

5.2.3 Validation of scRNAseq based gene expression in cell clones derived from the Plin2 lineage at the peak of alveolarization 66

5.2.4 Single-cell transcriptomic profile of Plin2^{lin} derived endothelial cells 68

5.2.5 Identification of a Plin2^{lin} derived myofibroblast population. 70

5.2.6 Molecular signatures of Plin2^{lin} derived lipofibroblasts. 73

6 Discussion 80

6.1 Depletion of Plin2 expressing cells in mice during lung development and adulthood 80

6.2 Lineage tracing of Plin2^{+} cells in mice in the adult lung and liver 82

6.3 Molecular signatures and contribution of Plin2^{lin} cells during alveolarization 82

6.3.1 Identification of Plin2^{lin} derived cell clusters 83

6.3.2 Non-mesenchymal cell clusters of P1 Plin2^{lin} cells during alveolarization 84

6.3.3 Contribution of Plin2^{lin} cells to mesenchymal cell populations during alveolarization 86

7 Conclusion 89

8 Summary 90

9 Zusammenfassung 91

10 Bibliography 93

11 Appendix 108

12 List of figures 114

13 List of tables 116

14 List of gene names 117

15 Abbreviations 119

16 Curriculum vitae ..... Error! Bookmark not defined.

17 Acknowledgments 123

18 Declaration 124

1 Introduction

1.1 Overview of lung evolution

Lung is the most important organ of respiratory system. It is an air-breathing organ which evolved first about 419-359 million years ago in Paleozoic period as a crucial evolutionary adaptation in transition of life from water to land. It is believed that lungs of today's terrestrial vertebrates have developed from simple sacs, as outpocketings of esophagus, which allowed early fish to swallow the air in hypoxic conditions (Cupello et al., 2022). The lungs of vertebrates range from simple saclike structures found in Dipnoi (lungfishes) to most efficient alveolar form in birds and mammals. Increasing subdivision of airways and development of greater surface area at the exchange surfaces appear to be the general evolutionary trend among higher vertebrates (Carvalho and Gonçalves, 2011). In human, daily breath transfers about 9000 liters of air into the lungs to deliver oxygen to and remove carbon dioxide from circulation. This crucial process is called gas exchange. Therefore, mammalian respiratory anatomic compartments and lungs are peculiarly configured to efficiently accomplish this tremendous demand (Tomashefski and Farver, 2008).

1.2 Respiratory system and lung anatomy in human and mice

The respiratory system comprises upper (nose, pharynx and larynx) and lower (trachea and lungs) compartments in both human and mice (Smith et al., 2021). There are also important anatomical, functional and structural differences between human and mice lung. The human lung has a tidal volume of ~ 6 liters, which is 6000 times of lung volume in mice. The provided surface area for gas exchange is about 70 m^2, compared to 82 cm^2 in mice (Weibel and Gomez, 1962). Human has 23 generations of the airways, compared to 13 generations in mice. The alveolar diameter and septa thickness are respectively 210 µm and 0.62 µm in human, while these values are 80 µm and 0.32 µm in mice.

Lung, a paired organ, is a part of the lower respiratory system, which is located in the thorax, surrounded by visceral pleura, and bordered with diaphragm. In the pleural cavity, the lungs are in contact with pleural fluid, which serves as a sliding film on one side and as an adhesive on the other. Its intricate, spongy, network-like, and elastic form enables the lung to function as a cohesive unit. Indeed, lung is the principal

component of the respiratory system, but its proper functioning depends on its interactions with other compartments of the respiratory system.

The lower respiratory system is comprised of two components with structural and functional differences: the conducting tracts (airways) and the respiratory zone (parenchyma). The airways deliver air via a pipe-like, branched structure (trachea, bronchi, and bronchioles) to the respiratory zone, which consists of respiratory bronchioles, alveolar ducts, and alveoli (Meyerholz et al., 2018).

The trachea is the most proximal part of the lower respiratory system, composed of 15-20 incomplete C-shaped rings in human and 15-18 in mouse. These cartilaginous rings support the trachea from collapsing. At its proximal end, the trachea connects to the larynx, while at the distal part, in a place called the "carina", it bifurcates into the left and right main bronchi, which in mouse are called extrapulmonary bronchi. Each bronchus, along with the pulmonary vessels, enters either of the lungs at a central recession called the hilum. Immediately after the entrance of the left and right bronchi into the lungs, they bifurcate into bronchioles, which are intrapulmonary bronchi in mice (Meyerholz et al., 2018).

Gross anatomy of the lung differs between human and mice. Human left and right lungs formed from two and three lobes respectively, however, in mice, the left lung is single-lobed and right lung consists of four lobes. Therefore, the bronchi dividing pattern in human and mice exclusively follows the number of lobes in each species. The conductive bronchioles undergo continuous dichotomous branching in human (Isaacson et al., 2017) and monopodial branching in mice. After ~ 25 generations of division in human, the terminal respiratory bronchioles are formed which are the most distal part of conductive zone with complete lack of cartilage. In mice, respiratory bronchioles are absent and terminal bronchioles often divide directly to alveolar ducts. The formation of alveolar ducts, alveolar sacs and lastly alveoli complete the most distal parts in this respiratory hierarchy. The parenchyma as the actual respiratory zone with the task of gas exchange contains 18 % of total lung volume in mice, which is equivalent to 12 % in human. (Harkema et al., 2013; Meyerholz et al., 2018; Tomashefski and Farver, 2008).

Despite the similarities between human and mice lungs, the differences in their gross anatomy, tissue features, and compositions are remarkable. These differences provide

adaptations to the physiological demands and ensure that respiration occurs smoothly despite the massive dynamic range, with human taking 16 breaths per minute and mouse taking 250-350 breaths per minute.

Table. 1. Comparative respiratory system in human and mice. The table is adapted from (Plopper and Hyde, 2008; Suarez et al., 2012).

	Feature	**Mouse**	**Human**
Gross anatomy	Lung lobes	4 right, 1 left	3 right, 2 left
	Airway generations	13-17	17-21
	Airway branching pattern	Monopodial	Dichotomous
	Diameter, main bronchus (mm)	1	10-15
Tissue	Diameter, terminal bronchiole (mm)	0.01	0.6
	Respiratory bronchioles	None or one	Yes
	Lung parenchyma/total lung volume (%)	18	12
	Alveoli (μm)	39-80	200-400
	Blood-gas barrier thickness (μm)	0.32	0.62

1.3 Lung development in mice and human

Lung development in mammals is a complex but highly coordinated process regulated by a considerable number of signals and pathways. Lung development can be divided into three main periods: (i) organogenesis, (ii) fetal lung development and (iii) postnatal lung development. Lung embryonic development starts with the formation of lung buds from the foregut at gestational day 26 in human and embryonic day (E) 9 in mice. At the end of week 7 in human (E12.5 in mice), the lung enters the pseudoglandular stage, which is the first step in fetal development and is characterized by the initiation of epithelial cell differentiation and the formation of the bronchial tree and terminal bronchioles (in human, this occurs between weeks 6-17 and in mice, between E12.5-E16.5). Fetal lung development continues with the canalicular stage, which occurs between 16-26 weeks in human. During this stage, formation of conductive airways is completed. Then parenchymal differentiation and massive capillarization then begin (in mice, this occurs between E16.5-E17.5) (deMello and Reid, 2000). In the saccular phase, week 26-36 in human fetal period, terminal ducts narrows and formed clusters of air sacs, which are the precursor of the future alveoli. At this step, endoderm begins

to differentiate into specialized alveolar epithelial type I and type II cells (in mice E18.5-P5).

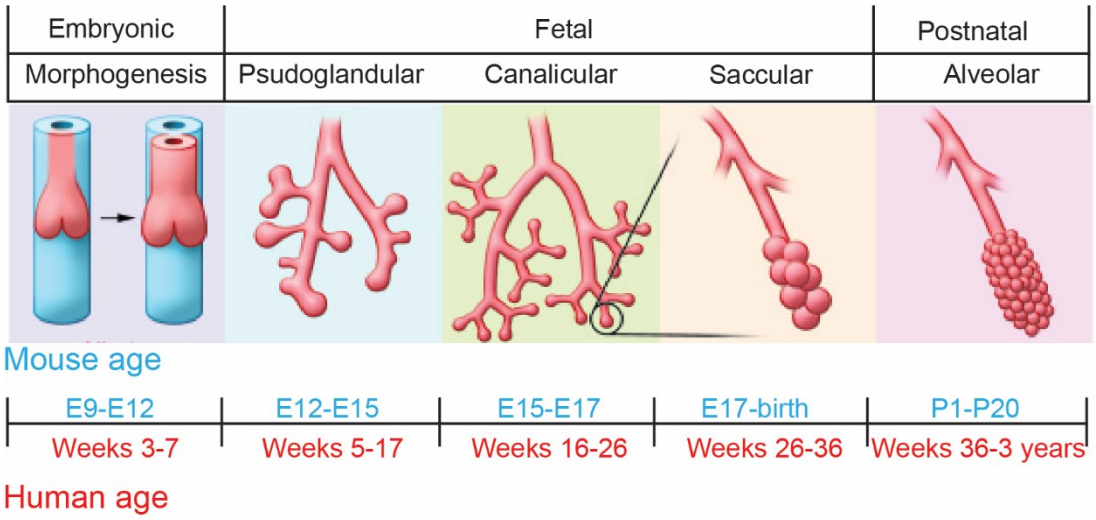

Figure 1. Lung development. Lung development in both mice and human progresses through five overlapping phases based on successive branching. The mouse lung is at saccular phase at birth while human lung is at alveolar phase at birth (week 40). Adapted and modified from (Rackley and Stripp, 2012).

At birth, human lung is already in the alveolar stage, in which lung is functional but still structurally immature. In contrast, mice are born in the saccular phase and the final step of lung development, the alveolarization phase, is completed after birth. Therefore, mice represent a perfect model to study alveolarization, since alveolarization takes place postnataly.

1.4 Structural lung diseases

Lung diseases such as chronic lung disorders (e.g. bronchopulmonary dysplasia (BPD) and chronic obstructive pulmonary disease (COPD) with emphysema and interstitial lung diseases (e.g. pulmonary fibrosis) are characterized by structural alteration in the lung parenchyma. Changes in the alveolar region (BPD & COPD) and in the interstitium (fibrosis) disrupt gas exchange and lead to respiratory failures in the patients. BPD is a chronic lung disease with a prevalence in preterm infants (born before 36 weeks of gestation). Oxygen supplementation and mechanical ventilation in these premature newborns cause the total arrest of alveolarization and consequently simplified alveolar structure with fewer and larger alveoli, decreased blood-air-barrier

for gas exchange and thickening of the septa (Kinsella et al., 2006; Lignelli et al., 2019; Silva et al., 2015). COPD is a global respiratory disease with high morbidity and mortality. It is a heterogeneous disease with various clinical manifestations. Briefly, chronic and systemic inflammation cause obstruction of small airways due to collapse of peripheral airways and consequently progressive irreversible airflow limitation (Barnes, 2014, 2016). Emphysematous parenchyma is also a histopathological phenotype observed in COPD patients, which is defined by abnormal permanent enlargement of the air spaces distal to the terminal bronchioles, accompanied by destruction of alveolar walls (Barnes, 2017; Doherty et al., 2023). Emphysema is the result of deficient alveolar regeneration after injury (Plantier et al., 2007). Alveolar mesenchymal fibroblast may play a role in alveolar multiplication and regeneration and it has been shown that the elevated extracellular matrix (ECM) is associated to increased number of myofibroblasts (Annoni et al., 2012; Löfdahl et al., 2011). Idiopathic pulmonary fibrosis (IPF) is a lethal chronic lung disease with a lifespan of 3-5 years in patients after diagnosis. This heterogeneous disease with patchy fibroblastic foci phenotype is the result of destruction of lung parenchyma and architecture which leads to impaired gas exchange and finally respiratory failure (Glass et al., 2022). A combination of genetic, epigenetic and environmental factors are introduced for IPF, although a general paradigm is common among most IPF cases. Constant micro-injuries to aging alveolar epithelium initiate aberrant epithelial-fibroblast communication, which provoke excessive ECM deposition in the interstitium by activated myofibroblasts. (El Agha, 2017; Lingampally et al., 2020; Richeldi et al., 2017). Recent genomic studies have proposed a re-capitulation developmental program as a regenerative response to aberrant IPF tissue remodeling (Chanda et al., 2016). Altogether, stunted alveoli in BPD, disrupted alveoli wall and enlargement of the air space in COPD and finally the thickening blood-air-barrier in IPF; all are characterized by aberrant alveolar structure. Therefore, understanding of the formation of alveoli and involved cellular and molecular compartments could help unraveling pathomechanisms of these diseases and discover new therapeutic strategies (Rodríguez-Castillo, 2018).

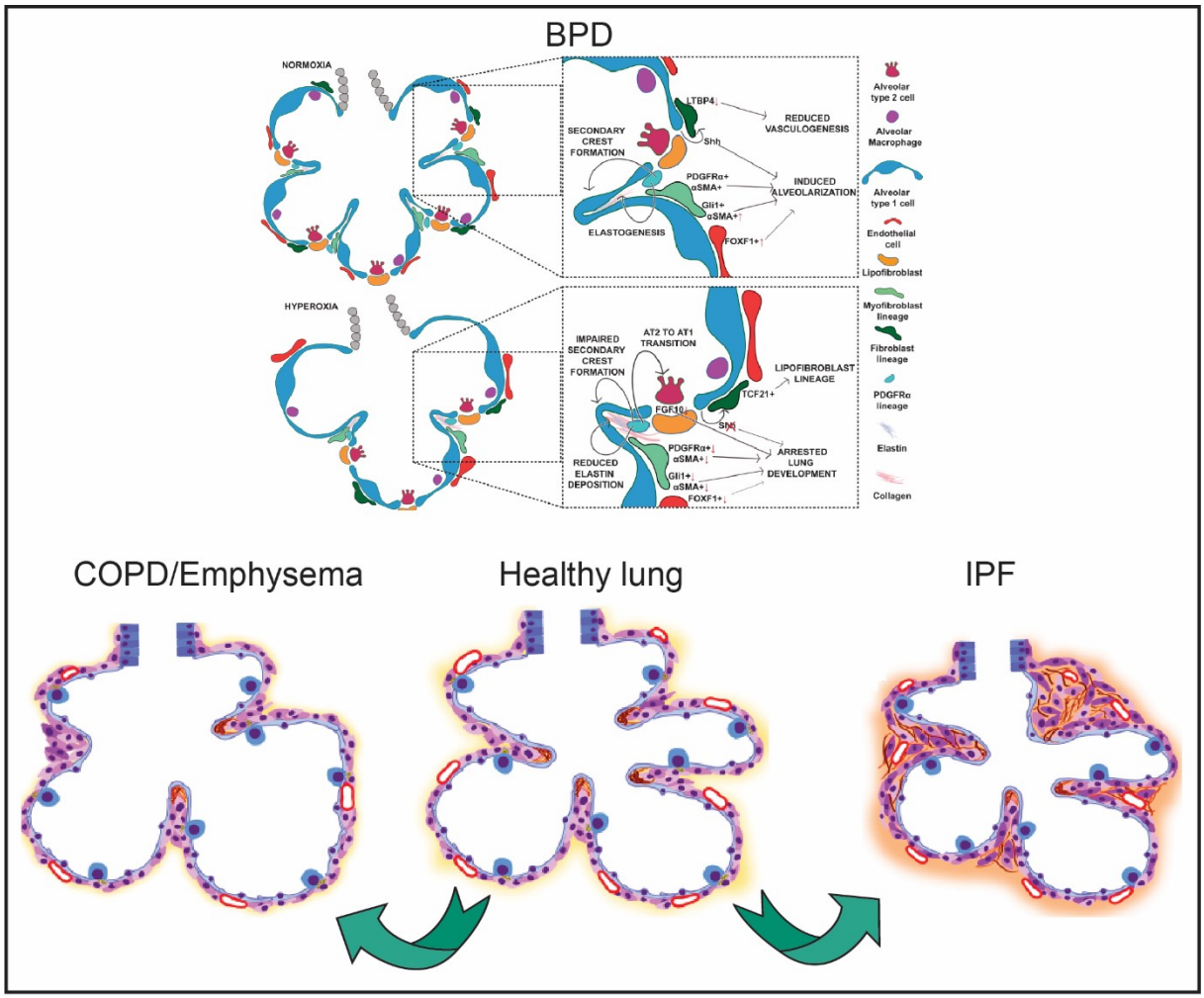

Figure 2. Schematic illustration of diseases with aberrant morphology of the alveolar region. Adopted from (Lignelli et al., 2019; Rodríguez-Castillo, 2018).

1.5 Alveolarization

Alveolarization (in mice ~ P5-P21 and after week 36 in human) is the final stage of lung maturation and refers to subdivisions of alveolar region into smaller units named “Alveoli”. This process has been described intensively in mice (Mund et al., 2008), rats (Tschanz et al., 2014) and human (Herring et al., 2014; Nikolić et al., 2018). Although there are considerable anatomical differences in murine and human lungs. The process of alveolarization is following similar structural changes. However, the time of its occurrence varies between the species (Thurlbeck, 1982; Zeltner and Burri, 1987). Therefore, mice represent a perfect tool to study alveolarization. In particular, alveolarization starts at the saccular stage in both human and mice. It peaks at P7 and structure is completed at P14 but alveolarization process and microvascular maturation

are continued after P14 in mice (Schittny, 2017). End of alveolarization is still not completely clear in human (Herring et al., 2014). The number of alveoli is estimated in an adult mouse $2.31*10^6$ and in an adult person 300 million alveoli out of which only 10 % are formed in human uterus (less than 20 million) (Knust et al., 2009; Thurlbeck, 1982; Weibel, 1979) . Generally, alveolar formation has been divided into two phases. The first phase is called “secondary septation” and the second phase is marked as remodeling of the alveolar wall “Vasculature maturation” (Mund et al., 2008). At birth, thin-walled primary septa enlarge and become completely wrapped in a capillary bilayer. When these airspaces reach to a sufficient size, protrusions lift off from pre-existing primitive septa perpendicularly into the airspace to form alveoli. This step already increases surface area enormously and is known as so-called “secondary septation” (Massaro and Massaro, 1996; McGowan, 2014). The sudden and massive appearance of the alveoli in the parenchyma has been termed “bulk alveolarization” (Burri, 2006). Both primary and secondary septa do still not resemble the adult interalveolar septa, since they are still immature and possess double-layered capillary (Joshi and Kotecha, 2007). Therefore to optimized gas exchange, this double layered capillary network is reduced into a single layered one under a process called microvasculature maturation (Roth-Kleiner et al., 2005). The process of alveolarization is orchestrated by different cellular lineages (Figure 3).

1.6 Cellular composition of the alveolar region during late lung development

Lung parenchyma consists of a large collection of roughly spherical units, the alveoli. The formation of alveoli is achieved by the interconnection of endoderm and mesoderm. This cooperation requires intricate interactions between a myriad of cell types during lung development. (Zepp and Morrisey, 2019).

In total, more than 40 different cell types reside in the lung with specific origins, phenotypes and functions (Suki et al., 2011; Yuan, 2018). Although, there are structural differences, cell composition of alveolar niche between human and mice, seems to be relatively similar (Basil and Morrisey, 2020). The internal surface of alveoli is paved with an epithelial cell layer and septal walls are further composed of interstitial cells and ECM (Suki et al., 2011). In addition to the epithelial cell lineage, the parenchyma of the lung is composed of other cell lineages such as, mesenchymal, endothelial and hematopoietic cell lineages. Practically, the epithelial cell lineage is

marked by the surface markers Cadherin 1 or Epcam (CD 326); the endothelial lineage by Cadherin 5 and Pecam-1 (CD31) and Intercellular adhesion molecule 2; the hematopoietic lineage by Protein tyrosine phosphatase receptor type C (CD45) and the mesenchymal lineage, which is negative for markers of the other three lineages (Vila Ellis and Chen, 2021).

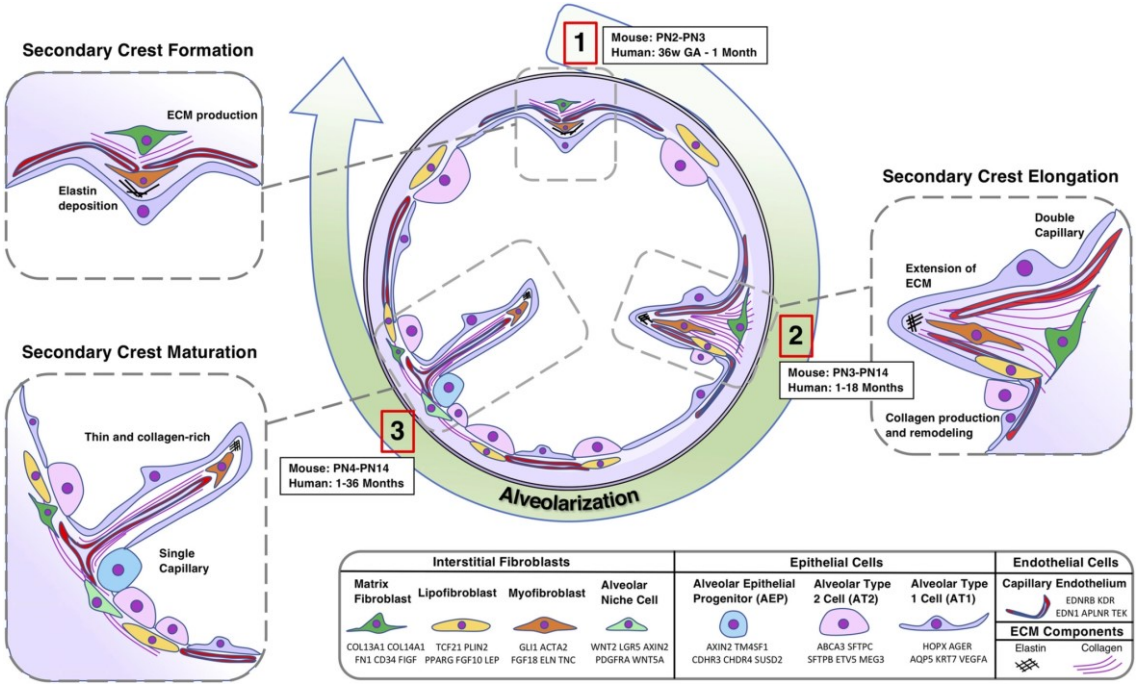

Figure 3. Interstitial lung fibroblasts and their role in alveolar septation and epithelial niche formation. Illustrations of mesenchymal subtypes and spatial and temporal contributions to alveolarization. Three key stages of alveolarization are arranged in a clockwise fashion in the center of the illustration. (1) Secondary crest formation occurs in mice between P2 and P3 and in humans between 36 weeks' gestational age and 1 month. (2) Secondary crest elongation occurs in mice between P3 and P14 and in humans between 1 and 18 months. (3) Secondary crest maturation occurs in mice between P4 and P14 and in humans between 1 and 36 months. Major events, such as elastin deposition during primary septum formation, are labeled in the respective panels. The spatial location of each cell type is reflected, such as myofibroblasts that resides at the septal tips and lipofibroblasts sitting adjacent to the alveolar epithelial type 2 cells (AEC II) (Ushakumary et al., 2021).

1.6.1 The epithelial cell lineage of alveolar niche

Alveolar epithelium covers more than 99 % of the internal surface area of the lung. It is composed of alveolar epithelial cells type 1 (AECs I) and type 2 (AECs II), each

constitutes 40 % and 60 % of the alveolar epithelium. During early lung development, AECs I and AECs II differentiate from a bipotent progenitors. Therefore, $Sox9^+$ progenitors are multipotent cells, which in embryonic lung development give rise to $Sox2^+$ cells of the airways, and later in lung development are capable to give rise to bipotent progenitors of AECs I and AECs II (Alanis et al., 2014; Desai et al., 2014; Eenjes et al., 2022). AECs I are highly attenuated cells and cover ~ 95 % of the alveolar surface. The main structural role of AECs I with their highly specialized morphology is achieved by flattening and folding of columnar progenitors (Yang et al., 2016). It had been shown that Nkx2-1 is required for AEC I morphology, quiescence and finally their maintenance (Vila Ellis and Chen, 2021). In addition to its structural role, AECs I are the major source of a number of key signaling molecules of alveogenesis such as Vegfa, Pdgfα and Shh (Vila Ellis and Chen, 2021). AECs II are characterized by heir lamellar bodies and are multifunctional cells that synthesize and secret surfactant, transport sodium to the basolateral cell surface to minimize alveolar fluid and produce molecules involved in innate immune defense (Fehrenbach, 2001). Additionally, AECs II function as facultative stem cells, self-renewing and differentiating into AECs I during injury-repair in the adult lung (Desai et al., 2014). During lung development, AECs II can give rise to AEC I (Fehrenbach, 2001; Vila Ellis and Chen, 2021). AECs are in close proximity to endothelial cells of the alveolar capillary network.

1.6.2 The endothelial cell lineage of the alveolus

Vasculature of the lung can be seen as shaped like a mesh. Neonatal lungs are comprised of squamous endothelial cells (ECs), which line the interior surface of the macro- and micro- vasculature (Joyce and Alexander, 2018). In the alveolar region, the microvasculature consists of capillaries, which are in close contact to epithelium, a prerequisite for optimal gas exchange in the alveolar region (Mammoto and Mammoto, 2019). Before alveolarization, endothelial progenitors are mainly derived from the bone marrow and the peripheral circulation system (Testa et al., 2016). However, it has been shown that there is an endothelial progenitor cell population residing in the lung with high vasculogenic capacity (Schniedermann et al., 2010). Generally, endothelial cells with a $Pecam^+$, $Foxf1^+$, $cKit^+$, $CD34^+$ and $CD309^+$ profile have been regarded as EC progenitors, due to their high self-renewal, proliferative and angiogenic capacity (Ciechanowicz, 2019). There are two different types of alveolar endothelial cells

amongst others (i) general capillary cells (gCAP) and (ii) aerocytes, which are also known as alveolar capillary cells (aCAP). Single cell RNA sequencing studies show gCAPs express Apelin receptor gene and consist of different EC types with high colony-formation capacity. While, aCAPs express Apelin and Carbonic anhydrase 4 genes and react to vascular endothelial growth factor (Vegf) produced by AEC I (Wang et al., 2022). Developmentally, the endothelium has a stable population pattern between E12-P14. However, the $Car4^{+}$ aCAPs emerge at E18.5 in mice from gCAPs. In summary, the aCAPs, as the important EC in the parenchyma, provide the niche, in which ECs interact with other resident cells to drive septal formation and capillary maturation during alveolarization (Mammoto and Mammoto, 2019).

1.6.3 Mesenchymal cell types of the alveolar niche during alveolarization

As mentioned before, every step in lung development relies on coordinated interactions of the pulmonary epithelium and the surrounding mesenchyme. Therefore, lung interstitial mesenchymal cells are crucial for alveolarization. At the saccular phase, these spindle shaped cells have a big oval nucleus with little cytoplasm, few organelles and scatter lipid droplets. These poorly differentiated mesenchymal cells are not involved in active protein synthesis and secretion (Vaccaro and Brody, 1978). Upon progress of lung development to the alveolar phase, mesenchymal cells become crucial for determining shape and size of the lung (Morimoto et al., 2010). Major cell type within the mesenchyme is the interstitial fibroblasts, which orchestrate the alveolarization, especially differentiation of interstitial cells. Due to the high plasticity and absence of robust, unique markers, characterizing lung mesenchymal fibroblasts has been hindered. Therefore, different subtypes have been characterized based on their location and gene expression profiles (Vila Ellis and Chen, 2021). In general, four main functions are defined for mesenchymal fibroblasts during alveolarization (1) proliferation (2) migration (3) extra cellular matrix (ECM) synthesis (4) apoptosis (Doherty et al., 2023; McGowan, 2014). Interstitial lung fibroblasts are derived from progenitors, which have specific gene expression profile as $CD31^{-}$, $CD45^{-}$, $Sca1^{+}$ expressing Pdgfrα and CD34 (McQualter et al., 2009; McQualter et al., 2013). Pdgf/Pdgfrα signaling has been demonstrated to be crucial for secondary septa formation (Boström et al., 1996). It has been shown that $CD31^{-}$, $CD45^{-}$, $Sca1^{+}$, Pdgfrα-expressing cells could expand and localize at the tips of elongating septa during

secondary septation and the paucity of Pdgf-A expression leads to alveolarization failure (Lindahl et al., 1997; McGowan and McCoy, 2013). Pdgfrα expressing cells can be classified based on their function and expression level of Pdgfrα. Functionally, they can be (i) crest myofibroblasts, (ii) lipofibroblasts and (iii) matrix fibroblast (Riccetti et al., 2022). Based on Pdgfrα expression level, the Pdgfrα^{+} fibroblast can appear in two subpopulations during alveolarization. (i) Pdgfrα (Pdgfra) high (Pdgfrα^{high}) expressing non-lipid myofibroblasts at the septal entrance and (ii) Pdgfrα low (Pdgfrα^{low}) expressing lipofibroblasts at the base of septa (Kimani et al., 2009; McGowan et al., 2008). Different interstitial fibroblasts reside in lung before and during alveolarization (table 2). Cellular location and interaction of different cell types during formation of the secondary septum is crucial (Figure 4). In particular, myofibroblasts and lipofibroblasts are mediators of secondary septum formation.

Table 2. Commonly used markers to distinguish different populations of fibroblasts during alveolarization. Adapted from (Rippa et al., 2021).

Fibroblast subtypes	**Suggested markers**
Matrix fibroblast	Colol14a1, CD34, Pdgfrα
Myofibroblast	Tbx4, Acta2, Pdgfrα, Fgf18, Eln
Lipofibroblast	Thy1, Pparg, Fgf10, Tcf21, Plin2 (ADRP), Leptin, Pdgfrα
Alveolar niche cell	Axin2, Lgr5, Wnt2, Wnt5a, Pdgfrα

1.6.4 Myofibroblasts during alveolarization

Myofibroblasts were first described in 1971 during the wound healing process in rats. Morphologically, they were similar to conventional fibroblast with a prominent difference “the ability to contract” (Gabbiani et al., 1971). Moreover, physiologically they were producing collagen for repairing injured tissue (Pakshir et al., 2020). These myofibroblasts were expressing the intermediate filament vimentin, which is found in the cytoskeleton of mesenchymal cells (Gabbiani, 1992). The expression of α-smooth muscle actin (α-SMA) is characteristic for myofibroblasts and a shared feature with smooth muscle cells (Hinz et al., 2012; Skalli et al., 1986). Recent single cell sequencing analysis showed that other markers such as Heavy metal binding protein HIPP-like, Abnormal spindle microtubule assembly and musculoskeletal embryonic

nuclear protein 1 are new putative markers for myofibroblasts in the lung (Xie, 2018). Myofibroblasts in normal lung derived from Pdgfrα⁺ cells and they are found to underline at the tip of the secondary crest, suggesting they may be important in septae formation. These are known as alveolar crest myofibroblasts. (Branchfield et al., 2016a; Li et al., 2018a). It has been shown that sonic hedgehog signaling is required for myofibroblasts differentiation and its interruption during alveolarization eliminates majorly glioma-associated oncogene homolog 1 (Gli1⁺) α-SMA⁺ cells at the septal tips during alveolarization (Kugler et al., 2017). Moreover, these mesenchymal cells deposit ECM proteins such as collagen and elastin, which are essential for secondary septa formation (Noguchi et al., 1989; Yamada et al., 2005). ECM proteins provide elasticity to the parenchyma during normal respiration to preserved alveolar structure (Hinz et al., 2007). Although myofibroblasts are abundant in early stages of lung development branching morphogenesis (P3-P13) and alveolarization they diminish in the adult lung in homeostasis (Endale et al., 2017). However, during disease condition, the activated myofibroblasts can be found during the pathogenesis of fibrosis (Hinz et al., 2007).

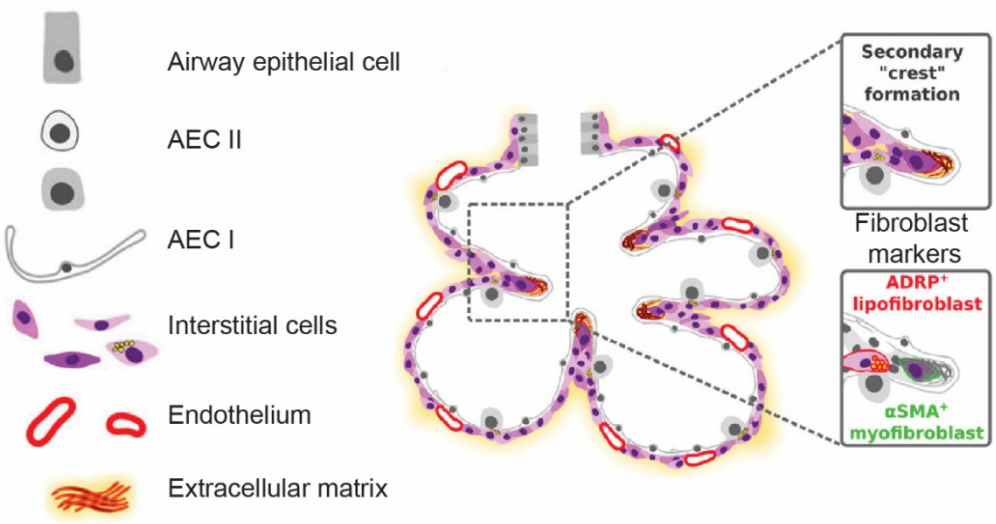

Figure 4. Mesenchymal cell types in distal lung during alveolarization. Alveolar mesenchymal fibroblasts such as myofibroblasts and lipofibroblasts differentiate from mesenchymal progenitor cells. Provided by (Rodríguez-Castillo, 2018).

1.6.5 Lipofibroblasts

Among all known mesenchymal subpopulations, lipofibroblasts are the least well described mesenchymal cells in the lung. Pulmonary interstitial lipid-laden fibroblasts are adipocyte-like mesenchymal cells, which were first described by O'Hare in 1970s and later during the early and late murine lung development and in human (Burri, 1985; O'Hare and Sheridan, 1970; Rehan, 2006; Travaglini et al., 2020). Later, these interstitial cells were characterized by the abundance of lipid droplets and high glycogen content and with localization in the center of alveolar septa (Brody, 1985).These interstitial cells were introduced as differentiated mesenchymal cells and named "Lipofibroblasts" (LIFs) (Torday, 1997; Trapnell et al.).

The advent of LIFs is considered as an alveolar evolutionary defense mechanism towards hyperoxic atmosphere at birth (Rehan, 2014). LIFs appear at E16 (canalicular stage) in murine lung and peak in number during the second postnatal week (Al Alam, 2015). As mentioned already, LIFs contain lipid droplets with a composition of 65 % neutral lipid triglycerides, 14 % cholesterol esters, 14 % phospholipids and 7 % free fatty acids (Awonusonu et al., 1999). LIFs contain lipoprotein lipase and are able to accumulate neutral lipid droplets and show positivity to lipophilic oil red-O stain (Maksvytis et al., 1984; McGowan et al., 1995). In addition to triglycerides, LIFs store also retinoic acid which is crucial for secondary septation (Simon and Mariani, 2007). LIFs express fibroblast marker Thy1 (Torday, 1997). There are also commonly reported LIFs markers such as Tcf21, Fgf10, G0s2 in the embryonic and late lung development (Al Alam, 2015; McGowan and McCoy, 2014; Park et al., 2019; Rehan et al., 2006; Schultz et al., 2002; Varisco, 2012). However, all of them except Tcf21, were not discriminative in other developmental and disease stages (Liu et al., 2021). To-date, different important functions were proposed for LIFs, such as in lung homeostasis and development (Lv et al., 2021; Ntokou et al., 2015b), synthesis of surfactant (Schultz, 2002), storage of vitamin A (Dirami et al., 2004; Senoo et al., 2007) and finally regeneration (Green et al., 2016). What makes lipofibroblasts so interesting is that they present mainly in close proximity to AECs II and support them in proliferation and their differentiation before and during alveolarization (Yuan, 2018). Since, they transfer neutral lipid to AEC II for surfactant phospholipid synthesis to reduce the surface tension of alveoli (Ushakumary et al., 2021). This process is highlighted under so-called "Epithelial-Mesenchymal paracrine signaling" path. Under control of Shh gene

expression, AEC II express Parathyroid hormone-related protein (Pthrp). Its related receptor is expressed on the lipofibroblasts (Kugler et al., 2017; Rehan and Torday, 2007). This leads to protein kinase-A activation which in turn downregulates Wnt signaling pathway, which cause the upregulation of Pparg, an adipogenic nuclear transcription factor, and its downstream targets Plin2 and leptin and impacts on neutral lipids trafficking triglycerides to AECs II. Eventually, Leptin binds to its receptor on AECs II site and stimulates surfactant phospholipid synthesis (Chao et al., 2016; Chao, 2015). Moreover, LIFs serve as mesenchymal alveolar niche to AEC II in adult lung and diseases (Chung et al., 2018; Zepp et al., 2017).

In summary, LIFs are believed to be crucial not only during late lung development but also in adult lung and disease conditions.

1.6.6 Perilipin2 (Plin2)

Lipid droplets (LDs) are the lipid storage unique organelles consisting of a neutral lipid core, mainly made up from cholesterol esters and triglyceride (TG) covered by a phospholipid monolayer and various proteins, in particular “Perilipins”. (Farese and Walther, 2009; Martin and Parton, 2006). Five paralogous mammalian perilipin genes have been identified, Plin1-Plin5. (Bickel et al., 2009). Mammalian cells express several Plin proteins where the dominating Plin proteins at the LD surface differ among the cell types (Tatsumi et al., 2018; Thiam et al., 2013). Each mammalian tissue expresses at least two Plin types, where combinations of expressed Plin members likely fulfill cell-specific requirements for LD regulation (Kimmel and Sztalryd, 2016).

Plin2, a LDs coating protein, was discovered as an mRNA induced in differentiating adipocytes (Jiang and Serrero, 1992). It was revealed later that Plin2 has ubiquitous expression with different expression levels and its expression is highly related to the amount of neutral lipids in the cells (Heid et al., 1998). Plin2 is regulated at the transcriptional level by peroxisome proliferator-activated receptor α (Ppara) (Edvardsson et al., 2006) but also through post-transcriptional degradation by the proteasomal system when lipid levels are low in the cell (Masuda et al., 2006). Plin2 functions as triglycerides protector by encapsulating them on one side, facilitates the LDs lysosomal degradation on the other side (Kaushik and Cuervo, 2016; Tsai et al., 2017). Indeed, Plin2 seems to play an important role in the LDs assembly and trafficking in Plin2-expressing cells.

1.7 Single cell RNA sequencing (scRNAseq)

Transcriptomics is one of the highthroughput technologies used to study an organism's transcript pool "transcriptome". In 1990s was first tried to study the entire transcriptome. Using high throughout RNA sequencing, transcriptomics is able to measure gene expression of an individual in different tissue, condition and timepoints. This provides scientists invaluable insights into gene expression, regulation and function and even alteration in pathological conditions. Since 1990s, technological advances have made transcriptomics as a widespread discipline by biologist (Lowe et al., 2017). To provide a higher resolution of cellular differences and a better understanding of the function of an individual cell in the context of its microenvironment, RNA sequencing was further developed to detect expression profile at the single cell resolution. It was first in 2009, scRNAseq was performed on mouse blastomere with only four cells (Tang et al., 2009). That time, the lack of multiplexing in library preparation was a technical obstcle in scRNAseq studies. Since then different groups tried to improve library preparation techniques to increase scalability of this technology (Islam et al., 2011; Klein et al., 2015; Macosko et al., 2015). Finally in 2015, with combination of microfluidics and nucleotide barcoding, a technique was developed in which a single cell could be encapsulated in an oil droplet microreactor in a high-throughput manner (Klein et al., 2015; Macosko et al., 2015). This technique has been optimized by an american company 10X Genomics which dropped the cost of a library preparation for a single cell to cents (Chambers et al., 2019). scRNAseq is a powerfull and reproducible thechnology to investigate questions that could not be addressed by other methodologies. Main advantages are assessment of cell-to-cell variations, identification of rare populations specially in developmental studies and also determination of heterogeneity within a cell population (Wu et al., 2018). A typical scRNAse workflow incorporates main steps (1) Single cell dissociation (2) Single cell isolation (3) Library preparation (4) Sequencing. The first step is tissue digestion to provide single cell suspension. Afterward, cells will be isolated based on the experimental set-up. In the 10X Genomics platform, which is used in this work, each droplet contains a cell and necessary chemicals to break down the cell membrane and to perform library construction. Library construction is a process in which captured intracellular mRNA first is reverse-transcribed to cDNA and then amplified. Meanwhile, mRNA from each cell is labeled with a droblet-specific barcode and unique molecular

identifiers (UMI). UMIs allow us to distinguish between amplified copies of the same mRNA and reads from separate mRNA molecules transcribed from the same gene. After library preparation, these libraries are pooled (multiplexed) for sequencing. Sequencing produces read data. Raw data are processed and aligned to obtain count (read) matrices. Raw data are further pre-processed by quality control, normalization, data correction, feature selection and dimensionality reduction. In the last step, data are visualized and undergone downstream analysis such as clustering, differential gene expresseion, computational analysis (Luecken and Theis, 2019).In the present study, we utilized scRNA-seq to examine the molecular signatures of LIFs. This method allows for transcriptional profiling of thousands of individual cells, providing a high-throughput analysis of gene expression at the single-cell level. Using scRNA-seq in the present study, it was investigated which genes were expressed, in what quantities, and how they differed across thousands of cells derived from Perilipin2 cell lineage ($Plin2^{lin}$). This approach allowed us to elucidate the heterogeneity of cell clones and to identify potential candidate markers specifically targeting LIFs during alveolarization.

2 Hypothesis

Pulmonary lipofibroblasts express the lipoprotein Perilipin 2 (Plin2) and can be specifically targeted in mice using Plin2$^{tm1.1\ (Cre/ERT2)\ Mort}$ (Plin2^{creERT2}) mice. Using this tool, function, molecular signatures and cellular characteristics of lipofibroblasts during alveolarization can be analyzed.

3 Aims of the study

Aims of the present study were:

(1) To elucidate the function of pulmonary lipofibroblasts during lung alveolarization in mice using a cell type specific cre-recombinase stop loxP diphtheria toxin A approach.

(2) To characterize molecular signatures of cells of the Perilipin 2 cell lineage (Plin2^{lin}) during alveolarization and the contribution of Plin2^{lin} cells to pulmonary cell populations during alveolarization in mice using a cell type specific lineage tracing approach combined with a single cell RNA sequencing approach.

4 Materials and Methods

4.1 Technical equipment

Technical equipment, devices, consumables, reagents and software utilized in all experimental procedures are reported in table 3, 4, 5 and 6.

Table 3. Name of equipment, devices, and manufacturer

Product	**Manufacturer**
Analytical balance	VWR International
BD FACSAria™ II Cell sorter	BD Biosciences
Biosafety cabinet, class II	NuAire
Cell culture incubator	Thermo Fisher Scientific
Centrifuge 5430 R	Eppendorf
Centrifuge, Multifuge 3 S-R	Heraeus
Chemical fume hood	Norddeutsche Laborbau
Confocal microscope, LSM 710	Carl Zeiss
Cooling ThermoMixer, HLC – MKR 13	Digital Biomedical Imaging Systems AG
Fluorescent microscope, DM6000 B	Leica
gentleMACS™ dissociator	Miltenyi Biotec
Heating plate	Medax
Hybridization oven, PersonalHyb	Stratagene California
Incubator, Heracell vios 160i	Thermo Fisher Scientific
Laminar flow hood	NuAire, Inc.
LSR Fortessa	BD Biosciences
Magnetic stirrer	Heidolph Instruments
Microcentrifuge	Labnet International
Microcentrifuge, Heraeus™ Fresco™ 17	Thermo Fisher Scientific
Microtome,RM2255	Leica
NanoZoomer 2.0-HT Slide scanner	Hamamatsu Photonics K.K.
Paraffin embedding station, EG 1160	Leica

Product	Manufacturer
PCR System, ProFlex	Thermo Fisher Scientific
pH benchtop meter, SevenCompact Duo S213-meter	Mettler Toledo
Pipettes, automatic: 10µl, 100µl and 300 µl	Eppendorf
Pipettes, manual:: 10µl, 100µl 300 µl and 1 ml	Eppendorf
Pipettor, Easypet 3	Eppendorf
Real-Time PCR System, QuantStudio 3	Thermo Fisher Scientific
Reusable Knife, 16 cm, profile d steel assy	Leica
Spectrophotometer, NanoDrop® ND-1000	Thermo Fisher Scientific
Stereomicroscope, M50	Leica Byosistems
Surgical instruments (various)	F.S.T
Ultra Microtome, MX35	Thermo Fisher Scientific
Ultraviolet (UV) transiluminator/Gel imager	Intas
Vacuum Tissue Processor, ASP200 S	Leica
Vibratome, Leica VT1200S	Leica
Vortex mixer	IKA®-Werke

4.2 Consumables

Table 4. Name of consumables and the manufacturer

Product	Manufacturer
Cover slides	Carl Roth
Easy strainer 100 µM	Greiner bio-one
Easy strainer 40 µM	Greiner bio-one
FACS tubes	VWR
Embedding cassettes, Rotilabo®	Carl Roth
Filter pipette tips: 10 µl, 100 µl, 200µl, 300µl, 1 ml	Greiner bio-one
GentleMACS C tubes	Miltenyi Biotec
iSpacerR one well, 0.2 and 0.5 mm	SunJin Lab

Product	Manufacturer
Micro centrifuge tubes: 0.5, 1.5 and 2 mL	Eppendorf
Pasteur pipette, 3.5 ml	Sarstedt
Pipettes, serological: 2 ml, 5 ml, 10 ml, 25 ml, 50 ml	Falcon
Seraflex	Serag wiessner
Super Frost™ Ultra Plus Adhesion slides	Thermo fisher Scientific
Syringes, Micro-Fine™+ 0.3ml 0.30mm (30G) x 8mm	BD Biosciences
Test tubes: 15 ml and 50 ml	Greiner bio-one
Titanium Ligating Clips, Horizon™	Teleflex Incorporated

4.3 Reagents and drugs

Table 5. Name of reagents, drugs and the manufacturer.

Product	Manufacturer
4-Hydroxytamoxifen	Merck
4',6-Diamidino-2-Phenylindole (DAPI)	Thermo fisher Scientific
Absolute Counting Beads, Count Bright™	Thermo fisher Scientific
Agar	Merck
Agar for embedding	Carl Roth
Agarose	Carl Roth
Bovine Serum Albumin	Merck
Citric acid monohydrate	Carl Roth
Compensating beads, OneComp eBeads	eBioscience Inc.
Cytofix™ Fixation Buffer BD Biosciences	Cytofix™ Fixation Buffer BD Biosciences
Deoxyribonuclease I	Serva
Dispase	Corning
DMEM, high glucose (4.5g/l), HEPES	Thermo fisher Scientific
Dulbecco's phosphate buffered saline 10×	Merck
eBioscience™ Flow Cytometry Staining Buffer	Thermo fisher Scientific

Product	Manufacturer
Ethanol ≥99,8 %	Carl Roth
Ethidium bromide solution 1 % (10 mg/ml)	Carl Roth
Fixation and Permeabilization Solution	BD Biosciences
Fixation Buffer	BD Biosciences
Flow Cytometry Staining Buffer	Thermofisher Scientific
Fluoromount W	Serva
Goat serum	Merck
HBSS 1x	Thermofisher Scientific
HCS LipidTOX™ Deep Red Neutral Lipid Stain	Thermo Fisher Scientific
HCS LipidTOX™ Green Neutral Lipid Stain	Thermo Fisher Scientific
HEPES solution1 M, pH 7.0-7.6	Merck
Hydrochloric acid (HCl)	Carl Roth
Hydrogen peroxide solution, 30 %	Merck
Isopropanol	Merck
Magnesium chloride (25 nM)	Thermo Fisher Scientific
Magnesium chloride (50 nM)	Thermo Fisher Scientific
Mayer’s hematoxylin solution	Merck
Metamizol, Novalgin® (drops. 500 mg/ml)	Sanofi
Methanol	Carl Roth
Methyl green	Vector Laboratories
Methylene blue	Carl Roth
Mowiol	Made in-house
Nuclease-free water	Ambion
Ultra low melting agarose	Merck
Paraffin, Paraplast®	Leica
Paraformaldehyde	Merck
Penicillin - Streptomycin for cell culture (100X)	AppliChem

Product	Manufacturer
Perm/Wash	BD Biosciences
Pertex™ mounting medium	Medite
Phosphate buffered saline (1x and 10x)	Merck
Resorcinol-Fuchsine-solution acc. to Weigert	Roth
Roti®-Histol	Carl Roth
Sodium hydroxide (NaOH)	Carl Roth
Tamoxifen	Merck
Tissue-Tek O.C.T.TM Compound	Sakura Finetek
Tris-Acetate-EDTA) buffer	Thermo Fisher Scientific
Tris-EDTA (TE) buffer	Thermo Fisher Scientific
Triton® X 100	Carl Roth
TWEEN® 20	Merck
Water for injection	Thermo Fisher Scientific
Van Gieson	Carl Roth

4.4 Software

Table 6. Name of the software and the manufacturer

Product	Manufacturer
DIVA software	BD Biosciences, USA
FlowJo_V10	BD, USA
GraphPad Prism 7.0	GraphPad Software, USA
ImageJ	NIH, USA
ImageQuant LAS 4000	GE Healthcare, United Kingdom
Microsoft Office	Microsoft, USA
StepOne™ and StepOnePlus™ Software v2.3	Thermo Fisher Scientific, USA

4.5 Primary and secondary antibodies

Antibodies used in this work are listed in the table 7.

Table 7. Name of primary/secondary antibodies, catalog number, host, conjugate and company name.

Primary antibodies				
Target protein	**Catalog number**	**Host**	**Conjugates**	**Company**
Perilipin 2	ab52356	Rabbit	none	abcam
Alpha-SMA	SAB5500002	Rabbit	none	Sigma
CD16/32	553141	Rabbit	none	BD Bioscience
CD 326	118216	Rat	PE/Cy7	Biolegend
CD 31	102506	Rat	FITC	Biolegend
CD 31	ab28364	Rabbit	none	abcam
CD 45	103112	Rat	APC	Biolegend
ProSP-C	AB3786	Rabbit	none	Millipore
Podoplanin	AF3244	Goat	none	R & D system
Isotype	400505	Rat	FITC	Biolegend
Isotype	400617	Rat	PE/Cy7	Biolegend
Isotype	400512	Rat	APC	Biolegend
Secondary antibodies				
Goat IgG	A21446	Rabbit	Alexa 647	Invitrogen
Rabbit IgG	A21244	Goat	Alexa 647	Invitrogen
Rat IgG	A21247	Goat	Alexa647	Invitrogen

4.6 Approvals for animal experimental studies

All mouse lines were employed in this study were approved by the local authorities (Regierungspräsidium Darmstadt) under approval number: B2/1151; B2/1129. Mice

were kept under standard conditions of purified air and water, supplied with food *ad libitum* and exposed equal cycles of 12 h light-darkness prior to experiments.

4.7 Mouse lines

4.7.1 C57BL/6J wild type mice

Mus musculus C57BL/6J wild type mice were purchased from the Jackson Laboratory.

4.7.2 Plin2$^{tm1.1\ (Cre/ERT2)\ Mort}$

Plin2$^{tm1.1(Cre/ERT2)Mort}$ (Plin2^{creERT2}) is an inducible CreERT2 driver mouse line that has been generated in Max Planck Institute, Bad Nauheim (Ntokou et al., 2017). A cassette containing CreERT2 and a monomeric Cherry fluorescent (mCherry) was inserted into the exon 8 of the Plin2 gene. These components were inserted at the end of the endogenous gene and joined by "reading bridges" (T2A segments). Thereby the original gene is remained fully functional even in homozygous mice. The mCherry fluorescent enables studying of the actual Plin2 expression as a direct reporter. Cre could be employed to lineage trace and ablate Plin2-expressing cells in combination with global mTmG reporter and DTA mouse lines respectively (Muzumdar et al., 2007; Voehringer et al., 2008). The Cre and mCherry are under control of the Plin2 promoter and expressed as long as the Plin2 is expressed.

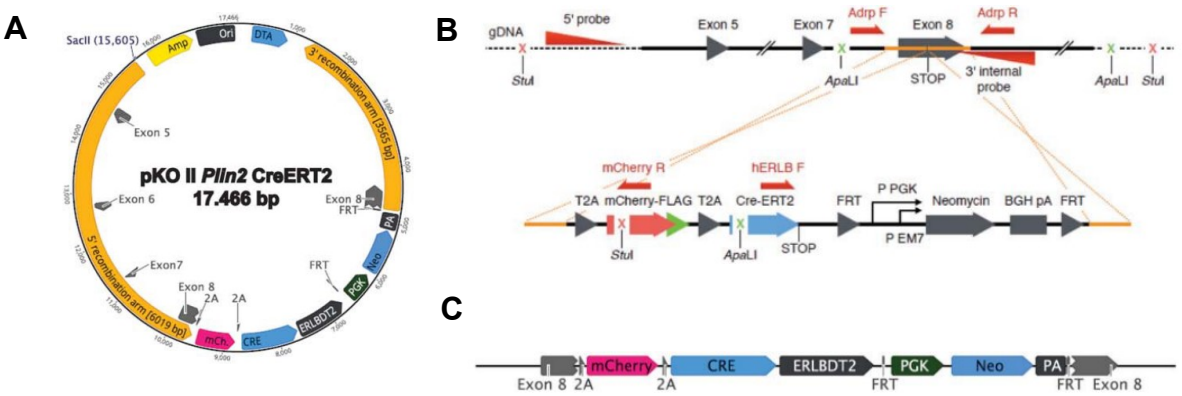

Figure 5. Construct of Plin2$^{tm1.1\ (Cre/ERT2)\ Mort}$ mouse. (A) Vector to target Perilipin 2 (Plin2). (B) Schematic diagram of integration of the mCherry/CreERT2 expression cassette into exon 8 upstream of the stop codon. (C) Scheme of mCherry/CreERT2 expression cassette. Provided by (Ntokou et al., 2017).

4.7.3 Gt (R26)26Sor$^{tm4\ (ACTB\text{-}tdTomato,\ EGFP)\ Luo/J}$

Gt (R26)26Sor$^{tm4\ (ACTB\text{-}tdTomato,\ EGFP)\ Luo/J}$ (R26^{mTmG}) mouse line was purchased from the Jackson Laboratory (Stock ID: 007576). It expresses tandem dimer Tomato (tdTomato) in all tissues and cell types with membrane localization. However, after breeding this mouse with a cre-driver mouse, after cre-mediated intra-chromosomal recombination the stop codon is removed, tdTomato expression will be silenced and membrane-targeted green fluorescent protein (mGFP) will be expressed. This double-fluorescence system allows visualization of recombined as well as non-recombined cells. Moreover, by locating the fluorescent protein in the cell membrane, one can investigate the cell morphology as well (Figure 6).

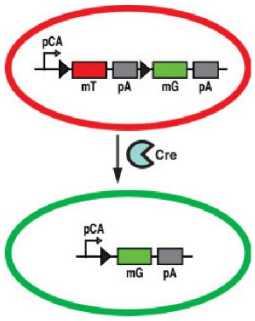

Figure 6. Schematic diagram of the mTmG construct before and after Cre activation. The mTmG construct has a CMV enhancer/chicken beta-actin core promoter (pCA) driving expression followed by a loxP site, an N-terminal membrane-tagged tdTomato (mT) cassette, a polyadenylation (pA) signal, a loxP site, an N-terminal membrane-tagged enhanced green fluorescent protein (mG) cassette and a pA signal. Cells and tissue(s) express a strong red fluorescence. Adopted from (Muzumdar et al., 2007).

4.7.4 B6.129P2-Gt (R26)26Sor$^{tm1\ (DTA)\ Lky/J}$ line

B6.129P2-Gt (R26)26Sor$^{tm1\ (DTA)\ Lky/J}$ (R26^{DTA}) mouse line was purchased from the Jackson Laboratory (STOCK ID: 009669). It has a floxed-STOP cassette before the open reading frame of the integrated diphtheria toxin A (DTA) gene. When this mouse is bred with a cre driver mouse line cre recombines upon tamoxifen injection. Cre recombination cuts off the stop codon, which subsequently results in DTA expression in all cells where cre is active (Voehringer et al., 2008).

4.7.5 Plin2$^{tm1.1\ (Cre/ERT2)\ Mort}$; B6.129P2-Gt (R26)26Sor$^{tm1\ (DTA)\ Lky/J}$ line

Conditional Plin2^{creERT2} line was utilized in combination with R26^{DTA} depleter mice. Double transgenic mice were induced with a single intraperitoneal (i.p.) Tmx injection. The Tmx-induced activation of cre lead to permanent DNA recombination and

subsequently deletion of a floxed-STOP cassette and finally expression of diphtheria toxin subunit A (DTA) in specific cre-expressing cells (Figure. 7). Diphtheria toxin production in Plin2^{+} cells causes cells to undergo apoptosis and cell death.

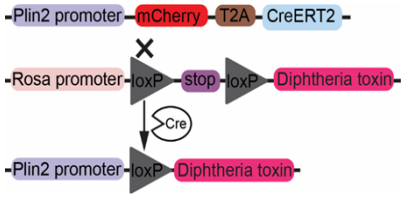

Figure 7. Scheme of induction of cre-recombination in a depleter mouse. Plin2^{creERT2} mice were crossed with R26^{DTA} to generate inducible Plin2 depleter mice (Plin2^{creERT2}; R26^{DTA}). Upon Tmx injection, cre recombines and excises the stop-loxP codon, which leads to Diphtheria toxin A expression.

4.7.6 Plin2$^{tm1.1\ (Cre/ERT2)\ Mort}$; Gt (R26)26Sor$^{tm4\ (ACTB-tdTomato,\ -EGFP)\ Luo/J}$ line

Crossing Plin2creERT2 driver line with cre-dependent recombinase responsive mouse lines like a global R26^{mTmG} reporter line can provide a tool for lineage tracing and of Plin2^{+} cells upon cre activation with Tmx. Depending on the time point of cre activation (Tmx injection), cells can be targeted in a time-controlled manner. Using lineage tracing, characteristics of Plin2^{+} offspring cells (cells of Plin2^{lin}) can be studied in a time-controlled manner. Upon cre recombination, Plin2^{+} cells and all progeny will express the reporter gene GFP and be tracked by imaging techniques.

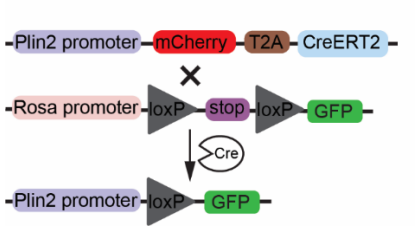

Figure 8. Scheme of induction of cre-recombination in a reporter mouse. Plin2^{creERT2} mice were crossed with R26^{mTmG} to generate inducible Plin2 reporter mice (Plin2^{creERT2}; R26^{mTmG}). Upon, Tmx injection, cre recombines and excises the stop-loxP codon, which leads to GFP expression.

4.8 Genotyping of transgenic mice

Prior to the genotyping process, genomic DNA was isolated from the tail of transgenic mice using the AccuStart™ II Mouse Genotyping Kit following manufacturer's recommendations.

Table 8. Primers used to amplify genomic DNA for genotyping.

Mouse line	Primer name	Primer sequence	Size of amplicon (bp)
Plin2^{CreERT2}	Cre F	5′-TGCCCCTCTATGACCTGCTGCT-3′	Mut Cre: 315
	Cre R	5′-TGCTCTGGTGACAAGGAGGGGT-3′	Mut mCherry: 584
	mCherry F	5′-AGCGCCTTCGGATCCACCTCT-3′	Wt: 441
	mCherry R	5′-CTCGTGGCCGTTCACGGAGC-3′	
R26^{mTmG}	R26 F	5′-CTCTGCTGCCTC CTG GCT TCT-3′	Mut mTmG: 250
	R26 R	5′-CGAGGCGGATCACAAGCA ATA-3′	Wt: 330
	CAGP R	5′-TCAATGGGCGGGGGTCGTT-3′	
R26^{DTA}	Wt F	5′-CCAAAGTCGCTCTGAGTTGTTATC-3	Mut DTA: 650
	Wt R	5′-GAGCGGGAGAAATGGATATG-3′	Wt DTA: 603
	DTA F	5′-CGACCTGCAGGTCCTCG -3′	
	DTA R	5′-CTCGAGTTTGTCCAATTATGTCAC-3′	

F: Forward; R: Reverse;

4.9 Genotyping PCR and DNA electrophoresis

To screen the genotype of loci of interest in transgenic mice, end-point PCR and DNA electrophoresis were employed. After preparing the master mix, related primers were added and PCR amplification protocol was followed. Amplicons were resolved in a 1.5 % agarose gel prepared in 1× TAE buffer and the bands were visualized by ethidium bromide (EtBr) (0.2 µg/ml) using a trans-illuminator (INTAS UV-system, Intas Science Imaging Instruments, Germany). Primer sequences, reaction components, amplification protocol are provided in tables 8, 9 and 10.

Table 9. Components used to amplify genomic DNA for genotyping.

Mouse line	Target locus	Components	Per sample (µl)
Plin2^{CreERT2}	Cre/mCherry	Nuclease-free H_2O	9.25
		REDTaqReadyMix (Sigma - R2523)	9.25
		Primer F+R	0.25+0.25
		Genomic DNA	2
R26^{mTmG}	R26	Nuclease-free H_2O	4.5
		Immomix (Bioline -Bio-25022)	5
		Primer F+R	0.25+0.25
		Genomic DNA	1
R26^{DTA}	DTA	Nuclease-free H_2O	5.38
		Kapa buffer B 10X	1.2
		Kapa Taq 5U/microl	0.06
		dNTPs	0.96
		Primers F+R	1.2+1.2
		Genomic DNA	2

Table 10. PCR cycling protocols for genotyping transgenic mice

Mouse line	Step	Reaction		Temperature	Time
Plin2^{CreERT2}	1	Denaturation		95 °C	3 min
	2	Denaturation	40×	95 °C	20 s
	3	Annealing		56 °C	30 s
	4	Extension		72 °C	35
	5	Final Extension		72 °C	7 min
	6	Storage		4 °C	∞
R26^{mTmG}	1	Denaturation		95 °C	15 min
	2	Denaturation	35×	94 °C	30 s
	3	Annealing		61 °C	61 s
	4	Extension		72 °C	60 s
	5	Final Extension		72 °C	2 min
	6	Storage		4 °C	∞
R26^{DTA}		Denaturation		94 °C	3 min
		Denaturation	35×	94 °C	30 s
		Annealing		60 °C	60 s
		Extension		72 °C	60 s
		Final Extension		72 °C	2 min
		Storage		4 °C	∞

4.10 Tamoxifen administration

A tamoxifen (Tmx) stock of 20 mg/ml was prepared by dissolving Tmx powder in a mixture of medium-chain triglycerides (Miglyol 812, Caesar & Loretz Hilden, Germany) prior to injection. Pups and adult mice were injected intraperitoneal with 0.2 mg and 100 mg tamoxifen per gram body weight respectively.

4.11 Paraffin tissue processing

Mice were sacrificed and after intratracheal intubation, lungs were perfused with PBS 1× and then inflated with 4 % paraformaldehyde (PFA) at 20 cm H_2O hydrostatic pressure. Removed lungs, liver, kidneys and spleen were kept in PFA 4 % at 4°C over

night. Tissues were then dehydrated with Leica ASP200S tissue processor, and embedded in paraffin blocks with Leica EG1160 and Leica EG1150C. The tissues were then sectioned using Leica RM2255 microtome into 3 µm thick sections and allowed to dry at room temperature (RT). Deparaffinization of the slides occurred by heating at 59 °C for 60 min.

4.12 Elastica staining

Histological sections. Elastica staining stains elastic fibers in dark blue and other cell components as a pinkish red. Elastic fibers are localized at the tip of alveolar secondary septa, therefore potential changes in morphology of septa e.g. septal simplification could be distinguished. Elastica staining was performed according to previous publication (Pieretti et al., 2014). Slides were washed twice 5 min in Xylol, followed by a 2 min step of series of progressively reduced ethanol concentration [96 % (*v*/*v*), 80 % (*v*/*v*), and 70 % (*v*/*v*)], and subsequently submerged for 15 min in Resorcinol-Fuchsine-solution. Lung tissues were next washed for 1 min in tap water before counter-stained with Weigert hematoxylin for 5 min. Tissues were subsequently washed for 15 min in tap water, followed by 5 sec in 1 % hydrochloric acid 70 % alcohol (*v*/*v*), and 5 sec in ddH_2O. Next, Van Gieson solution was used in order to stain for collagen and the cellular cytoplasm. Once staining was carried out, tissue was once again progressively dehydrated [twice submerged for 2 min in 96 % (*v*/*v*) ethanol, once for 2 min in 2-propanol 99.8 % (*v*/*v*) ethanol and twice for 5 min in Xylol] and mounted with Pertex. Images were generated by using the nanozoomer at bright field.

4.13 Hematoxylin and Eosin staining

Slides were washed twice in Xylol for 5 min, followed by 4 min steps of reduced ethanol concentration [96 % (*v*/*v*), 80 % (*v*/*v*), 70 % (*v*/*v*), and 60 % (*v*/*v*) ethanol] followed by a 2 min ddH_2O washing step. Lung tissues were next stained with Mayer Hematoxylin solution during 5 min followed by a 5 min tap water washing step. Following, 5 min submersion step in aqueous Eosin 1 % (*v*/*v*) and 5 min washing step in tap water were performed. Finally, tissues were dehydrated [twice submerged for 2 min in 96 % (*v*/*v*) ethanol, once submerged for 2 min in 2-propanol 99.8 % (*v*/*v*) ethanol and twice submerged for 5 min in Xylol] and mounted with Pertex. Images were generated by using the Nanozoomer at bright field.

4.14 Total RNA isolation and real-time PCR

Total RNA was isolated from P7 and P4 mouse lungs using miRNeasy mini kit following manufacturer's protocol. Tissues were placed into 2 ml tube containing ceramic beads and homogenized using Precelly 24-Dual. Total RNA was then suspended in 30 µl nuclease-free water and concentration was determined using NanoDrop One Microvolume UV-Vis Spectrophotometer. Subsequently, cDNA was prepared using 1000 ng/µl RNA. Steps, reactions, temperature and the reaction time for amplifying cDNA are reported in table 11. A master mix was prepared by using the reagents listed in table 12 to obtain a final volume of 40 µl. Real time polymerase chain reaction (RT-qPCR) was carried out using Platinum SYBR Green qPCR SuperMix-UDG to analyze changes in gene expression for mRNA. The qPCR was assessed in the StepOne Real-Time PCR System and cycling conditions are reported in Table 12. For qPCR analysis, ΔCt values were assessed as mean Ct (reference gene) – Ct (gene of interest), where the Polr2a gene was used as reference genes for mRNA. Primer pairs were validated prior experimental design (Table 14).

Table 11. Reverse transcription procedure to prepare cDNA from mRNA

Step	Reaction	Temperature	Time
1	Incubation	21 °C	10 min
2	Extension	43 °C	75 min
3	Enzyme Inactivation	95 °C	5 min
4	Storage	4 °C	∞

Table 12. PCR reaction mix used to prepare cDNA for gene expression analysis

Component	1 sample (µl)
Nuclease-free H_2O	1
GeneAmp™ 10× PCR Buffer	4
Magnesium chloride solution (25 mM)	8
dNTP Mix (10 mM)	2
Random Hexamers (50 µM)	2
RNase Inhibitor (20 U/µl)	1
M-MLV Reverse Transcriptase (50 U)	2
RNA (1000 ng/µl)	20
	Total 40

Table 13. RT-qPCR cycling conditions

Step	Reaction		Temperature	Time
1	Denaturation		95 °C	5 min
2	Denaturation	40×	95 °C	5 s
3	Annealing		59 °C	5 s
4	Extension		72 °C	30 s
5	Final Extension		72 °C	5 min
6	Melting Curve Analysis			30 min
7	Storage		4 °C	∞

Table 14. List of primers used for RT-qPCR analysis

Primers		
Gene	**Forward (5′ - 3′)**	**Reverse (5′ - 3′)**
Acta2	GCATCCACGAAACCACCTAT	TCCACATCTGCTGGAAGGTA
Arg1	GGTTCTGGGAGGCCTATCTT	CACCTCCTCTGCTGTCTTCC
Casp3	GTCCATGCTCACGAAAGAAC	ACCTGATGTCGAAGTTGAGG
Casp8	GCTTGGACTACATCCCACAC	TCTCTCACCATCTCCTCTCG
CD31	ACTTCTGAACTCCAACAGCGA	CCATGTTCTGGGGGTCTTTAT
Col13a1	AATGGAAGTTCTACTCGCGTAGG	TTCTCGCCTGGTTGACCTTTG
Col1a1	AGACATGTTCAGCTTTGTGGAC	GCAGCTGACTTCAGGGATG
Cre	GACATGTTCAGGGACAGGCA	GTTGTTCAGCTTGCACCAGG
Des	GTGGATGCAGCCACTCTAGC	TTAGCCGCGATGGTCTCATAC
Fabp4	CATCAGCGTAAATGGGGATT	CTTGTGGAAGTCACGCCTTT
Fgf10	TTTGGTGTCTTCGTTCCCTGT	TAGCTCCGCACATGCCTTC
Fizz1	GGAACTTCTTGCCAATCCAGC	AAGCACACCCAGTAGCAGTC
GFP	GAAGCCAACGCCTGCAAAATC	CCAACGGGTATGAGCTATTCC
Il1b	ACCCCAAAAGATGAAGGGCTG	TACTGCCTGCCTGAAGCTCT
Lpl	TTCCAGCCAGGATGCAACA	GGTCCACGTCTCCGAGTCC
mCherry	AAGGGCGAGATCAAGCAGAG	CCTCGTTGTGGGAGGTGATG
Parp1	GGCAGCCTGATGTTGAGGT	GCGTACTCCGCTAAAAAGTCAC
Pdgfrα	GTCGTTGACCTGCAGTGGA	CCAGCATGGTGATACCTTTGT
Plin2	CGACGACACCGATGAGTCCCAC	TCAGGTTGCGGGCGATAGCC
Polr2a	GCGGAATGGAAGCACGTTAAT	CCCAGCACAAAACACTCCTC
Pparg	CATCGAGGACATCCAAGACA	GGGTGGGACTTTCCTGCT
Sftpc	ACCCTGTGTGGAGAGCTACCA	TTTGCGGAGGGTCTTTCCT
Tcf21	GGCCAACGACAAGTACGAGA	GCTGTAGTTCCACACAAGCG
Thy1	TGCTCTCAGTCTTGCAGGTG	TGGATGGAGTTATCCTTGGTGTT
Tnfα	CATCTTCTCAAAATTCGAGTGACAA	TGGGAGTAGACAAGGTACAACCC
Vim	CCAACCTTTTCTTCCCTGAA	TGAGTGGGTGTCAACCAGAG
Zfp423	CAGGCCCACAAGAAGAACAAG	GTATCCTCGCAGTAGTCGCACA

4.15 Flow cytometry

For analyses of Plin2^{lin} cell populations, lungs were digested with Dispase and dissociated mechanically to generate lung cell suspensions, which were analyzed by flow cytometry upon staining with fluorescently labeled antibodies. Detailed protocol for flow cytometry and for sorting the cells is described in detail in the following paragraphs. In general, when washing steps had to be performed, samples were centrifuged at 500 g for 10 minutes, after which supernatant was removed.

4.16 Lung isolation and preparation of cell suspension

After, mice were sacrificed, chest was opened. Then, vena cava was opened for exsanguination. A small cut was made in the left heart ventricle; lungs were then perfused with Hanks' Balanced Salt solution (HBSS) via the right heart ventricle. Lungs were then filled with Dispase (~ 50-caseinolytic units/ml) intratracheally. Trachea was closed with surgical thread (SERAFLEX, Serag Wiessner, Germany) to prevent leaks. Afterwards, lungs were removed and placed in a 12-well plate with ~ 1 ml dispase (~ 50 caseinolytic units), in which lungs were partially digested to facilitate further dissociation. They were first incubated at RT for 40-45 minutes and after to stop further digestion lungs were transferred to 12-well plates containing fresh DMEM medium with 1 % (v/v) HEPES, 1 % Penicillin/Streptomycin (v/v) and DNase I (0.2 mg/ml). After separating lungs from the trachea and other organs, the lung lobes were transferred to gentleMACS C tubes containing 5 mL of the same DMEM medium and followed by mechanical dissociation with gentleMACS™ dissociator (Miltenyi Biotec, Bergisch Gladbach, Germany) using pre-loaded program (m-lung.01.01). Cell suspensions were sequentially filtered through 100 µm and 40 µm cell strainers. Then cell suspension were centrifuged at 500g for 10 minutes, pellets were resuspended in DMEM with 1% HEPES and stained immediately or stored at 4 °C for further analysis.

4.17 Immunofluorescent labeling for flow cytometry

To label cell populations of interest, 1–2 × 10^6 live cells were transferred to Eppendorf tubes prior to staining. For labeling of membrane-bound proteins, cells were washed and resuspended with 1× PBS containing 2 % FCS. Then, cells were incubated with an excess of anti-CD16/CD32 antibody (1:100) for 5 minutes at RT to block unwanted interactions between the other antibodies used and Fc receptors in the surface of certain cells. After blocking, cells were incubated with fluorophore-conjugated primary

antibodies for 15 minutes at 4 °C in darkness. Upon staining with antibodies, cells were resuspended in DMEM with 1 % HEPES and centrifuged again to get rid of unbounded antibodies. Right before the acquisition, 4′, 6 Diamidino-2-phenylindole (DAPI) (1:5000) was added to the samples for dead cell discrimination. Single-cell suspensions were analyzed either in a LSRFortessa™ Cell Analyzer (both from BD Biosciences, Franklin Lakes, USA) or BD FACSAria™ III, whenever sorting was intended, using the software FACSDiva (BD Biosciences, Franklin Lakes, USA) during acquisition. If possible, in experiments that required the use of fluorophores with spectral overlap, compensation was carried out using single stained samples containing antibody-capture compensation microbeads (OneCompeBeads™, Thermo Fisher Scientific, USA). Events positive for the various markers investigated were identified comparing fully stained samples with “fluorescence minus one (FMO) controls”. FMO controls contained all but not one of the all fluorophores present in fully stained sample. After acquisition, FlowJo 10.x software (FlowJo, Ashland, USA) was utilized to generate flow cytometry plots and histograms, and for quantitative evaluation of populations of interest.

4.18 Preparation of precision-cut lung slices from fixed organs

Thick mouse lung sections (or precision-cut lung slices, PCLS) were employed for 3D imaging of cells and tissue. To prepare lung thick sections, lungs were perfused post-mortem with PBS 1× via the right ventricle. Lungs were then inflated intratracheally with low gelling temperature agarose (Merck, Germany) 4 % (w/v) in PBS 1× containing 1.5 % PFA (w/v). Trachea was closed to prevent leakage and lungs were transferred to PFA 2 % (w/v) in solution with PBS 1× at 4 °C for overnight and then transferred to PBS 1×. Then separate lobes were embedded in blocks of regular agarose (Carl Roth, Germany) 1 % (w/v) in PBS 1× and incubated at 4 °C until blocks became solid. Afterwards, blocks were cut into 150 µm slabs with a VT1200S vibratome (Leica, Germany). Slabs were subsequently transferred to PBS 1× for storage until further use.

4.19 Immunofluorescent staining of PCLS

Generally, PCLS were stained with fluorescent either antibodies or dyes. Sections were washed three times with PBS 1× before blocking with a solution containing 0.5 % (w/v) BSA and 0.5 % (v/v) Triton X-100. Incubation with primary antibodies (a list of the antibodies can be found in table 6) was then carried out overnight at 4 °C followed

by 3 washes with PBST 1×. If necessary, sections were then stained with secondary antibodies raised against the primary antibody's isotype. DAPI (2 µM) was added to the secondary antibody solution (or directly-labeled primary antibody solution) if required as nuclear stain. Finally, three more washing steps were performed on the sections with PBST 1×, which were then mounted on slides with fluoromount W (Serva, Germany) using properly-sized spacers (SunJin Lab, Taiwan).

4.20 Image processing, analysis and figures preparation

Once stained, whole lung slides were scanned (10×, 20× and 40×) and digitized to virtual slides using a NanoZoomer-XR C12000 (Hamamatsu Photonics, Japan).

FIJI/ImageJ was used to perform adjustments of brightness and contrast to epi fluorescent and confocal images as well as for generating 3D renderings and projections of z-stacks.

Graphs were prepared with the software Prism (Graphpad Software Inc., v6–8.x) and figures were assembled using the Adobe Illustrator program 2022.

4.21 ScRNAseq sample preparation and data analysis

Sorted cells were counted using MoxiTM Z cell counter (VWR, ORFLMXZ001) and diluted according to the manufacturer's protocol. Cell separation was done by using the 10x Chromium platform with Next GEM Single Cell 3′ Reagent kit (10× Genomics) following the manufacturer's recommendations and targeting 10000 cells per sample. Next-generation sequencing was performed using Nextseq500 (Illumina). Reads with a quality of less than 30 (<0.3 %) were filtered out. Subsequent read processing was conducted using scRNAseq implementation of STAR solo and reads were aligned to the mm10 mouse reference genome (Dobin et al., 2013). Preprocessed counts were further analyzed using Scanpy (Wolf et al., 2018). General cell quality control was conducted by taking the number of detected genes and mitochondrial content per cell into consideration. Cells with less than 300 detected genes or mitochondrial content greater than 8 % were removed. Raw counts per cell were normalized to the median count over all cells and transformed into logarithmic values to stabilize the variance. Dimension reduction was carried out using PCA and 50 principal components were retained. Subsequent visualization by the uniform manifold approximation and projection (UMAP), feature reduction method and preliminary cell clustering via

community detection were based on the initial PC calculation (Leland McInnes and Großberger, 2018; Traag et al., 2019). Final cell clusters were fine-tuned based on known marker genes expression followed by manual cell type annotation (Du et al., 2015; Zhang et al., 2018). Additional Differential expressed genes (DEGs) comparison was performed for cluster pairs of interest with Scanpy package. All following data visualization was carried out by CellxGene package (DOI 10.5281/zenodo.3235020).

4.22 Statistics

Statistical analyses were performed on Prism v6–8.x. Data are presented as mean ± SD. Differences were evaluated with t-test (unpaired, unless noted) for comparisons between two groups. P values lower than 0.05 were considered statistically significant.

5 Results

Previously, Plin2^{creERT2}; R26$^{(mTmG)/+}$ mice were employed to confirm function of the generated mouse line and to investigate phenotypic features and localization of cells of the Plin2 cell lineage (Plin2^{lin}) cells within the mesenchyme of the murine lung (Ntokou et al., 2017). To further delineate the role of Plin2^{+} cells in alveolarization during late lung development, this Plin2^{creERT2} cre-driver line was employed in combination with different cre recombinase responsive strains in this work.

5.1 Depletion of Plin2^{+} cells using Plin2^{creERT2}; R26^{DTA} mice

To analyze function of Plin2^{+} cells, Plin2^{+} cells were depleted during alveolarization and in adult mice to analyze the impact of loss of Plin2^{+} cells on change in lung morphology.

5.1.1 Depletion of Plin2^{+} cells during postnatal lung development

To investigate the role of Plin2^{lin} cells during alveolarization, it was aimed to deplete Plin2-expressing cells in neonates. Therefore, Plin2^{creERT2}; R26^{DTA} and control mice were injected with a single dose Tmx injection at P5 and organs e.g. lung, liver, kidney and spleen were harvested at P8 (n = 3). Initially, the objective was to investigate impact of depletion in lungs at P14, however due to the pathological symptoms of the neonates e.g. stillness, few milk in stomach and pale skin color, the experiment had to be ended earlier.

5.1.1.1 Morphology of lungs, liver, kidneys and spleen of Plin2^{+} cell depleted neonatal mice

Lungs during late development are passing through a very dynamic cellular and molecular phase. Hence, lung structure is also undergoing rapid changes. To distinguish Plin2^{+} cells depletion-based potential impact on structural changes at P8 from development-based structural changes, different controls were considered. P5 Plin2^{creERT2} mice positive or negative for DTA without Tmx injection were included as controls for development-based structural changes (Figure. 9 A, C). P8 Plin2^{creERT2} mice negative for DTA with Tmx injection were considered as control for cre recombination. Since these mice lack the DTA-expressing gene, after Tmx injection, no DTA can be expressed and consequently Plin2^{+} cells would not be depleted. Therefore, figure 9 B represents intact lung structure at P8 developmental stage.

Looking at lung samples from P8 Plin2$^{creERT2-}$ mice positive for DTA, these mice did not no show any significant changes after Tmx administration (Figure. 9 D).

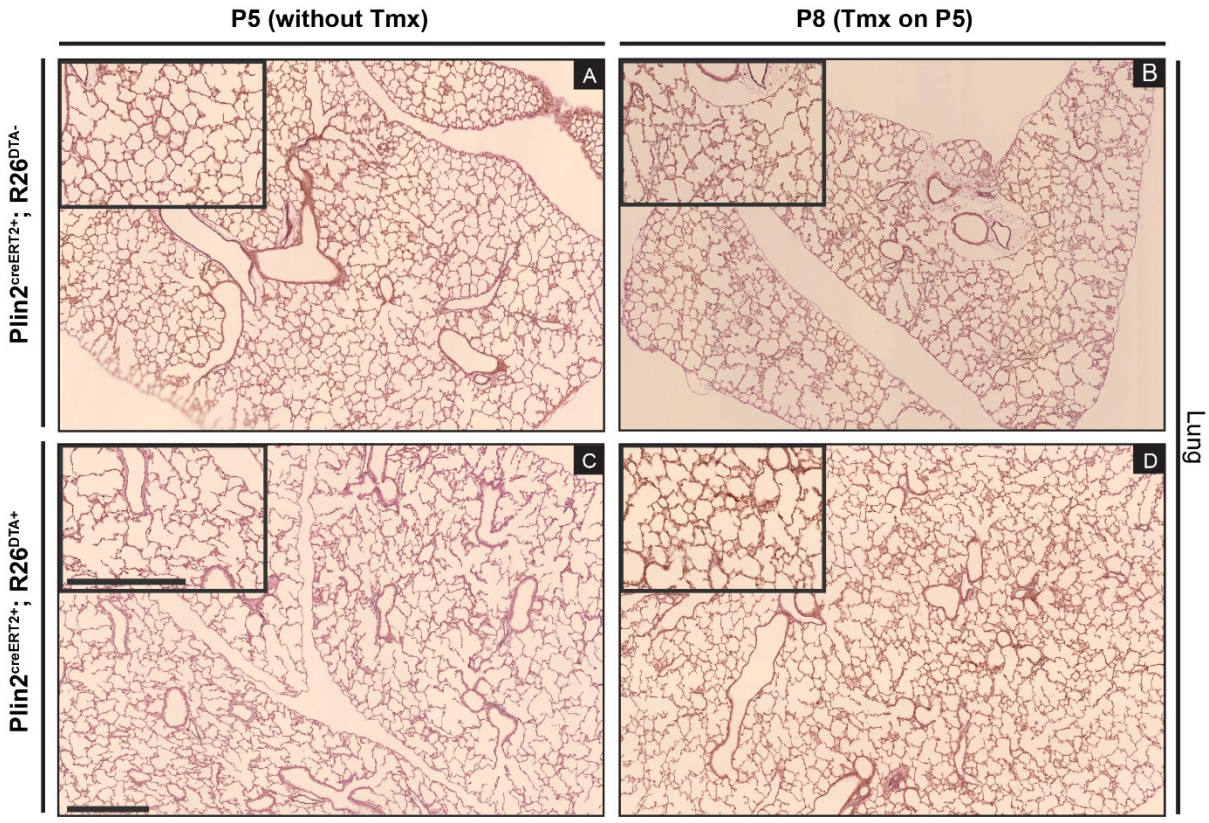

Figure 9. Assessment of structural changes in neonatal mouse lung of Plin2^{+} cell depleted and control mice. Neonates were injected by Tmx at postnatal day (P) 5. Histological H and E staining was performed on Plin2$^{creERT2+}$; R26^{DTA-} and Plin2$^{creERT2/+}$; R26^{DTA+} in neonatal lungs. (A, B) Controls for DTA^{-} lung structure at P5 and P8 respectively; (C) Control for DTA^{+} lung structure at P5, and (D) lung structure of cell depleted mice at P8. Scale bar = 250 µm

Other organs in neonates e.g. liver, kidney and spleen were harvested for histological analysis, since they also express Plin2 to some extends. Following three figures are showing Hematoxylin and Eosin (H & E) staining of paraffin sections from those organs. Investigating other organs, the same experimental set up as above was kept according to have both types of controls.

Looking at the liver samples from Plin2^{+} cell depleted mice, livers of cell-depleted mice depicted pathological features that are common in fatty livers. P5 Plin2^{creERT2} mice positive or negative for DTA without Tmx injection were included as controls for development-based structural changes (Figure. 10 A, C). P8 Plin2^{creERT2} mice negative for DTA with Tmx injection were considered as control for cre recombination (Figure.

10 B). Histopathology of liver tissues showed micro-vesicular steatosis-like phenotype, which appeared as empty white bodies. In figure 10 D, green circles point to some of these vesicles. Based on the observation, it can be concluded that attempt to deplete Plin2-expressing cells in the lung caused a pathological phenotype in liver and liver structure from Plin2^{+} depleted mice was altered.

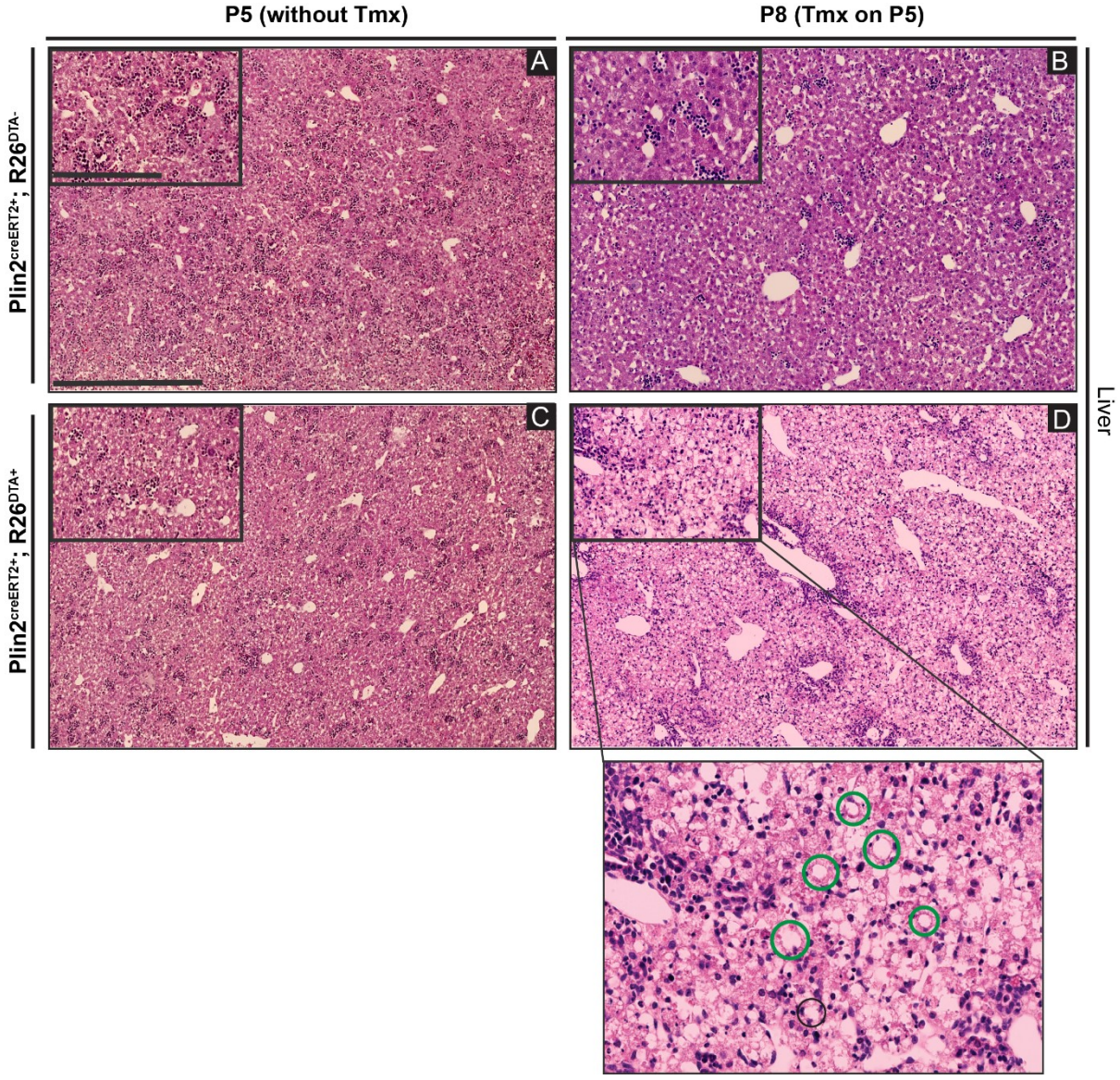

Figure 10. Assessment of structural changes in neonatal mouse liver Plin2^{+} cell depleted and control mice. Neonates were injected by Tmx at postnatal day (P) 5. Histological H and E staining was performed on Plin2$^{creERT2+;}$ R26^{DTA-} and Plin2$^{creERT2/+}$; R26^{DTA+} in neonatal livers. (A, B) Controls for DTA^{-} liver structure at P5 and P8 respectively; (C) Control for DTA^{+} liver structure at P5, and (D) Liver structure of cell depleted mice at P8. Green circles indicate the micro-vesicles, which contain lipid and pushing the nucleus to the side of the cell. Scale bar = 250 µm.

Observations of kidney samples from Plin2^{+} cell depleted mice demonstrated that kidneys of cell-depleted mice did not undergo any structural changes. P5 Plin2^{creERT2} mice positive or negative for DTA without Tmx injection were included as controls for development-based structural changes (Figure. 11 A, C). P8 Plin2^{creERT2} mice negative for DTA with Tmx injection were considered as control for cre recombination (Figure. 11 B). P8 Plin2^{creERT2} mouse kidneys positive for DTA did not no show any significant changes in kidney structure after Tmx administration (Figure. 11 D).

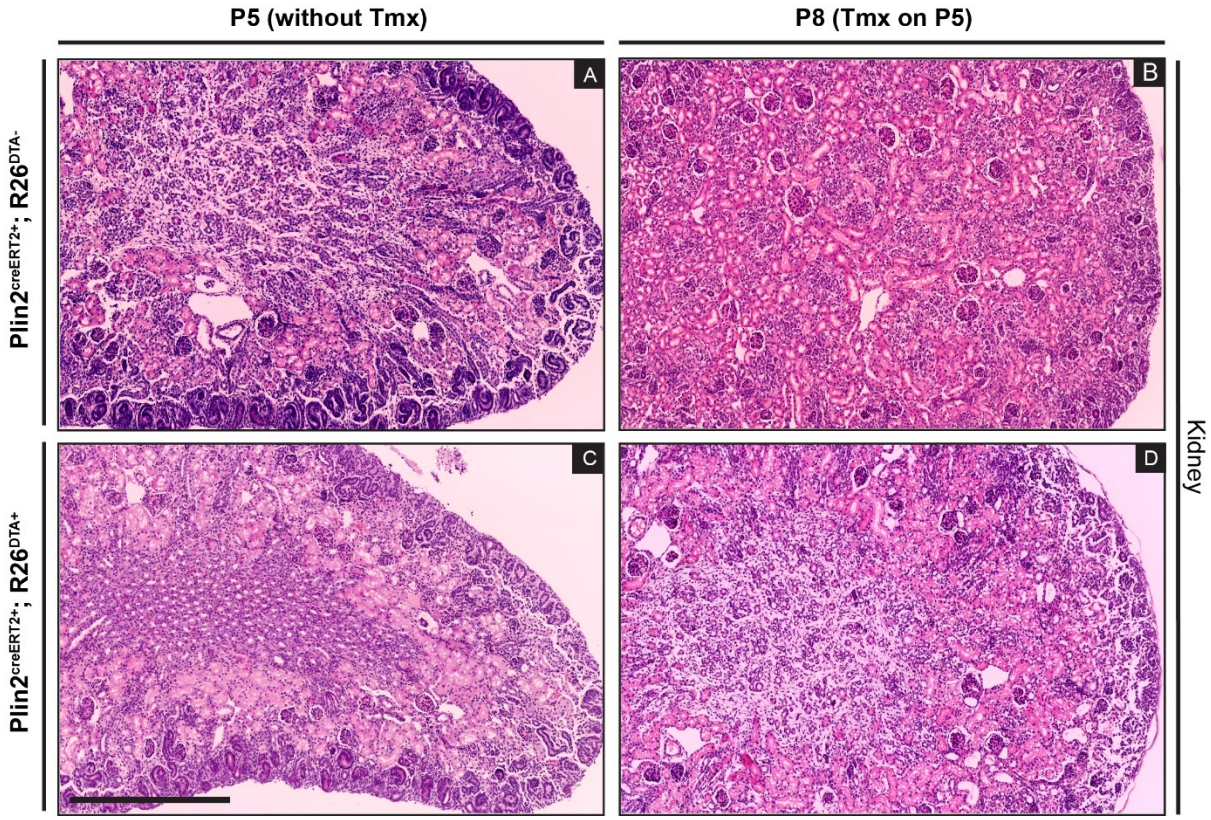

Figure 11. Assessment of structural changes in neonatal mouse kidney of Plin2^{+} cell depleted and control mice. Neonates were injected by Tmx at postnatal day (P) 5. Histological H and E staining was performed on Plin2$^{creERT2+}$; R26^{DTA-} and Plin2$^{creERT2/+}$; R26^{DTA+} in neonatal kidneys. (A, B) Controls for DTA^{-} kidney structure at P5 and P8 respectively; (C) Control for DTA^{+} kidney structure at P5, and (D) Kidney structure of cell depleted mice at P8. Scale bar = 250 µm.

Investigating spleen samples from Plin2^{+} cell depleted mice was followed with all proper controls. P5 Plin2^{creERT2} mice positive or negative for DTA without Tmx injection were included as controls for development-based structural changes in spleen (Figure. 12 A, C). P8 Plin2^{creERT2} mice negative for DTA with Tmx injection were considered as control for cre recombination (Figure. 12 B). P8 Plin2^{creERT2} mice spleens positive for

DTA did not no show any significant changes in spleen structure after Tmx administration (Figure. 12 D).

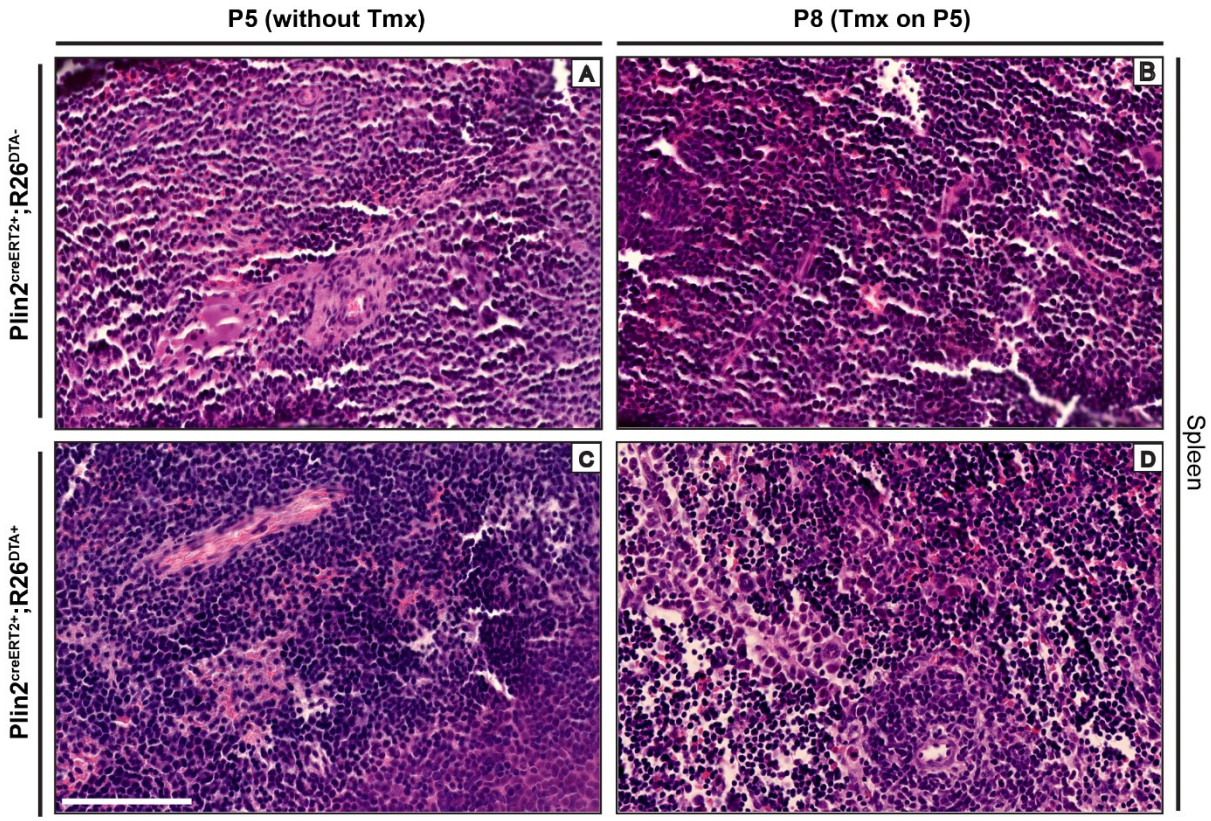

Figure 12. Assessment of structural changes in neonatal mouse spleen of Plin2$^+$ cell depleted and control mice. Neonates were injected by Tmx at postnatal day (P) 5. Histological H and E staining was performed on Plin2$^{creERT2+}$; R26^{DTA-} and Plin2$^{creERT2/+}$; R26^{DTA+} in neonatal spleens. (A, B) Controls for DTA$^-$ spleen structure at P5 and P8 respectively; (C) Control for DTA$^+$ spleen structure at P5, and (D) Spleen structure of cell depleted mice at P8. Scale bar = 250 µm.

5.1.1.2 Quantitative analysis of Plin2$^+$ cell depletion in postnatal lungs

Attempts to deplete Plin2$^+$ cells in the lung to analyze impact or any structural phenotype during alveolarization did not lead to structural alterations in the lung. However, structure of livers from Plin2$^+$ cell depleted mice was altered. This raised the question if tamoxifen administration and cre-activation did cause ablation of Plin2$^+$ cells in the lung at all. Therefore, Plin2-driven mCherry$^+$ cells were quantified by flow cytometry in Plin2$^+$ cell depleted lungs and control lungs. It was observed that the number of mCherry$^+$ cells did not significantly change in Plin2$^+$ cell depleted versus control lungs (Fig. 13).

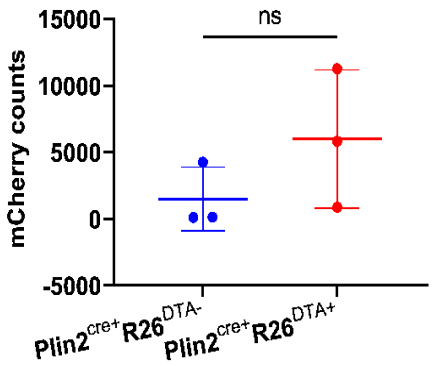

Figure 13. Quantification of mCherry⁺ cells from lungs of postnatal Plin2⁺ cell depleted and control mice. Quantification of mCherry⁺ cells using endogenous mCherry fluorescent as actual Plin2⁺ cell counts in Plin2⁺ depleted mice (Plin2^{cre+};R26$^{DTA+)}$ vs controls (Plin2^{cre+}; R26^{DTA-}). All mice were injected with Tmx at P5 and harvested lungs at P8 were used for quantification of mCherry⁺ cells by flow cytometry. Data represent mean ± SD. Unpaired t-test was used and P-value < 0.05 was defined as statistically significant.

5.1.1.3 Gene expression analyses of lungs and livers from Plin2⁺ cell depleted and control neonatal mice

Investigating molecular changes upon Tmx administration in neonatal lung and liver tissues from Plin2⁺ depleted and control mice were pursued by gene expression analysis. First, expression of mCherry and Plin2 genes was analyzed in lung samples from Plin2^{cre+}R26^{DTA+} and Plin2^{cre+}R26^{DTA-} mice at P8 which were injected with Tmx at P5. Unexpectedly, Plin2 expression was significantly higher in Plin2⁺ cell depleted mice compare to control mice but mCherry did not show any significant changes between depleted and control mice (Fig. 14 A). To further investigate whether tamoxifen injection affected mesenchymal fibroblast populations in the lung, expression of fibroblast markers such as Col1a1 and Pdgfrα were analyzed, which did not show any changes between the two groups (Fig. 14 B). Since the used cre driver line Plin2^{creERT2} has been shown to target lipofibroblasts in the lung, expression of lipofibroblast-related genes was explored next. Except Tcf21, fatty acid binding protein4 (Fabp4) and lipoprotein lipase (Lpl), which were upregulated in depleted mice in comparison to control mice, other genes did not demonstrate significant changes in depleted mice versus control mice (Fig. 14 C).

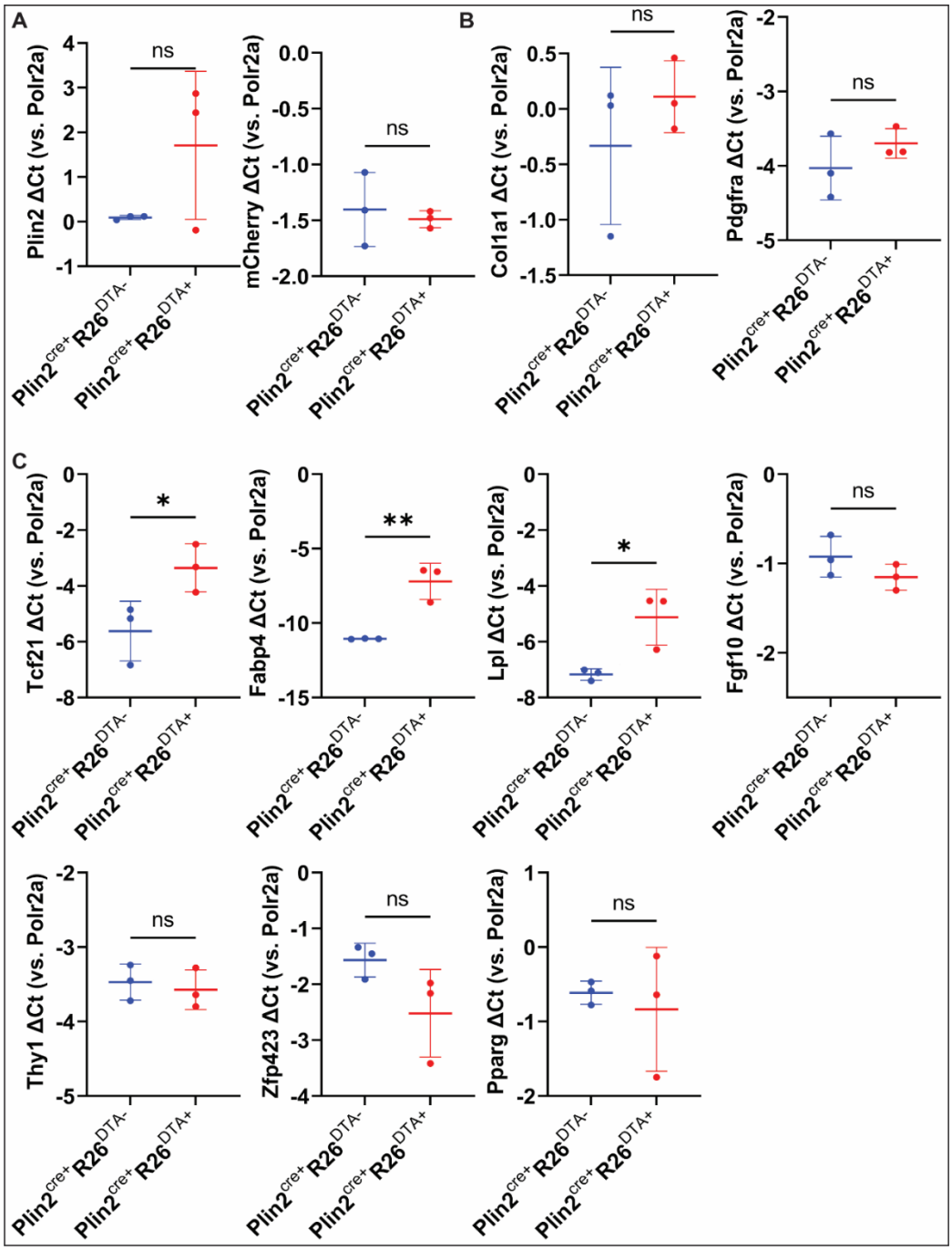

Figure 14. Assessment of fibroblast-related gene expression in postnatal lungs of Plin2⁺ cell depleted and control mice. Plin2^{cre+}; R26^{DTA+} and Plin2^{cre+}; R26^{DTA-} postnatal mice were injected with Tmx at P5. Lungs were harvested at P8 and used for gene expression analysis by qPCR. Comparison of expression levels in Plin2^{cre+}; R26^{DTA+} vs Plin2^{cre+}; R26^{DTA-} for (A) Plin2 and mCherry genes; (B) Fibroblast markers: Col1a1 and Pdgfra (C) Lipofibroblast markers: Tcf21, Pparg, Thy1, Fgf10, Fabp4, Zfp423, Lpl. Polr2a was used as housekeeping gene. Data represent mean ± SD. Unpaired t-test was used and P-values < 0.05 was defined as statistically significant.

Next the expression level of inflammatory markers such as tumor necrosis factor (Tnfa), interleukin 1 beta (Il 1b), resistin like α (Fizz1) and arginase 1 (Arg1) were

analyzed. Results showed that only the Arg1 gene was down regulated in depleted mice versus control mice (Figure. 15 A).

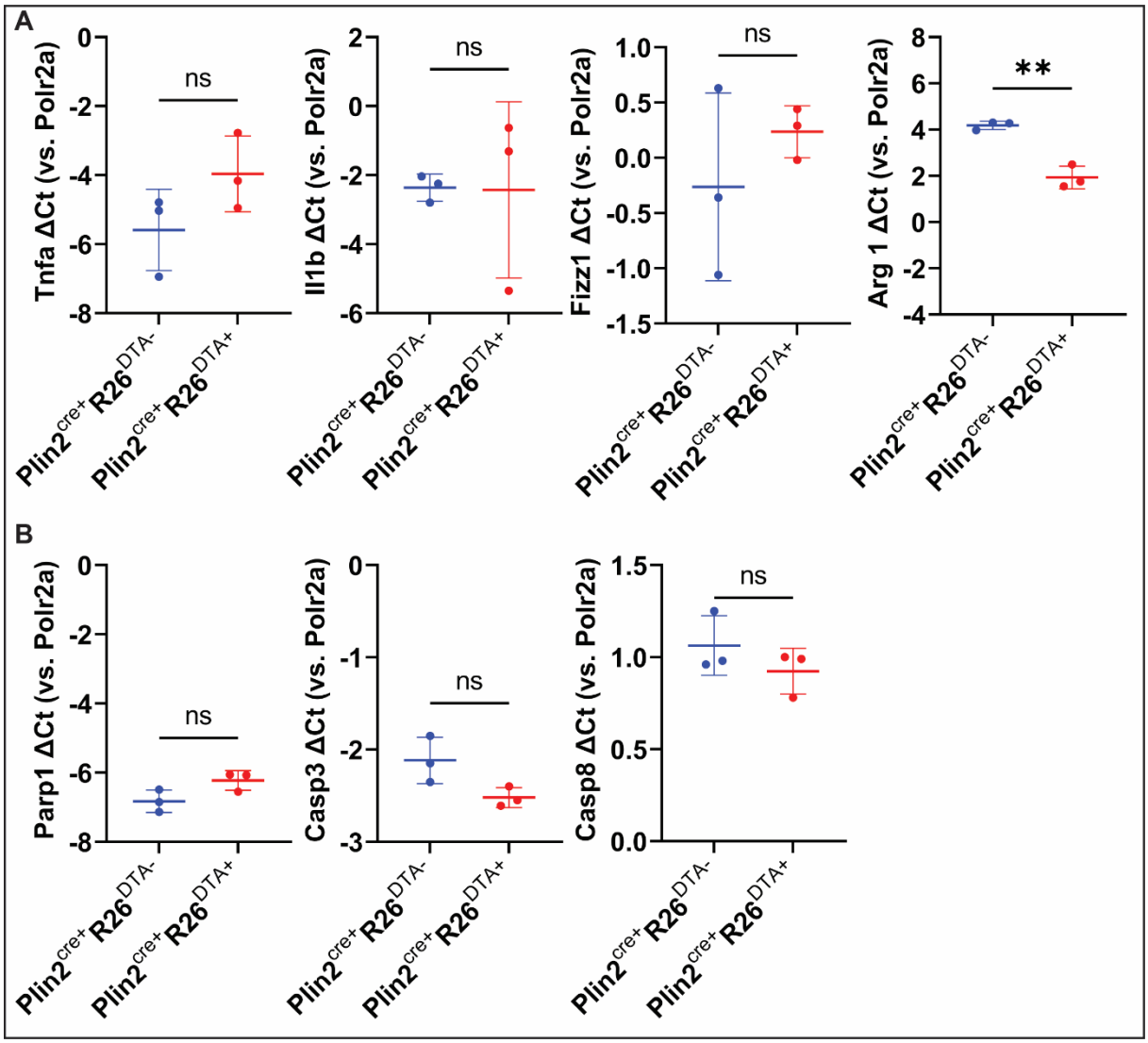

Figure 15. Assessment of gene expression of inflammatory and apoptotic processes in postnatal lungs of Plin2⁺ cell depleted and control mice. Plin2^{cre+}; R26^{DTA+} and Plin2^{cre+}; R26^{DTA-} postnatal mice were injected with Tmx at P5. Lungs were harvested at P8 used for gene expression analysis by qPCR. Comparison of expression levels in Plin2^{cre+}; R26^{DTA+} vs Plin2^{cre+}; R26^{DTA-} for (A) Inflammatory markers; Tnfa, Il1b, Fizz1, Arg1. (B) Apoptotic markers; Parp1, Casp3, Casp8. Polr2a was used as housekeeping gene. Data represent mean ± SD. Unpaired t-test was used and P-values < 0.05 was defined as statistically significant.

Since expression of diphtheria toxin A (DTA) in cells as a toxin stimulates programmed cell death, markers for apoptosis were evaluated next. Expression of genes such as poly ADP-Ribose polymerase 1 (parp1), cysteine-aspartic acid protease 3 and 8 (Casp 3 and 8) were investigated. None of these three genes was expressed significantly different in depleted mice versus control mice (Figure. 15 B).

Due to the fact that a pathologic organ structure was only observed in liver samples, gene expression analysis was carried out additionally on liver tissue, Therefore, same fibroblast-related gene set was analyzed in liver tissue homogenates. Plin2 and Plin2-driven mCherry reporter gene did not show significant changes in expression in liver samples from depleted versus control postnatal mice (Figure. 16 A). Likewise, expression of mesenchymal fibroblast markers Col1a1 and Pdgfrα did not change between groups (Figure. 16 B). Only expression of Tcf21 and Lpl among the other lipofibroblast-related markers was down regulated in depleted mice compare to control mice (Figure. 16 C). Moreover, expression of inflammatory genes was also assessed in postnatal liver samples. Results indicated significant upregulation of Tnfa expression in depleted mice versus control mice (Fig. 17 A). Apoptosis inspection showed downregulation of Parp1 in depleted mice compare to control mice (Fig. 17 B).

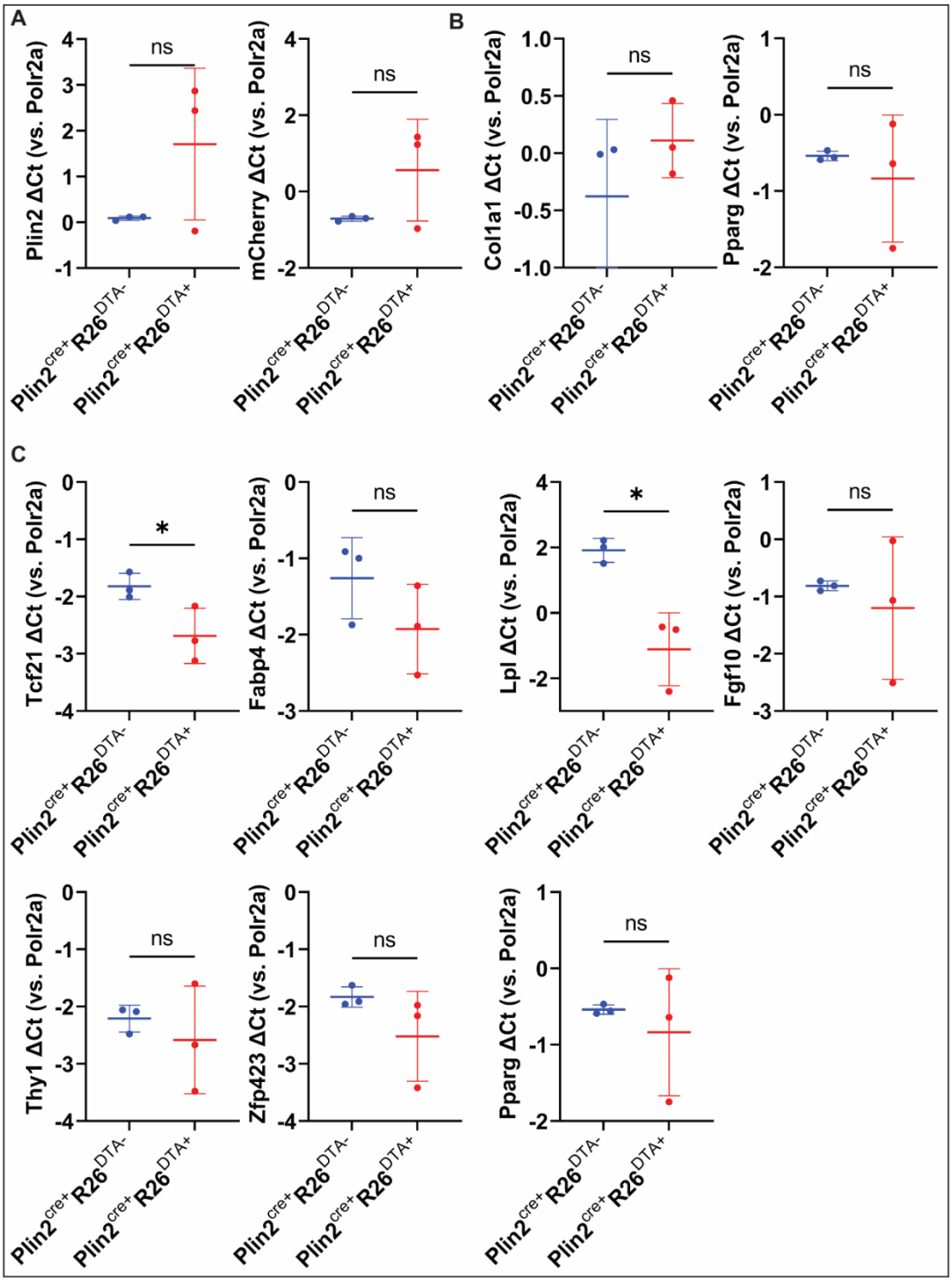

Figure 16. Assessment of fibroblast-related gene expression in postnatal livers of Plin2^{+} cell depleted and control mice. Plin2^{cre+}R26^{DTA+} and Plin2^{cre+}R26^{DTA-} postnatal mice were injected with Tmx at P5. Livers were harvested at P8 and used for gene expression analysis by qPCR. Comparison of expression levels in Plin2^{cre+}R26^{DTA+} vs Plin2^{cre+}R26^{DTA-} for (A) Plin2 and mCherry genes; (B) Fibroblast markers: Col1a1 and Pdgfra (C) Lipofibroblast markers: Tcf21, Pparg, Thy1, Fgf10, Fabp4, Zfp423, Lpl. Polr2a was used as housekeeping gene. Data represent mean ± SD. Unpaired t-test was used and P-values < 0.05 was defined as statistically significant.

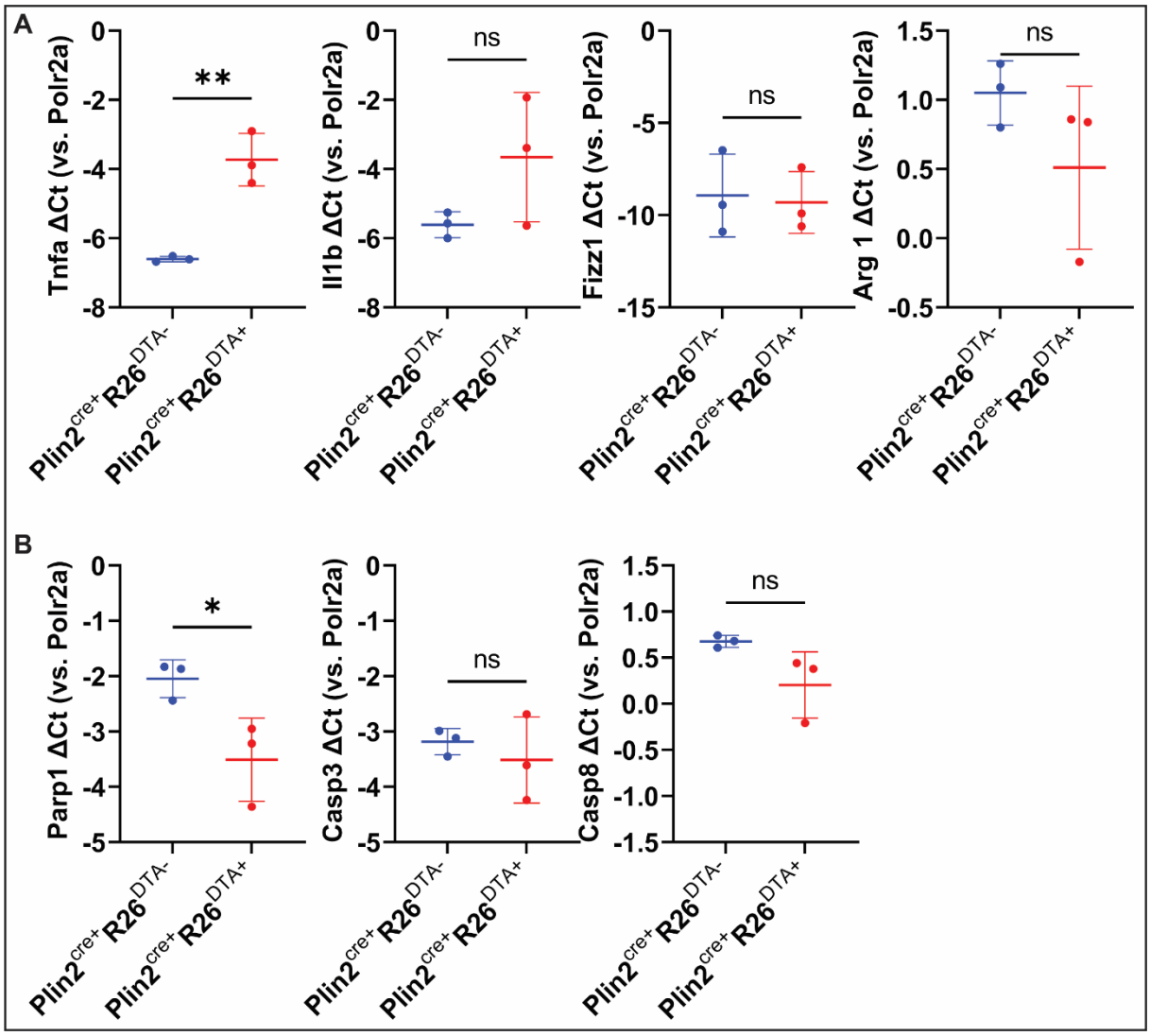

Figure 17. Assessment of gene expression of inflammatory and apoptotic processes in postnatal livers of Plin2⁺ cell depleted and control mice. Plin2^{cre+}; R26^{DTA+} and Plin2^{cre+}; R26^{DTA-} postnatal mice were injected with Tmx at P5. Livers were harvested at P8 used for gene expression analysis by qPCR. Comparison of expression levels in Plin2^{cre+}; R26^{DTA+} vs Plin2^{cre+}; R26^{DTA-} for (A) Inflammatory markers; Tnfa, Il1b, Fizz1, Arg1. (B) Apoptotic markers; Parp1, Casp3, Casp8. Polr2a was used as housekeeping gene. Data represent mean ± SD. Unpaired t-test was used and P-values < 0.05 was defined as statistically significant.

5.1.2 Depletion of Plin2⁺ cells in adult mice

Since depletion of Plin2⁺ cells in neonatal lungs could not be achieved, Plin2⁺ cells were depleted during lung homeostasis in adult mice. To evaluate lung structure after Plin2⁺ cell depletion, adult Plin2$^{creERT2+}$; R26^{DTA+} and Plin2$^{creERT2+}$; R26^{DTA-} mice were injected with a single intraperitoneal Tmx injection. An injected Plin2$^{creERT2+}$; R26^{DTA-} mouse was used as control mouse (Figure. 18 A, C, E and G).

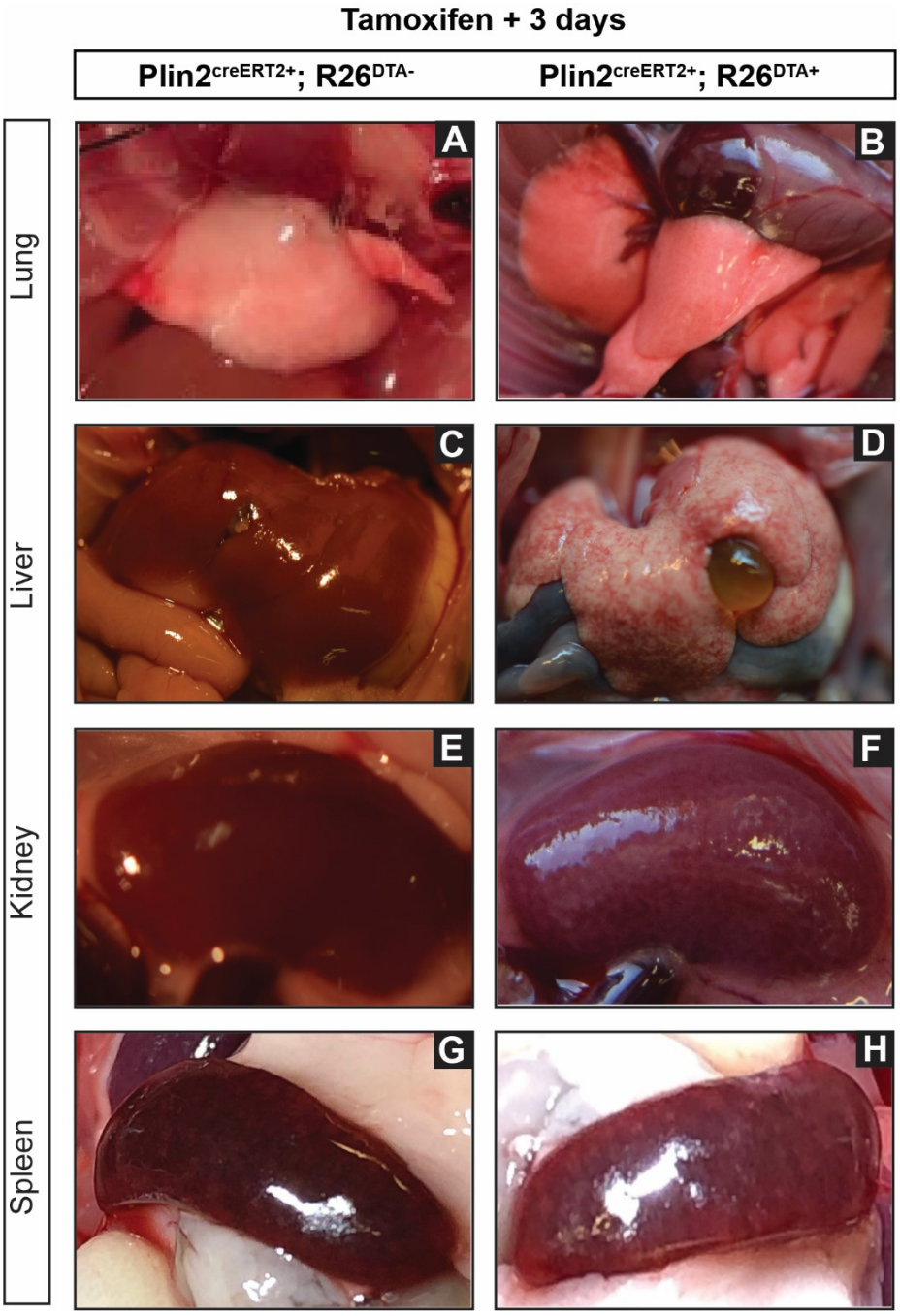

Figure 18. Macroscopic phenotype of adult mouse organs after Tmx injection in Plin2^{+} cell depleted and control mice. Plin2^{cre+}; R26^{DTA+} and Plin2^{cre+}; R26^{DTA-} adult mice were injected with Tmx and organs were harvested 3 days after injection. (A, B) Lung (C, D) Liver (E, F) Kidney and (G, H) Spleen.

Mice had to be sacrificed 3 days after injection since the cell depleted mouse showed sickness symptoms like coat staring, being less alert and being aggressive upon provoking. Macroscopic inspection of the organs revealed an altered liver appearance representing strong liver failure upon Plin2^{+} cell depletion compare to a control liver (Figure. 18 E, F). Macroscopic inspection of other abdominal organs e.g. kidney (Figure. 18 C, D) and spleen (Figure. 18 G, H) did not show any deformities.

In adult mice, also histological analysis was performed on the lung and other organs in order to evaluate the impact of Tmx injection on lung structure and other organs morphology.

First, elastica staining was performed on 5-µm thick paraffin sections of the lungs of Plin2^{+} cell depleted versus control mice. Since elastica staining stains elastic fibers presented at tip of alveolar septa, any structural changes of the lung could easier be detected. No significant changes in septal morphology in Plin2^{+} cell depleted lung were observed versus the control lung (Figure. 19 A, B).

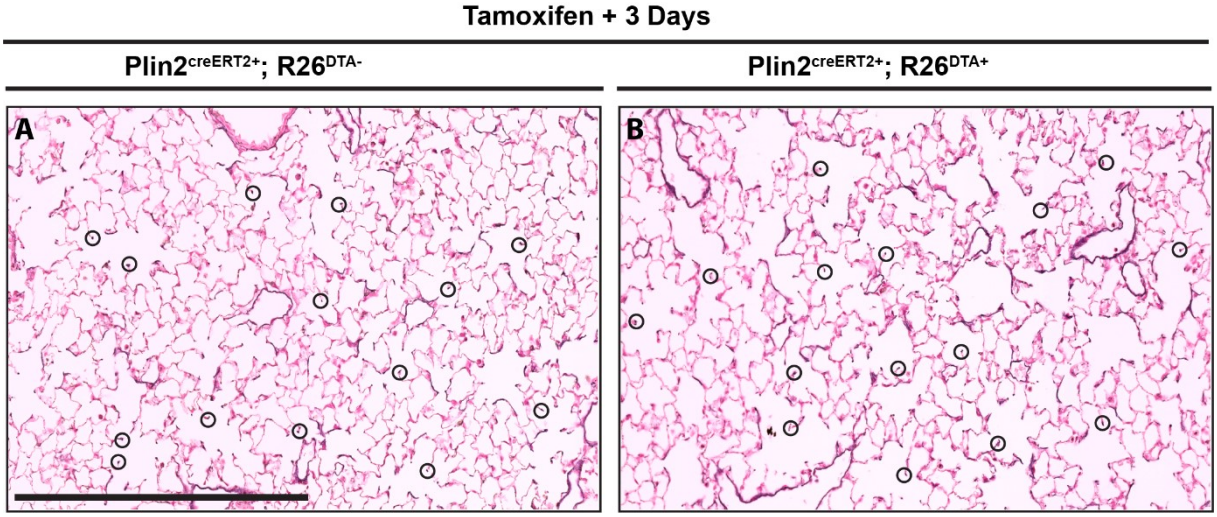

Figure 19. Assessment of elastin deposition in the adult mouse lung of Plin2^{+} cell depleted and control mice. Plin2^{cre+}; R26^{DTA+} and Plin2^{cre+}; R26^{DTA-} adult mice were injected with Tmx and lung was harvested 3 days after injection. Elastica staining was used to stain elastin fibers in lung paraffin sections. Circles show elastin fibers at the tips of alveolar septa in (A) Control and (B) Depleted mice. Scale bar = 250 µm.

Next, H & E staining was applied on lung and other organs paraffin sections. There were no significant changes observed in the structure of lung, kidney and spleen of Plin2^{+} cell depleted versus control samples (Figure. 20 A, B and E- H). However, liver

structure differed significantly in Plin2^{+} cell depleted mice compared to the control mice demonstrating signs of strong liver failure. (Fig 20. C, D).

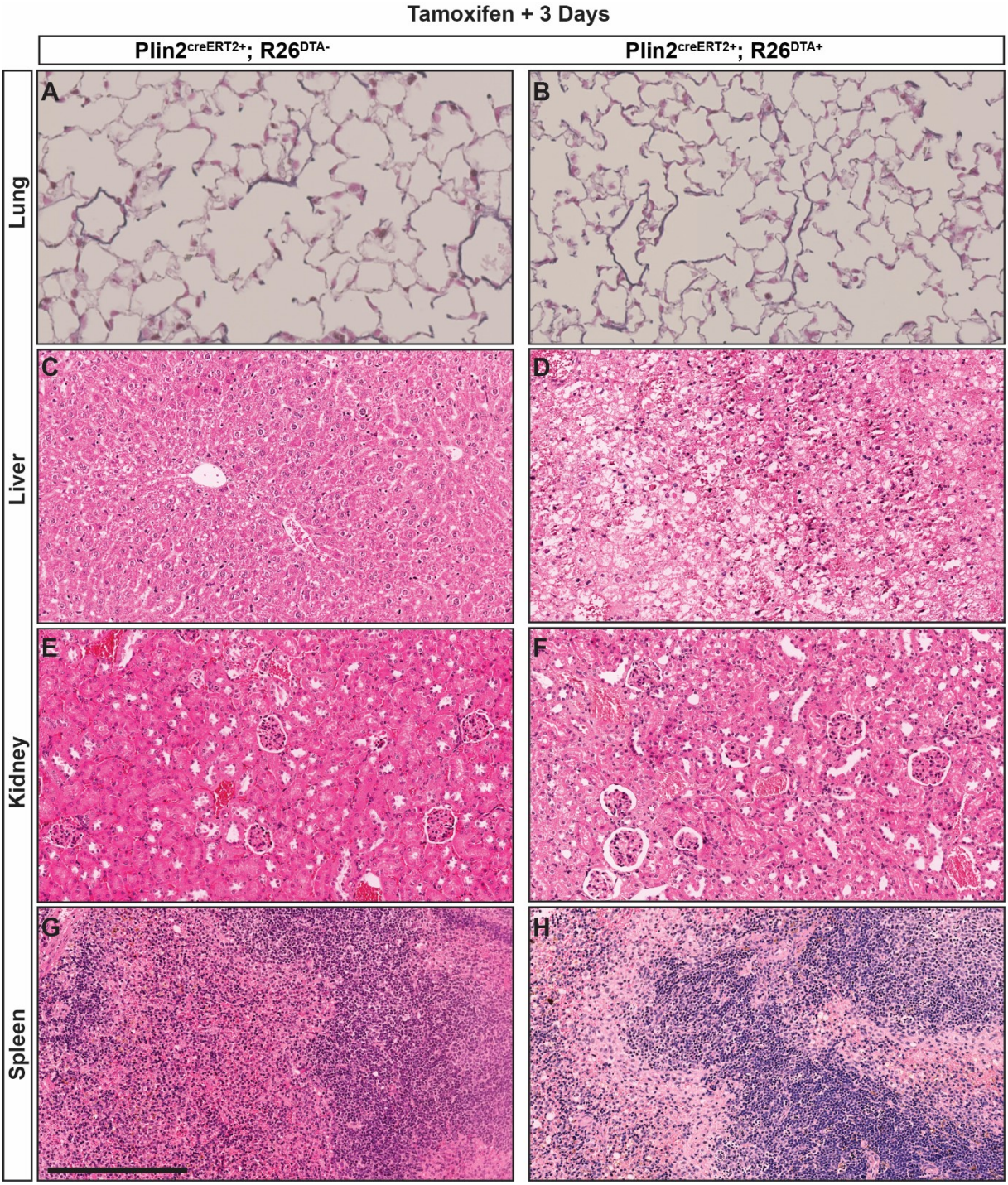

Figure 20. **Assessment of structural changes in organs of Plin2^{+} cell depleted and control adult mice.** Plin2$^{creERT2+}$; R26^{DTA+} and Plin2$^{creERT2+}$; R26^{DTA-} adult mice were injected with Tmx and lung and other organs were harvested 3 days after injection. Histological H & E staining (A, B) Lung (C, D) Liver (E, F) Kidney (G, H) Spleen. Paraffin sections show significant morphological changes in liver tissue structure of Plin2^{+} cell depleted mouse compare to control mouse. Scale bar = 25 µm.

Summarizing Plin2^{+} cell depletion experiments in postnatal and adult mice indicated that tamoxifen administration to deplete Plin2^{+} cells in the lung did not lead to cell depletion and morphological changes in the lung. Therefore, the Plin2^{+} cell depletion approach was not followed further.

5.2 Labeling of the Plin2^{+} cell lineage in adult mice

Using a cell depletion approach, Plin2^{+} cells could not be depleted in the lung upon Tmx injection of Plin2$^{creERT2+}$; R26^{DTA+} mice. However, a strong phenotype in the liver of liver failure upon Plin2^{+} cell depletion suggested Plin2^{+} cell depletion in the liver. Based on these observations, it should be tested, whether cre recombination using Plin2^{creERT2} mice could be achieved in lung and liver. To test this, Plin2$^{creERT2+}$; R26^{mTmG+} adult mice received a single dose of Tmx i.p. and were sacrificed three days after the injection.

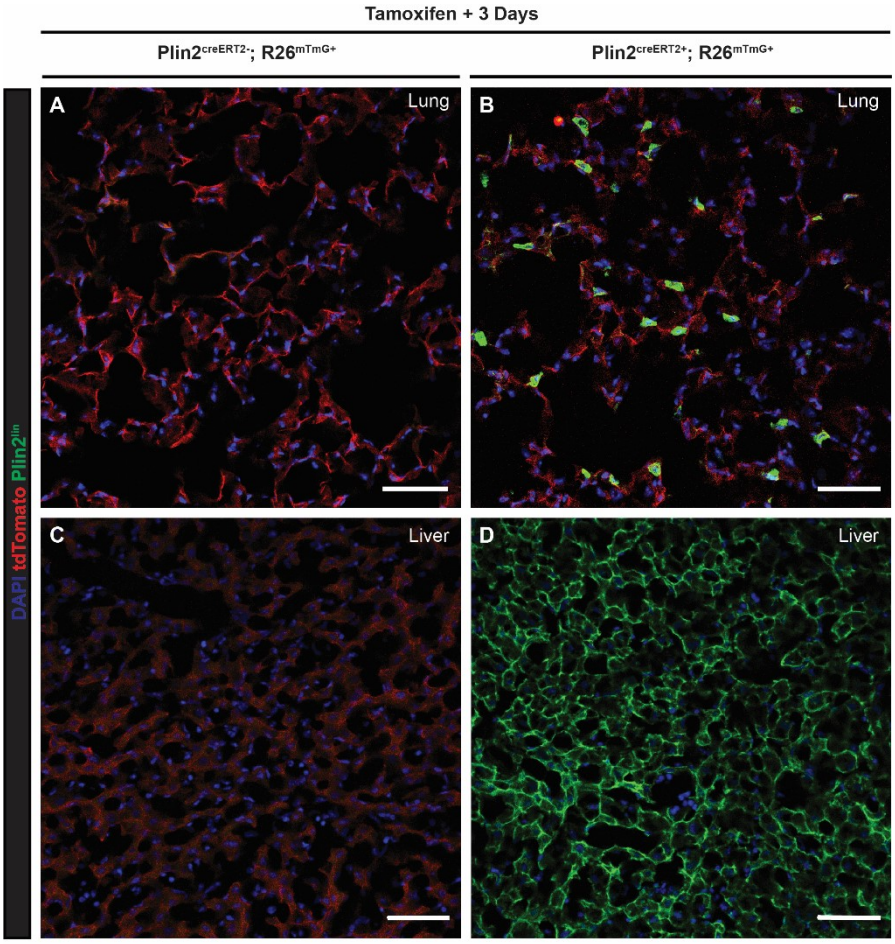

Figure 21. Cre recombination in Plin2$^{creERT2+}$; R26^{mTmG+} adult mice. (A) Plin$^{creERT2+}$ mice were bred with R26^{mTmG+} global reporter to generate inducible Plin2^{lin} reporter mice (Plin$^{creERT2+}$; R26^{mTmG+}). Cre-recombination was induced in adult mice with a single dose of Tmx injection. Lung and liver were

harvested 3 days after Tmx injection and used for immunofluorescence (IF) analysis. (A, B) Representative cryosections from lung samples (D, E) from liver samples show constant tdTomato expression in both Plin2$^{creERT2-}$; R26^{mTmG+}and Plin2$^{creERT2+}$; R26^{mTmG+} mice. eGFP was expressed in Plin2$^{creERT2+}$; R26^{mTmG+} mice only after Tmx administration. GFP (Green), tdTomato (Red) and nuclear stain DAPI (Blue) Scale bar = 50µm.

Cre negative animals did serve as negative control for cre-dependent recombination. GFP could be detected in adult lungs by immunofluorescent CLSM imaging; it was found also extensively throughout the liver tissue (Figure. 21 A, B). GFP was also found extensively expressed throughout liver tissue (Figure. 21 C, D). These observations outline that cre recombination in the lung works upon Tmx induction, when liver is not damaged.

In order to label cells of the Plin2 cell lineage (Plin2^{lin}), Plin$^{creERT2+}$; R26^{mTmG+} mice were injected with Tmx at P1 and postnatal lungs were harvested at the peak of secondary septation (P7) and the end of bulk secondary septation (P14). Samples were further subjected to single cell RNA sequencing analysis (n = 1), IF staining and CLSM imaging (n = 3) (Figure. 22 A).

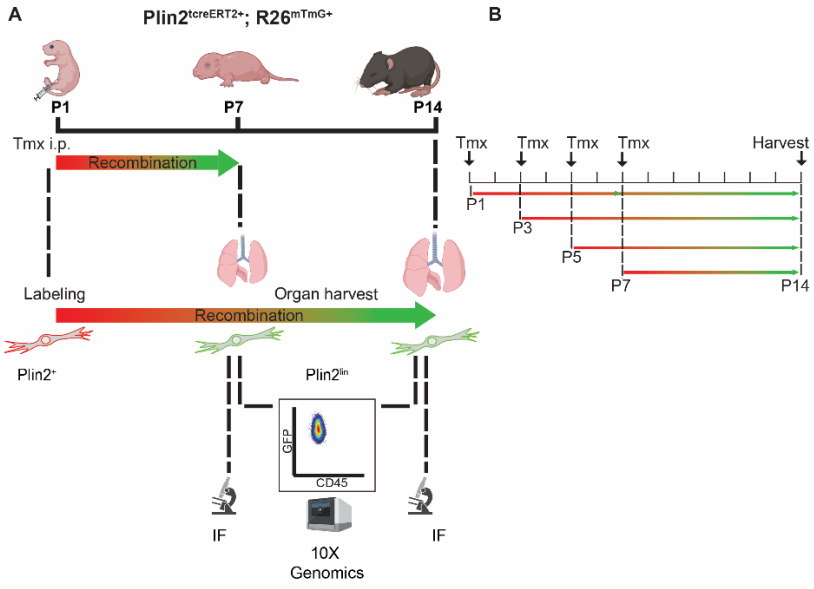

Figure 22. Experimental design for lineage tracing of Plin2 cells of the Plin2 cell lineage during alveolarization. (A) Plin2$^{creERT2+}$; R26^{mTmG+} inducible reporter mice received an i.p. Tmx injection at P1 to induce cre-induced recombination. All cells expressed tdTomato and upon cre recombination, cells of the Plin2 cell lineage expressed GFP. Lungs were harvested at P7 and P14 for scRNAseq by 10X Genomics sequencer and IF (B) Scheme illustrates labeling of Plin2^{+} cells at different time points to study Plin2^{lin} cells by IF and CLSM.

5.2.1 Characterization of lung cells of Plin2 cell lineage by scRNAseq at P7 and P14

To asses cellular contribution of $Plin2^{lin}$ cells to lung cell populations during late lung development, enriched $Plin2^{lin}$ cells were obtained from P7 and P14 lung homogenates by fluorescence-activated cell sorting (FACS). After exclusion of doublets and dead cells, hematopoietic-originated cells were also excluded using a common leukocyte marker known as CD45. Results showed that $Plin2^{lin}$ cells derived from a P7 lung were mainly positive for both the lineage label GFP (GFP^{+}) and the global tdTomato fluorescent reporter. However, $Plin2^{lin}$ cells derived from the P14 lung were either only GFP^{+} or GFP^{+}; $tdTomato^{+}$ (Figure. 23 A). Afterwards, $CD45^{-}GFP^{+}$ cells from single lung homogenates were followed by scRNAseq using the 10X Genomics Chromium platform. Following a general sequencing quality control (S1), data were preprocessed by StarSolo bioinformatics tool (S2). Thereafter, data were passed through essential steps like filtration, dimensional reduction and normalization. Identification of similar cells and classification into clusters which is the final step of post-processed data. To confirm that true $Plin2^{lin}$ cells were sequenced, expression of the reporter gene and lineage label GFP was probed. The outcomes proved that almost all 17886 sequenced cells did highly express GFP (Figure. 23 B). In total, 8791 and 9095 GFP^{+} cells were profiled from P7 and P14 $Plin^{creERT2+}$; $R26^{mTmG+}$ mouse lungs respectively. Cells were visualized in two dimensions according to their expression profiles by uniform manifold approximation and projection (UMAP) (Figure. 23 C). Seven cell clusters were well segregated. The distribution of these clusters indicated that cells derived from P7 and P14 lungs contributed diversely in different clusters. For instance, cells derived from P7 and P14 lungs contribute closely in cluster 1 and 4, while cluster five showed mainly contribution of P7-derived cells than P14 (Figure. 23 D). Moreover, it was noticed that cells from P7 were more abundant in clusters 2, 3, 6 and 7 (Figure. 23 D).

Unsupervised clustering from both time points identified seven distinct clusters (Figure. 24 A). The highest and lowest number of cells were found in cluster 1 and 7 (Figure. 24 B). To look at the appeared populations in details, a heatmap of normalized data was generated. The heatmap visualized top variant genes ordered by a median expression score per cluster (Figure. 23 C).

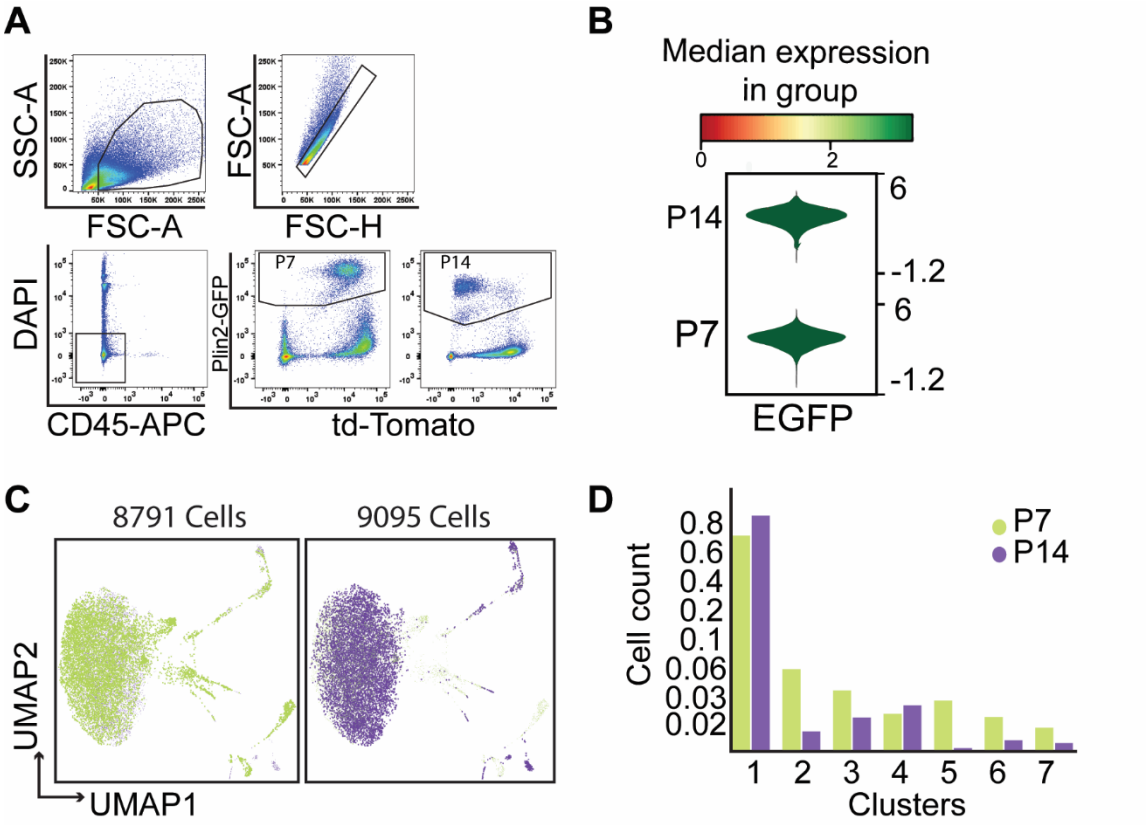

Figure 23. Single cell RNA sequencing of cells of the Plin2 cell lineage during alveolarization. (A) Flow cytometry plots of single cell suspensions from P1 labeled Plin2$^{creERT2+}$; R26^{mTmG+} at P7 and P14 mouse lungs were stained with an antibody against CD45. Plots demonstrate gating strategy for sorting CD45^{-} GFP^{+} (cells of the Plin2 cell lineage (Plin2^{lin})) cells. After exclusion of doublets and dead cells, GFP^{+}Plin2^{lin} cells were sorted for scRNAseq analysis. (B) Stacked violin plot shows high GFP expression in CD45^{-}GFP^{+} sequenced Plin2^{lin} cells. (C) UMAP graphs represent the clustering pattern of Plin2^{lin} sequenced cells from P7 (green) and P14 (Purple) mice. (D) Bar plot represents contribution of P7 and P14 derived Plin2^{lin} cells to distinguished clusters. FSC-A, forward scatter area; FSC-H, forward scatter height; SSC-A, side scatter area. DAPI, nuclear staining.

Except cluster 2, which did not show a clear pattern of expressed genes, other clusters followed an explicit expression pattern regarding different cell types in the lung (Figure. 24 C). Epithelial, endothelial, and different sub-population of mesenchymal fibroblasts cell expression schemes were identified (Figure. 24 C). Furthermore, a supervised cluster annotation was carried out. Therefore, Plin2^{lin} cells were identified based on their preferential and distinctive marker gene expression into known cell types of the lung. For instance, the canonical epithelial cell marker Epcam; further alveolar epithelial cell markers such as Sftpc and Pdpn; Pecam1 as a pan-endothelial marker; Hmgb2 as a mesenchymal progenitor cell marker; Acta2 as myofibroblast/smooth

muscle cell marker and finally Tcf21 as a marker for lipofibroblasts were chosen for annotation and classification (Fig. 24 D).

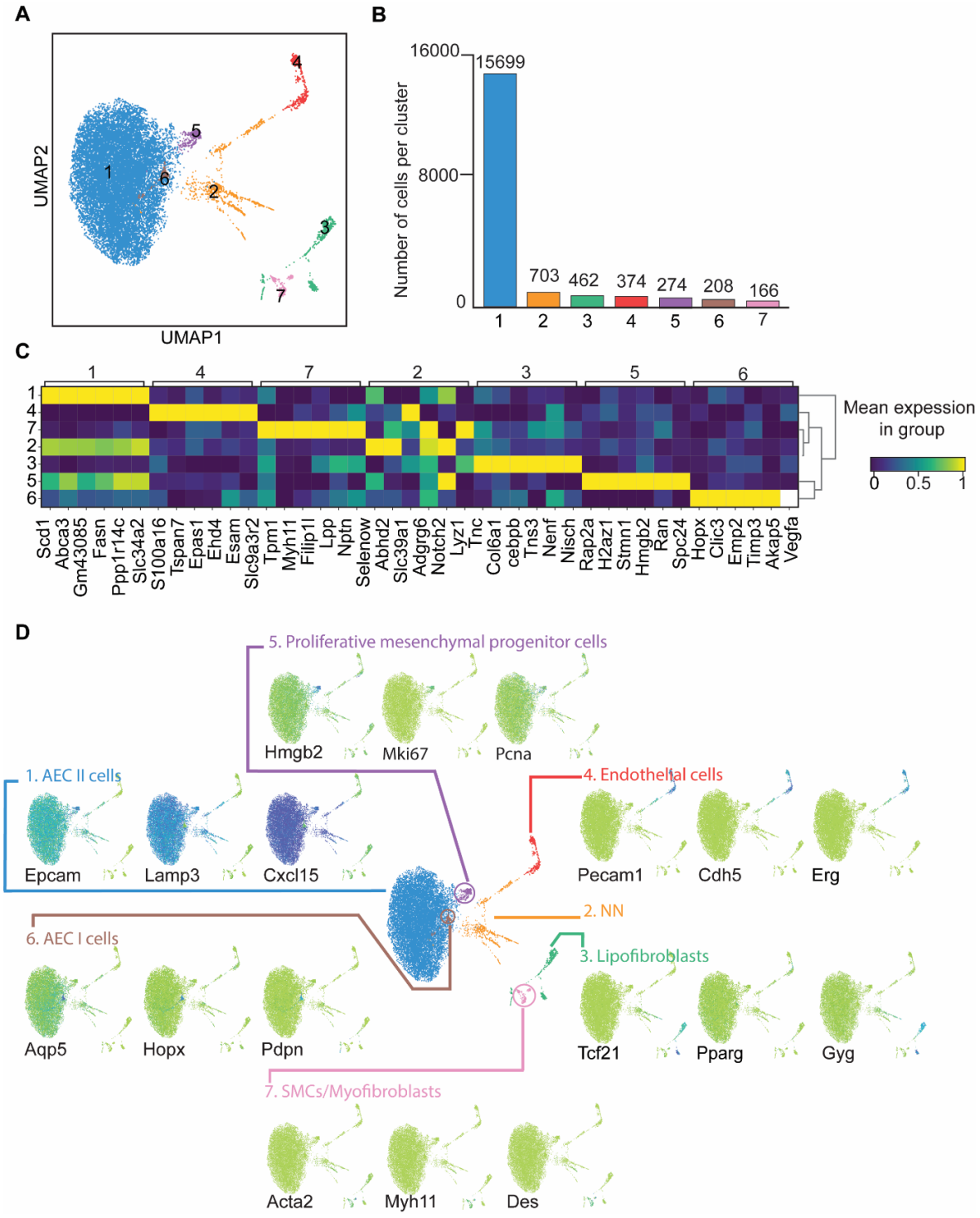

Figure 24. Classification of postnatal Plin2^{lin} cells by scRNAseq. (A) UMAP shows that the CD45^{-} Plin2^{lin} comprises seven distinct cell clusters. (B) Bar plot indicates number of cells in each cluster. (C) Heatmap visualization of top expressed genes per each cluster. (D) Manual annotation of gene expression patterns and classification of each cluster to a distinct cell type of the lung by known cell type specific markers. NN stands for not annotated because of a mixed transcriptomic profile.

Results showed conformity between both annotation approaches. Final cell annotation demonstrated that the Plin2^{lin} is composed of alveolar epithelial type II cells (AECs II), 87.77 %; NN, 3.9 %; lipofibroblasts (LIFs), 3.5 %; endothelial cells (ECs), 2.64 %; mesenchymal progenitor cells, 1.53 %; alveolar epithelial type I cells (AECs I), 1.16 %; and myofibroblasts/smooth muscle cells (MFs/SMCs), 0.93 % (Figure. 23 B). Together, these unbiased analyses indicated that diverse cell types could originate from cells expressing Plin2 at P1 (Plin2^{lin} from P1) during late lung development in mice.

5.2.2 Plin2^{lin} contribution to alveolar epithelial cell subpopulations

Exploring epithelial cell populations, Epcam expression was investigated across cell clusters. Clusters 3, 4, and 7 had very either low expression of Epcam or did not express it at all. It was demonstrated that in addition to AECs, other cell types such as mesenchymal progenitor cells remarkably expressed Epcam (Fig. 25 A). It was shown that in the Epcam^{+} population (Cluster 1), AEC II is the prevailing cell type whereas AEC I (Cluster 6) represents a small population (Figure. 25 B). In addition, AECs II had the highest expression levels of surfactant-associated protein family (Sftps) with a median expression of approximately 4.5, while the expression was comparatively lower in other cells, including AECs I with a median expression of around 2.5, as shown in (Figure. 25 C). To further specify epithelial sub-clusters, top 12 most significantly regulated genes (FDR<0.00001) in clusters 1 (AECs II) and 6 (AECs I) were plotted. Expectedly, these genes showed a complementary expression pattern between type I and II AECs, assuring valid classification and separation of Plin2^{lin}-derived epithelial cells (Figure. 25 D). These genes were highly expressed in the AECI and the AEC II cluster (Clusters 1 and 6), and were either absent or less expressed in other clusters, which was consistent with our tentative cell-type annotation (S 4).

Considering Plin2 as a classic LIF marker, deriving such a big alveolar epithelial cell population from cells, which were Plin2^{+} at P1, was unexpected. Hence, to evaluate the relevance of AEC II markers (here as an example only Sftpc family is considered) with Plin2 and with Tcf21 (Park et al., 2019) as casual LIF markers, dual genes analysis was performed. This analysis could present co-expression of different Sftp$_s$ with Plin2 or Tcf21 considering an expression cutoff equal to one. Again, it was shown that, Epcam was not expressed in the LIF cluster (Cluster 3) although Plin2 co-expression

with Epcam in the AEC II cluster was not negligible. Co-expression of Sftpa1, b and c with Plin2 was observed in both AEC II and the LIF cluster. However, Sftpd co-expression was barely detected in the LIF cluster (Figure. 25 E. Top panel).

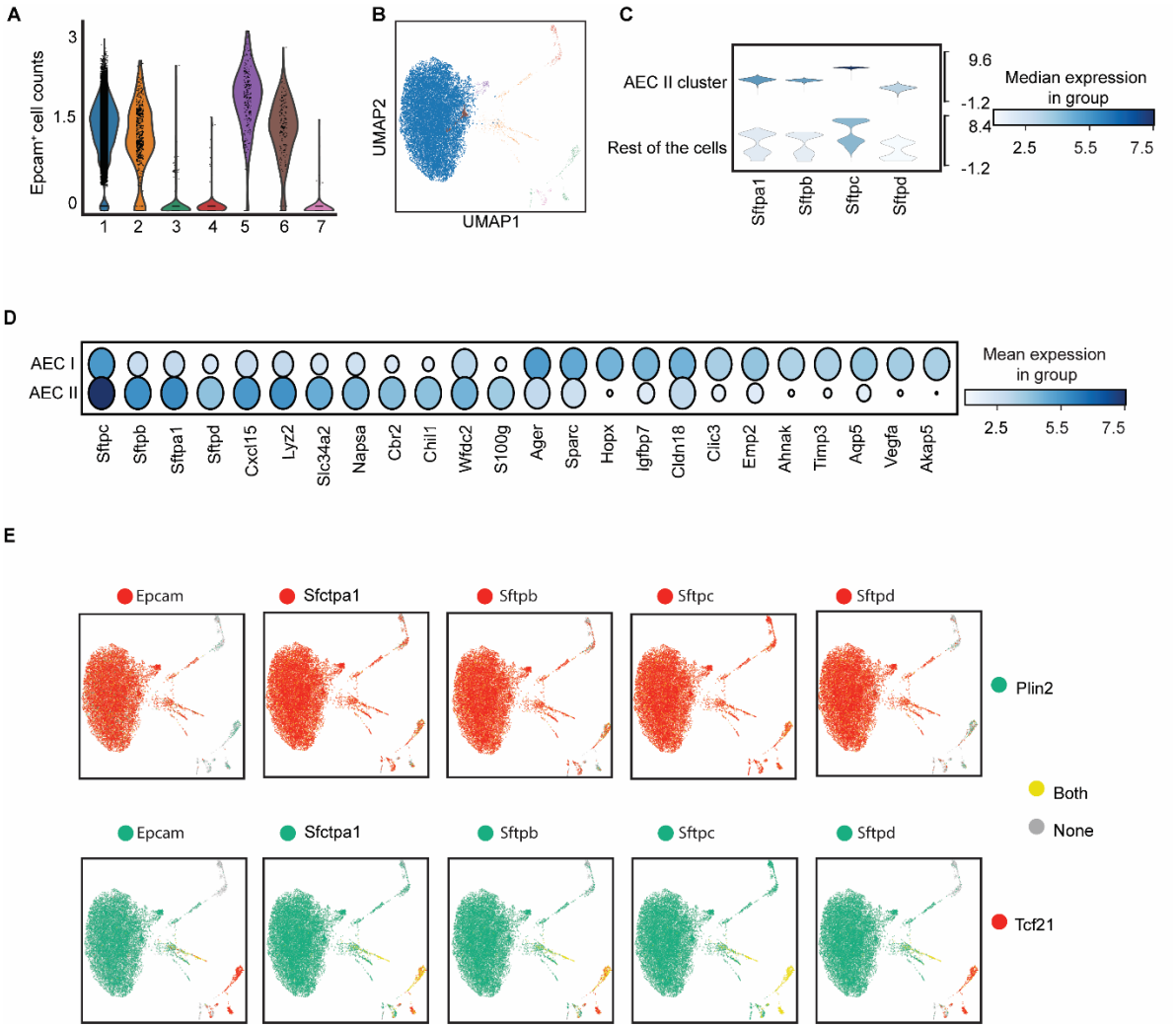

Figure 25. Contribution of the Plin2^{lin} to alveolar epithelial cell populations in the lung during alveolarization. Plin$^{creERT2+}$; R26^{mTmG+} mice were injected with Tmx at P1 and lungs were harvested at P14 for scRNAseq analysis. (A) Violin plot shows the expression of common epithelial cell marker Epcam in all clusters. (B) UMAP visualizes the AEC II cluster in blue as the prevailing clusters derived from the Plin2^{lin}. (C) High expression of surfactant-associated proteins is shown in the AEC II and the rest of the cluster by stacked violin plot. (D) Dot-plot represents top significantly regulated genes (q-value = 0) for identified epithelial cell types. The size of dots represents the relative gene expression in percentage of expressing cells for each cluster. The biggest size equals a value of 100 % that means that each cell within this cluster expressed this gene. Colors indicate the average expression level for indicated gene per cluster. (E) UMAPs plot the expression of Epcam and Sftp$_s$ with Plin2 or Tcf21. Top panel: red = epithelial markers, green = Plin2; Bottom panel: green = epithelial markers, red = Tcf21; yellow = co-expression and gray = no expression.

On the other hand, dual gene expression analysis demonstrated that LIF marker Tcf21 was not expressed in the AECs II and thus in general no co-expression of Epcam and $Sftp_s$ with Tcf21 in the AEC II cluster could be observed. Sftpa1, Sftpb and Sftpc were co-expressed with Tcf21 partially in the LIF cluster. There was no co-expression of Epcam with Tcf21 neither in the AEC II nor in the LIF clusters. In contrast, poor co-expression of Sftpd and Tcf21 was observed in the LIF cluster, since Epcam and Sftpd were hardly expressed in the LIF cluster (Figure. 25 A, E. Bottom panel).

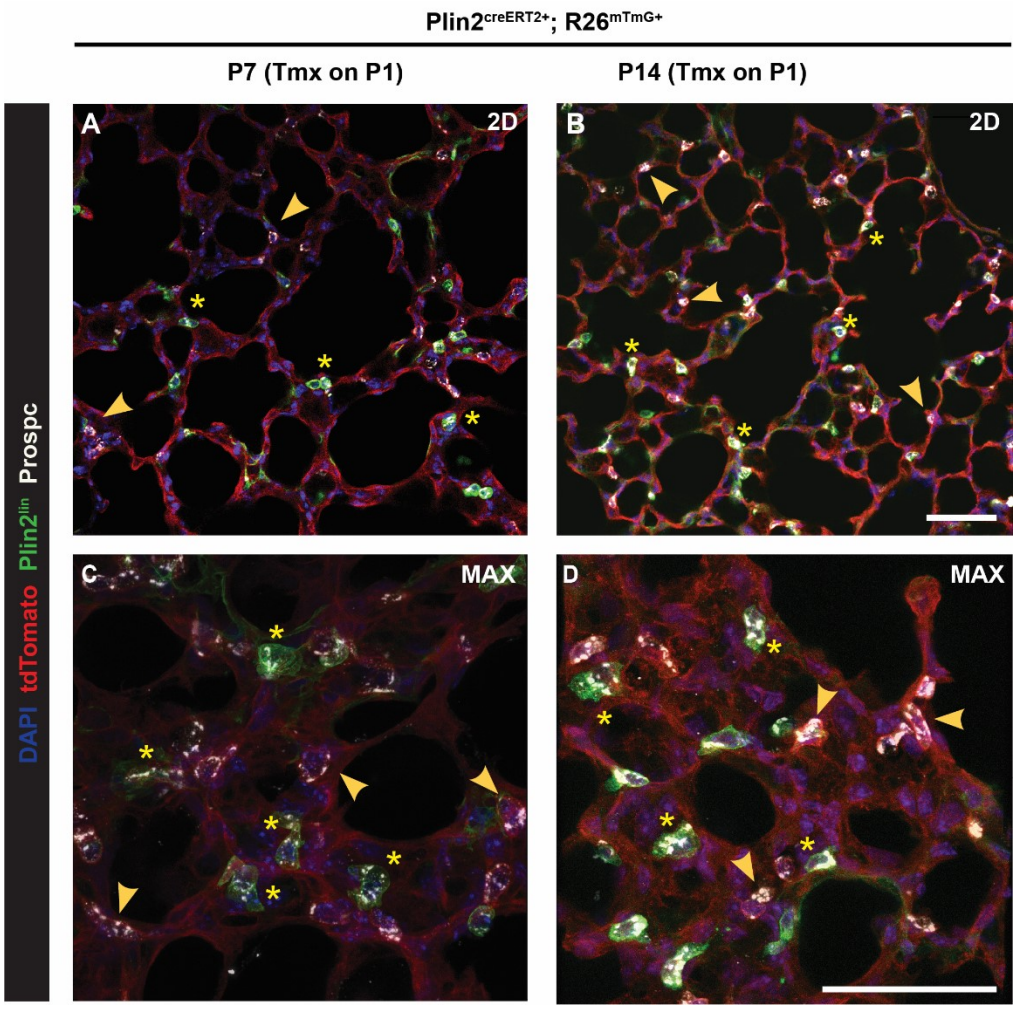

Figure 26. Confirmation of $Plin2^{lin}$ cell contribution to alveolar epithelial type II cells during alveolarization. Representative images of IF staining of PCLS from $Plinc^{reERT2+}$; $R26^{mTmG+}$ mice against Prospc, pro-surfactant protein C, as AEC II cell marker. Images were taken by CLSM to evaluate expression of Prospc protein by $Plin2^{lin}$ cells from $Plin2^{+}$ cells labeled at P1. (A, B) 2-dimensional representation of PCLS from P7 (A) and P14 $Plin^{creERT2+}$; $R26^{mTmG+}$ mice injected at P1(C, D) Maximal projection of PCLS from P7 (A) and P14 $Plin2^{creERT2+}$; $R26^{mTmG+}$ mice injected at P1. Terms 2D and MAX stand for two-dimensional and maximum intensity projection respectively. Asterisks (*) display $Plin2^{lin}$ cells expressing Prospc while arrowheads point to AECs II which are not $Plin2^{lin}$ traced. $Plin2^{lin}$ (green), tdTomato (red), Prospc (white) and nuclear stain DAPI (blue). Scale bar = 50 µm.

To validate these findings on protein level, same experimental design was followed by immunofluorescent (IF) histology and confocal laser scanning microscopy (CLSM).

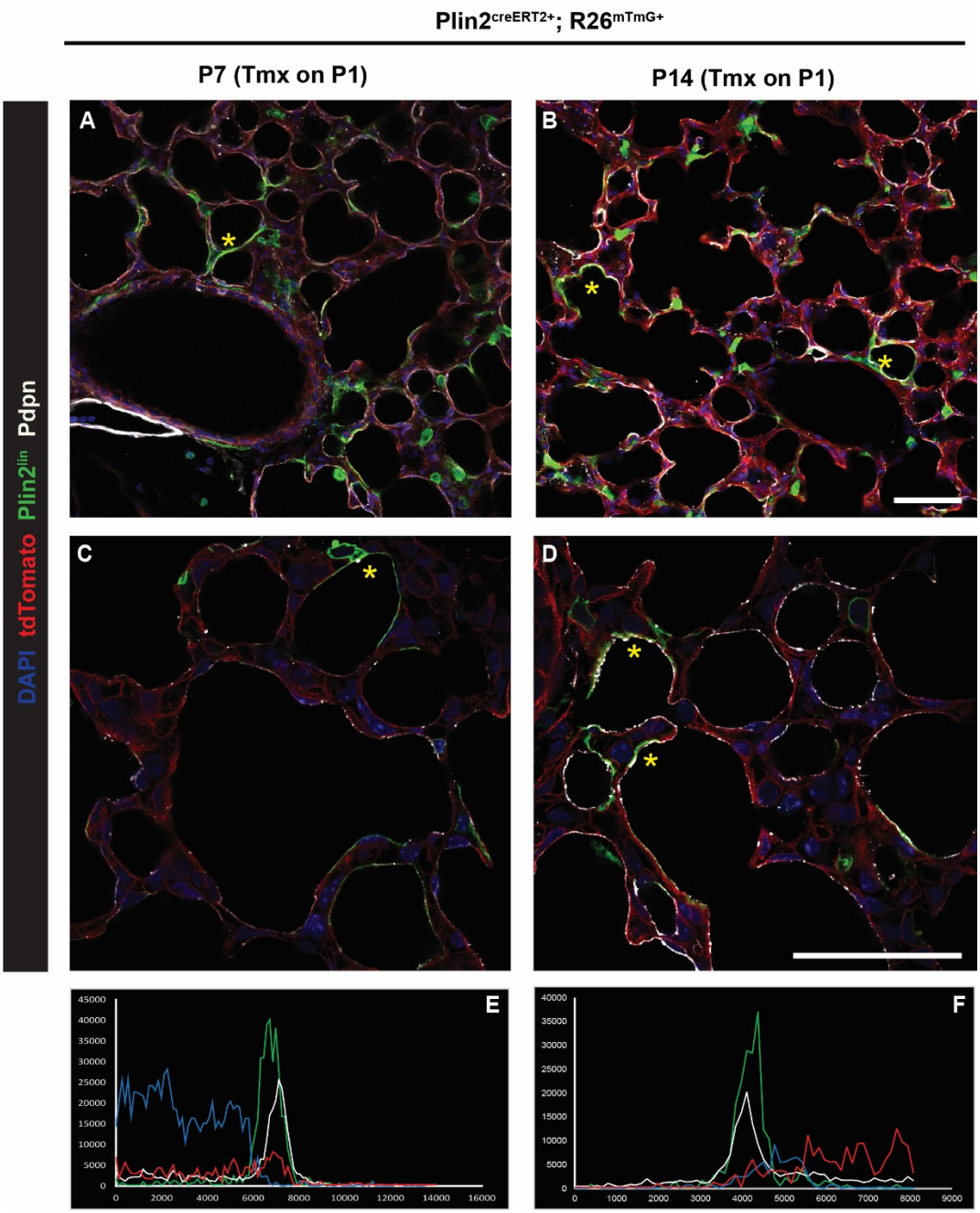

Figure 27. Confirmation of Plin2^{lin} cell contribution to alveolar epithelial type I cells during alveolarization. Representative images of IF staining of PCLS from Plin$^{creERT2+}$; R26^{mTmG+} mice against Pdpn, Podoplanin, as AEC I cell marker. Images were taken by CLSM to evaluate expression of Pdpn protein by Plin2^{lin} cells from Plin2^{+} cells labeled at P1. (A, B) Representation of PCLS from P7 (A) and P14 Plin$^{creERT2+}$; R26^{mTmG+} mice injected at P1 with 25X and (C, D) 60X magnification. (E, F) Representative fluorescent intensity overly analysis by ZEN program. Asterisks (*) display Plin2^{lin} cells expressing Pdpn. Plin2^{lin} (green), tdTomato (red), Prospc (white) and nuclear stain DAPI (blue). Scale bar = 50 µm.

Immunofluorescent staining against Pro-surfactant protein C (Sftpc) and Podoplanin (Pdpn) was performed on P7 and P14 precision-cut lung slices (PCLS). To distinguish Sftpc^{+} Plin2^{lin} cells, the association of Prospc to an individual cell was shown. In addition to 2-dimensional images (Figure. 26 A, B), 3D imaging was employed by means of maximum projection or 3D reconstructions (3D) of CLSM image analysis (Figure. 26 C, D). Results demonstrated that a large proportion of Plin2^{lin} cells was Sftpc^{+}. To confirm that Plin2^{lin} cells comprised AECs I, IF staining and CLSM imaging was performed on PCLS from Plin$^{creERT2+}$; R26^{mTmG+} mice stained against Pdpn (Figure. 27), Indeed some AECs I displayed the lineage label GFP at P7 and P14 (Figure. 27 A-D). AECs I are very thin cells. To prove the co-localization of Pdpn with GFP reporter of Plin2^{lin}, fluorescent intensity overly profiles of 2D CLSM images were used. This function of ZEN program could detect the fluorescents intensity overlaps of white (Pdpn) and green (Plin2^{lin} label) in 2D images (Figure. 27 E, F).

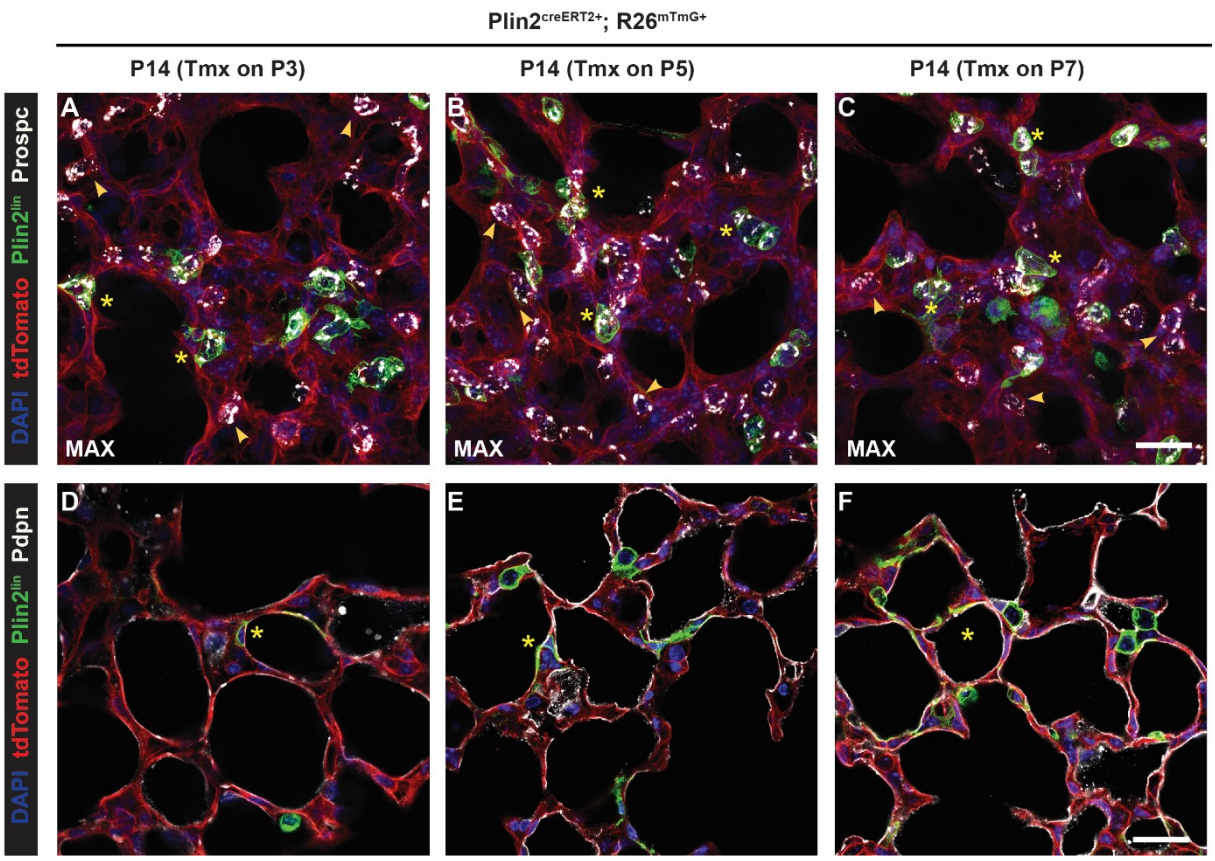

Figure 28. Expression of alveolar epithelial cell markers by Plin2^{lin} cells during the course of late lung development. Plin$^{creERT2+}$; R26^{mTmG+} mice were injected with Tmx at different time points (P3, P5 and P7) and lungs were harvested at P14. (A-C) Representative images of IF staining of PCLS against Prospc. MAX: Maximum projection illustrates spatial localization of Prospc within AEC II cells. (D-F) Common two-dimensional images show co-localization of Pdpn (white) and the lineage label GFP (green)

in Plin2^{lin} derived AEC I. Asterisks: Non-Plin2^{lin} derived AECs I displayed only white fluorescence. Plin2^{lin} (green), tdTomato (red), Prospc (white) and nuclear stain DAPI (blue). Scale bar = 20 µm.

These findings confirmed high contribution of Plin2-expressing cells from P1 to the AECs II population at the peak and end of bulk alveolarization at P7 and P14 respectively during late lung development. Furthermore, moderate contribution of the Plin2^{lin} to AECs I was confirmed.

To further explore how contribution of Plin2^{lin} cells to AECs might vary during the course of late lung development, Plin2-expressing cells were labeled at different time points. Plin2$^{creERT2+}$; R26^{mTmG+} neonates were injected with Tmx at P3, P5 and P7 lungs were harvested at P14 and stained for Prospc and Pdpn. IF staining against Prospc and Pdpn showed consistent pattern with results of P7and P14 mice which were injected at P1. All three different time points of injection demonstrated high contribution of Plin2^{lin} cells to AEC cells especially to AECs II (Figure. 28).

5.2.2.1 Molecular signatures of alveolar epithelial type II cells at P1

Deriving a big AECs II cluster from Plin2^{+} cells from P1, raised the question whether Plin2^{+} AECs II already existed at P1. To address this question, scRNAseq was applied on a wild type mouse (n = 1) at P1 with exactly the same experimental set up used for Plin2$^{creERT2+}$; R26^{mTmG+} transgenic mice. Thereby, CD45^{-} cells from the wild type P1 lung were sorted by FACS and were sequenced by10X genomics sequencer.

Afterwards, distinguished clusters were annotated manually using the same gene set used for generated data of Plin2^{lin} cells. Among 11 defined clusters, clusters 1 and 4 expressed respectively AEC II and AEC I markers, therefore were annotated to AECs I and AECs II respectively. Cluster 2 showed a mixed profile of AECs I and AECs II though more toward AECs II orientated in UMAP. To search for the LIF cluster, some of LIF-related genes were inspected and consequently cluster 5 was annotated as LIF cluster (Figure. 29 A). Next step was to check for co-expression of Plin2 and AEC II markers, to assess the existence of Plin2-expressing AEC II at P1. Even though, cells in the AEC II cluster did exclusively express AEC II markers, there were cells expressing both Plin2 and AEC II markers (Figure. 29 A). In contrast to P7 and P14 lungs from Plin2$^{creERT2+}$, R26^{mTmG+} mice, co-expression of epithelial markers except Sftpc with Plin2 in the LIF cluster was negligible (Figure. 29 B). Although dual genes

analysis could express the relationship of expression level of two genes in selected cells, it does not give more details about expression modality of those genes. To explore distribution density of Plin2 and Sftpc genes in both, the AEC II and the LIF cluster, density scatter plot was used, which allows to explore the joint expression density of Plin2 and Sftpc in cells expressing both gene. Each hexagon represents a number of cells with the same distribution density. In general, Plin2 expression density was lower than Sftpc gene expression density in both clusters. It could be observed that only a small population of cells showed a higher density of Plin2 and Sftpc co-expression around 1000-2000 (polygons in light green color) (Figure. 29 C).

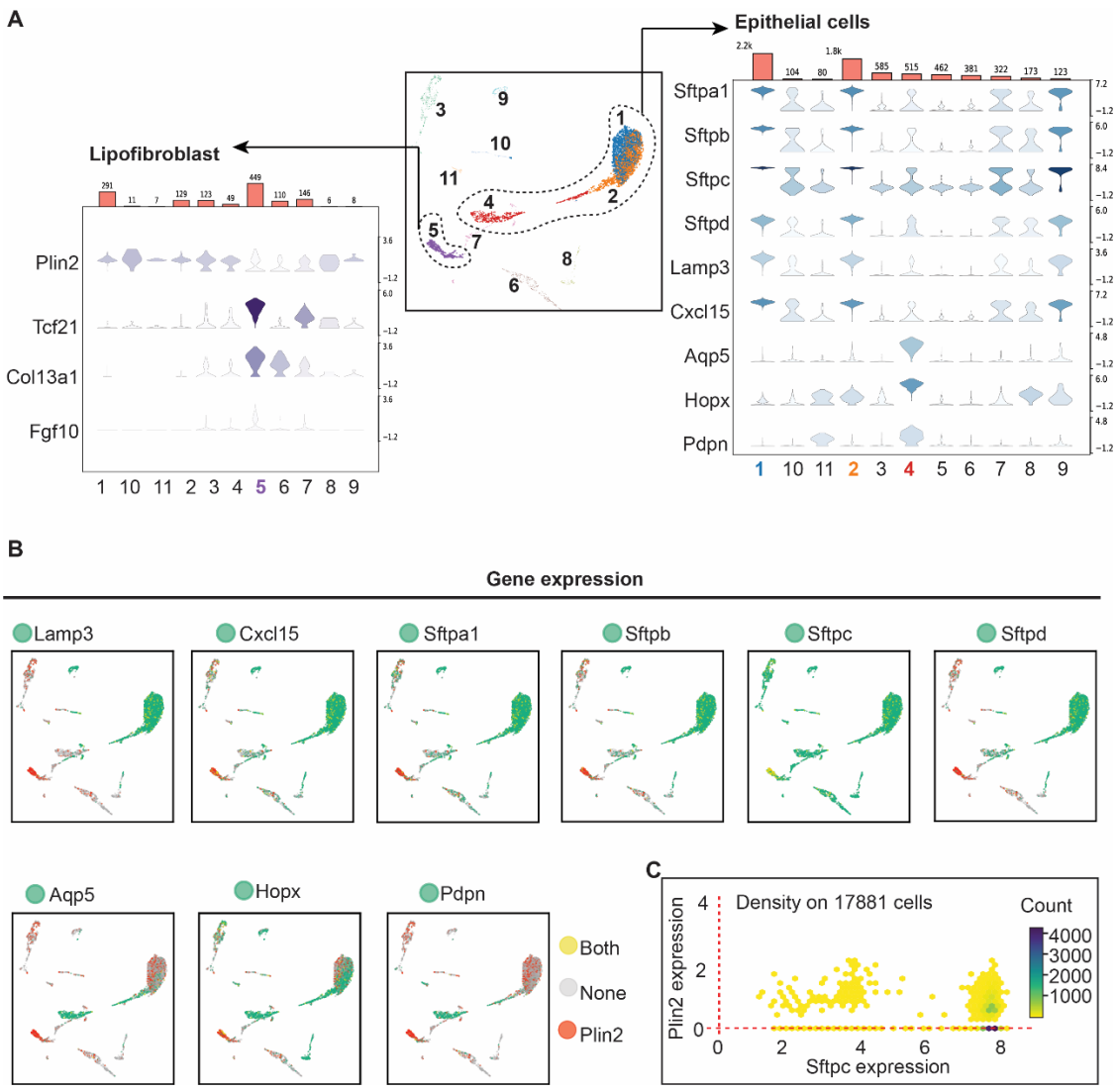

Figure 29. Existence of Plin2-expressing alveolar epithelial cells in a wild type lung at P1. ScRNAseq was performed on a wild type mouse lung at P1. (A) UMAP of CD45^{-} cells (6728 cells) depicted 11 segregated clusters. Clusters 1, 2 and 4 showed expression of epithelial cell markers via stacked violin plot on the right while cluster 5 expresses genes related to LIF populations, on the left.

(B) UMAP embedding of clusters where individual cells are colored by expression of only Plin2 (red), expression of only AECs markers (green), co-expression (yellow) of Plin2 with AECs markers. Gray color indicates expression of neither Plin2 nor AECs markers(C) Density scatter plot represents joint expression density of Plin2 and Sftpc in cells expressing both above an expression cut-off = 1. X-axis and Y-axis represent expression level of Sftpc and Plin2 genes respectively.

5.2.3 Validation of scRNAseq based gene expression in cell clones derived from the Plin2 lineage at the peak of alveolarization

To validate gene expression of Plin2^{lin} cells with higher biological replication, gene expression analysis was performed on CD45^{-} Plin2^{lin} cells (all CD45^{-}GFP^{+}) from Plin2$^{creERT2+}$; R26^{mTmG+} neonates injected with Tmx at P1 and sacrificed at P7 (n = 3). Results confirmed scRNAseq data. Plin2^{lin} cells expressed the lineage label GFP, mesenchymal cell markers (LIFs, myofibroblasts) as well as non-mesenchymal AEC II marker (Sftpc) (Figure. 30). Lineage label expression showed approximately the same expression level as mesenchymal cell markers. The highest expression level was seen in AECs II marker. Result indicate that the gene expression analysis for mentioned markers fits scRNAseq data in terms of both the prevalence of identified clusters and the expression levels of markers.

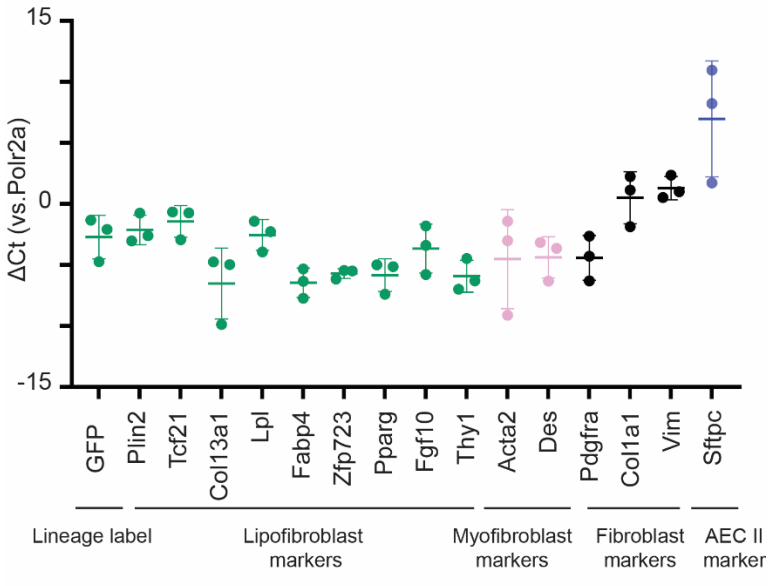

Figure 30. Gene expression analysis of Plin2^{lin} cells at the peak of alveolarization. Plin2$^{creERT2+}$; R26^{mTmG+} mice were injected with Tmx at P1 and lungs were harvested at P7 to sort Plin2^{lin} cells by FACS. All CD45^{-}Plin2^{lin} (CD45^{-}GFP^{+}) cells were sorted for gene expression analysis by qPCR. Polr2a was used as housekeeping gene. Data represent mean ± SD, no statistical comparison was made.

Additionally gene expression of Plin2 derived non-mesenchymal subpopulations was also confirmed by qPCR analysis. Endothelial ($CD31^+GFP^+$) and epithelial ($CD326^+GFP^+$) $Plin2^{lin}$ derived subpopulations were isolated using FACS (Figure. 31 A).

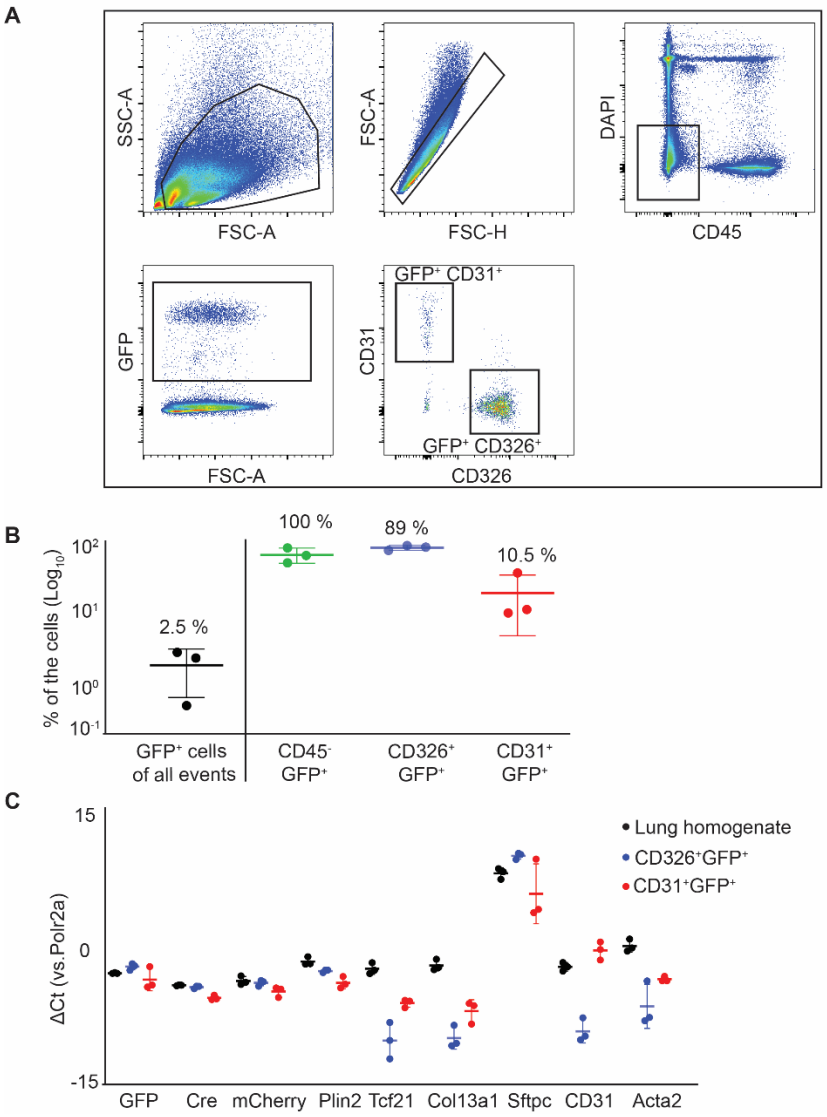

Figure 31. Gene expression analysis of non-mesenchymal $Plin2^{lin}$ derived endothelial and epithelial populations during alveolarization. $Plin2^{creERT2+}$; $R26^{mTmG+}$ mice were injected with Tmx at P1, lungs were harvested at P14 $Plin2^{lin}$ epithelial and endothelial cells were sorted by FACS. (A) Cell suspensions were fluorescently stained with anti-CD45 (hematopoietic cells marker), anti-CD326 (epithelial marker) and anti-CD31 (endothelial marker). Gating strategy was defined based on single stained and FMO controls. GFP^+ epithelial cells and GFP^+ endothelial cells were sorted for qPCR analysis. (B) Plot represents the percentage of the different cell populations in P14 lungs. (C) Levels of mesenchymal and non-mesenchymal marker genes were assessed in the $CD31^+GFP^+$; $CD326^+GFP^+$ cell populations and entire lung homogenate by qPCR. Polr2a was used as housekeeping gene. Data represent mean ± SD, no statistical comparison was made.

Averagely, 2.5 % of all cells were GFP^+ from which ~ 64 % were negative for the hematopoietic marker CD45. Flow cytometry results also indicated that epithelial and endothelial cells formed respectively ~ 89 % and ~10.5 % of the $CD45^-GFP^+$ population (Figure. 31 B). Marker genes for both mesenchymal and non-mesenchymal cells were evaluated in sorted populations. Baseline expression levels were determined by analyzing lung homogenates. Gene expression analysis of sorted populations revealed generally low expression levels of mesenchymal LIF markers. The expression levels of lineage label markers were consistent with the expression of LIF markers. Sftpc expression showed highest expression level exclusively in its relevant population (GFP^+CD326^+), while CD31 expression level was also highest exclusively in its relevant population (GFP^+CD31^+) (Figure. 30 C).

These observations indicated that different strategies for gene expression analysis confirmed generated scRNAseq data of $Plin2^{lin}$ cell, AEC II constituted the major cell type derived from $Plin2^{lin}$ cells during alveolarization.

5.2.4 Single-cell transcriptomic profile of $Plin2^{lin}$ derived endothelial cells

To inspect endothelial cell populations derived from $Plin2^{lin}$ cells, pan endothelial cell (EC) markers were included in the analysis. Cluster 4 demonstrated a high cell count expressing the common EC marker gene, Pecam1 (CD31) (Figure. 31 A). Expression of other canonical endothelial markers, e.g. Cadherin 5 (Cdh5); Claudin 5 (Cldn5); BMX non-receptor tyrosine kinase (Bmx) and ETS transcription factor (Erg) were also examined on UMAP projection of all clusters. To confirm ECs derived from the $Plin2^{lin}$, other known endothelial markers were also taken into consideration within cluster 4. Different endothelial transcriptional factors e.g. Sox7, Sox18, Erg, Tie1, Gata2; some vasodilator receptors e.g. Calrl and Ramp2; other endothelial receptors e.g. Flt1, Adgrl1, Bmpr2, Acvrl, and some endothelial cell adhesion molecules e.g. Esam, Clec14a were significantly (FDR≤0.00001) expressed in cluster 4 and no remarkable expression was observed in the other clusters (Figure. 32 B).

By higher resolution, bigger clusters split into their optimal well-connected sub-sets $Plin2^{lin}$ traced ECs with high CD31 expression appeared to consist of two distinguishable sub-clusters. Aiming to decipher these endothelial subpopulations, data were reanalyzed with higher resolution. (Figure. 32 C). EC clusters 6 and 8 were

derived from the initial EC cluster 4. However, cluster 7 expressed CD31 to a lesser extent.

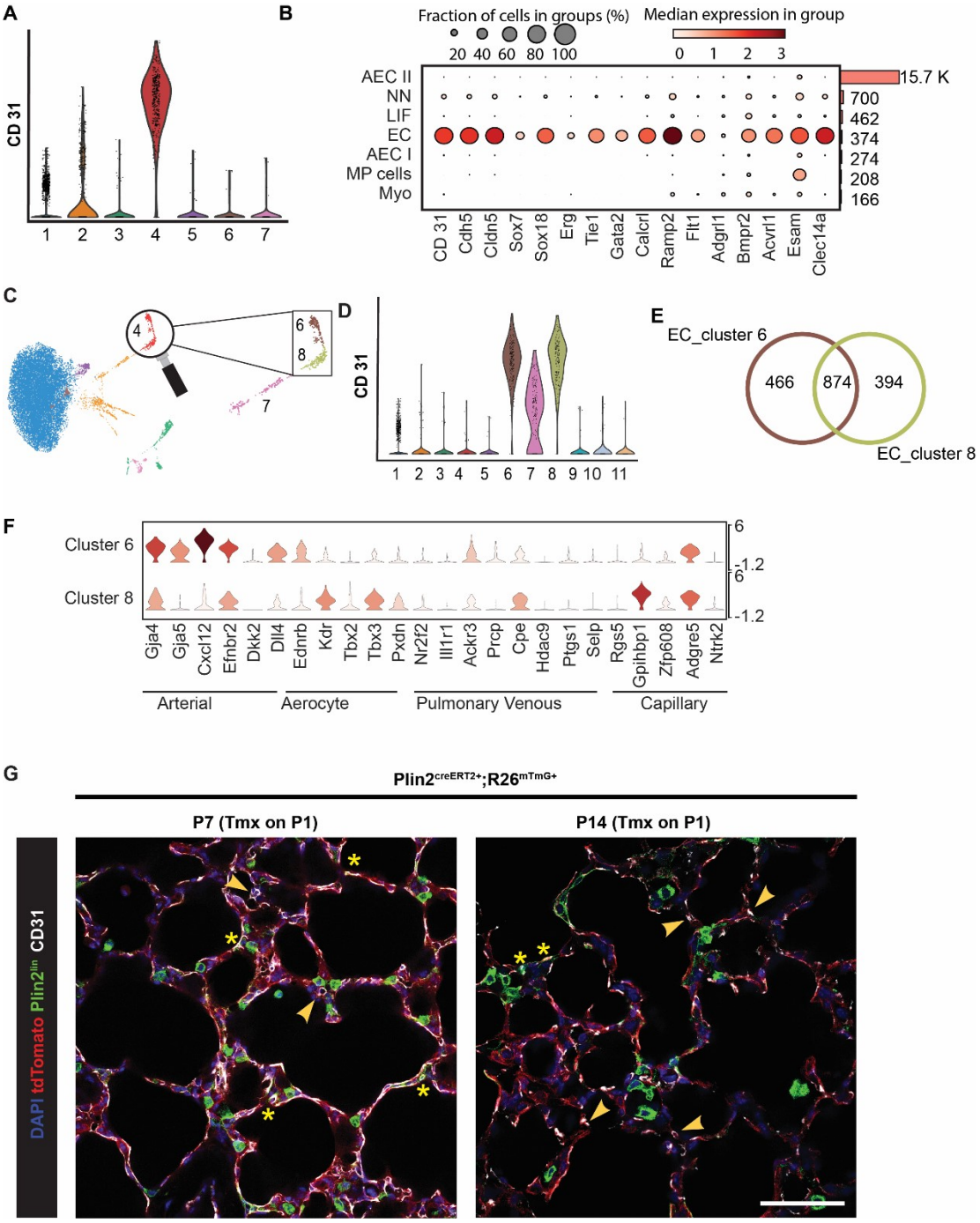

Figure 32. Plin2^{lin} comprises endothelial cell populations during alveolarization. Plin$^{creERT2+}$; R26^{mTmG+} mice were injected with Tmx at P1 and lungs were harvested at P14 for scRNAseq analysis. (A) Violin plot demonstrates expression of CD31, a pan endothelial marker in all clusters. (B) Dot plot visualizes EC marker genes (which are conserved in EC populations in humans and mice) within different clusters. (C) EC sub-clusters were distinguished by higher resolution analysis. (D) Violin plot indicates CD31 expression in 11 clusters derived from the analysis with higher resolution. (E) Venn diagram

represents number of common and unique expressed genes in Plin2^{lin} derived endothelial cell subpopulations. (F) Expression of marker genes for EC subtypes are shown in defined EC sub clusters 6 and 8 by stacked violin plot. (G) Representative images of IF staining against CD31 in P7 and P14 PCLS from P1 labeled Plin$^{creERT2+}$; R26^{mTmG+} mice. Asterisks indicate Plin2^{lin} derived ECs while arrowheads show ECs from different origin. Plin2^{lin} (green), tdTomato (red), CD31 (white) and nuclear stain DAPI (blue). Scale bar: 100µm.

This cluster was derived from the initial cluster 2, which exhibited a mixed profile of different cell types. Hence, it was excluded from further analysis (Figure. 32 D). Selected genes that showed a fold change > 1.5 and significant different expression between the two subsets were compared between two sub-sets (FDR ≤ 0.0001). It was observed, that the two subsets shared a high number of genes (874 genes), while there was also a notable number of genes, which were exclusively expressed in either of the sub-sets (Figure. 32 E). To further characterize molecular signatures of EC derived from the Plin2^{lin}, expression of marker genes of different types of EC was surveyed. Marker genes conserved in both, human and mice were preferred to use to distinguish between lung EC populations. Arterial and venous EC, aerocytes and capillary EC markers were screened. Outcomes revealed that Plin2^{lin} traced ECs displayed a high detection rate of arterial EC markers in cluster 6. The lowest detection rate was related to pulmonary venous EC markers (Figure. 32 F). To validate that ECs were derived from the Plin2^{lin}, CD31 IF staining was carried out on P7 and P14 PCLS from Plin$^{creERT2+}$; R26^{mTmG+} mice. Plin2^{lin} cells positive for CD31 were detected in both P7 and P14 mouse lungs in the alveolar region (Figure. 32 G).

These analyses declared that cells expressing Plin2 at P1 contribute to different types of ECs in the course of late lung development.

5.2.5 Identification of a Plin2^{lin} derived myofibroblast population

Exploring Vimentin (Vim), an intermediate filament protein known as a mesenchymal fibroblast marker, Vim was highly expressed in three clusters, the EC, the myo- and the lipo-fibroblast cluster (Figure. 33 A). Thereafter, known mesenchymal myofibroblasts (MF) markers like Actin alpha 2 (Acta2) and Desmin (Des) were exploited and only cluster 7 could be distinguished as MF cluster (Figure. 33 B, C). Nevertheless, co-expression of Acta2 with other insofar known myofibroblasts markers including Elastin (Eln), Fibronectin 1 (Fn1), Transgelin (Tagln), and Tenascin C (Tnc)

were also examined. Results demonstrated that among Vim^+ cells, Acta2-expressing cells co-expressed highly Des, Eln, Tagln and Fn1 in cluster 7 (Figure. 33 D). Expression of Pdgfrα and Tnc showed lower occurrence in $Acta2^+$ cells (Figure. 32 D). Additionally, to characterize the genetic profile of $Plin2^{lin}$ derived mesenchymal fibroblast subpopulations, differentially expressed genes were investigated between clusters 3 (LIFs) and 7 (MFs). Among 2038 significantly differentially expressed genes, 1165 genes showed higher expression in the LIF cluster, while 873 genes showed higher expression in the MF cluster. Genes such as Crip1 & 2, Cald1, Tagln and Mustn1, which are involved in collagen production, metabolic and regulatory pathways, were up regulated in the MF cluster. Genes like Npnt, Ptprd, Col13a1, Adh1, Slc36a2 and Slc38a5 were strongly expressed by the LIF cell population (Figure. 33 E). Comparison of these mesenchymal sub-clusters revealed many significantly up-regulated genes in each cluster. Therefore, a selection was made to focus on genes encoding for membrane proteins, since membrane proteins represent suitable target genes to target a specific cell type.

Membrane located genes were searched using a threshold of FDR ≤ 0.00001 and FC ≥ 4 in up regulated genes. Top 30 most significantly regulated genes were selected (Figure. 33 F, G). The Differential gene expression analysis showed that there were genes coding for membrane or transmembrane proteins among up-regulated genes in both lipo- and myo- fibroblasts, (Figure. 33 F, G).

IF staining was performed for α-smooth muscle actin (α-SMA) (Gene name: Acta2) on P7 and P14 PCLS from $Plin2^{creERT2+}$; $R26^{mTmG+}$ P7 and P14 mice injected with Tmx at P1. As expected, CLSM analysis demonstrated that some $Plin2^{lin}$ traced cells were positive for α-SMA (Figure. 34 Dash-boxes). Interestingly, there were also some α-SMA-expressing cells on the tips of the alveolar septa, which were not derived from P1 labeled Plin2-expressing cells (Figure. 34 Arrowheads).

These data suggested that alveolar myofibroblasts have different origins during late lung development and that one subpopulation aroused from the $Plin2^{lin}$. Moreover, a combination of known and here mentioned markers could help to better characterization of mesenchymal subpopulations in the lung.

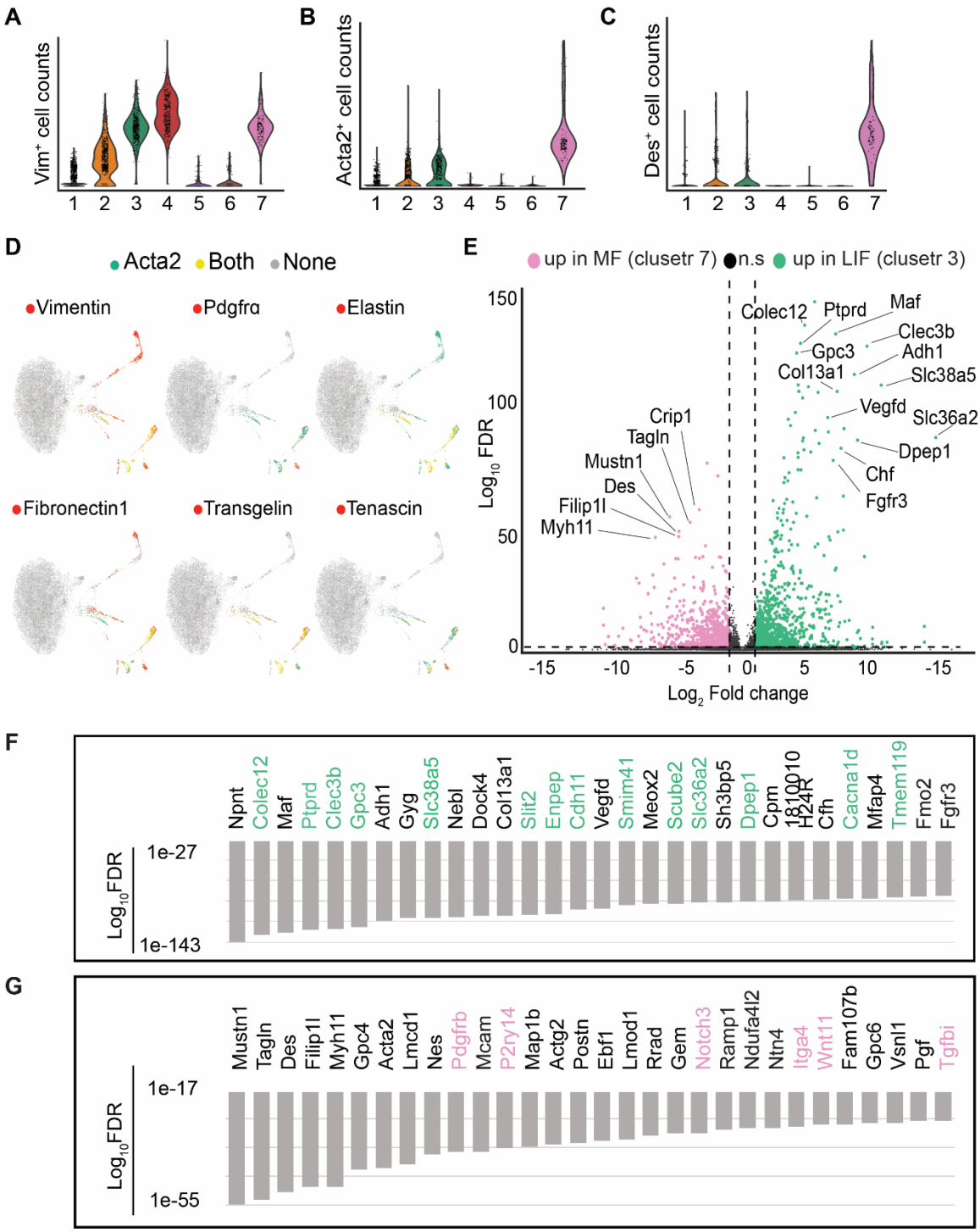

Figure 33. Plin2^{lin} contributed to a myofibroblast population during alveolarization. Plin$^{creERT2+}$; R26^{mTmG+} mice were injected with Tmx at P1 and lungs were harvested at P14 for scRNAseq analysis. Violin plots show expression of (A) Vim (B) Acta2 and (C) Des in all clusters. (D) UMAP embedding of clusters where individual cells are colored by expression (Red), no expression (gray) and co-expression of Acta2 with known myofibroblasts markers (yellow). Green dots represent expression of Acta2. (E) Significant DEGs in mesenchymal Lipo- vs Myo-fibroblast subpopulations are shown by volcano plot. (F) DEGs in LIF population and (G) DEGs in MF population. Green and pink state (trans) membrane located genes.

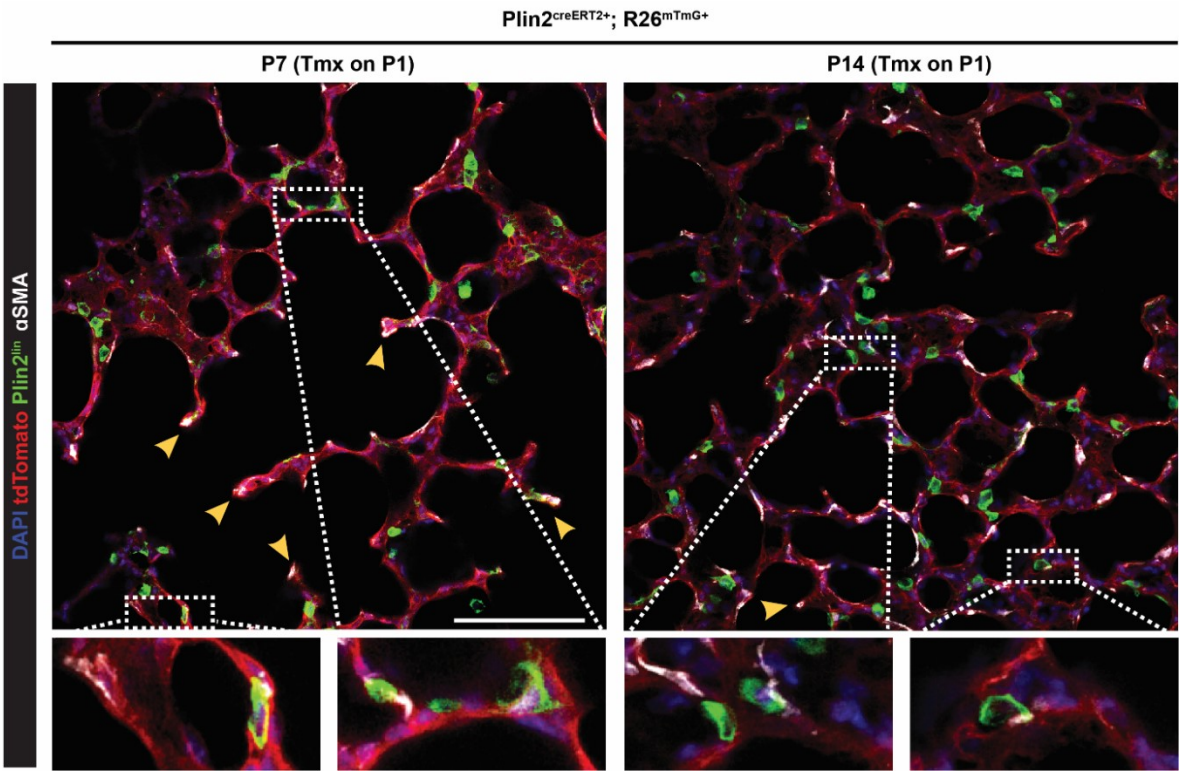

Figure 34. Localization of Plin2^{lin} derived myofibroblasts in the postnatal lung. Representative image of IF staining of P7 and P14 PCLS from Plin$^{creERT2+}$; R26^{mTmG+} P7 and P14 mice injected with Tmx at P1 and stained with smooth muscle actin (αSMA) antibody, αSMA^{+} cells demonstrate myofibroblasts in the lung. Dash boxes represent Plin2^{lin} derived myofibroblasts at the base of secondary septa at P7 and within alveolar septa at P14. Arrowheads display non-Plin2^{lin} derived αSMA^{+} cells at the tip of secondary septa at P7 and within alveolar septa at P14. Plin2^{lin} (green), tdTomato (red), αSMA (white) and nuclear stain DAPI (blue). Scale bar: 100µm.

5.2.6 Molecular signature of Plin2^{lin} derived lipofibroblast

Lipofibroblasts are internal fibroblasts, which contain neutral lipid droplets. It was shown that LIFs, as well as MFs, could differentiate from platelet-derived growth factor receptor alpha (Pdgfrα) expressing precursor cells. Therefore, expression of Plin2, Tcf21 and Pdgfrα was searched in the dataset. Results depicted that Plin2^{lin} derived LIFs expressed Pdgfrα as well as Plin2^{lin} derived MFs at very low level (Figure. 35 A). Hitherto, Plin2 and Tcf21 have been used as mesenchymal LIF related markers. Therefore, to analyze their expression relationship, dual gene expression analysis was exploited. Overlap expression of Plin2 and Tcf21 was observed mainly in cluster 3 (Figure. 35 B).

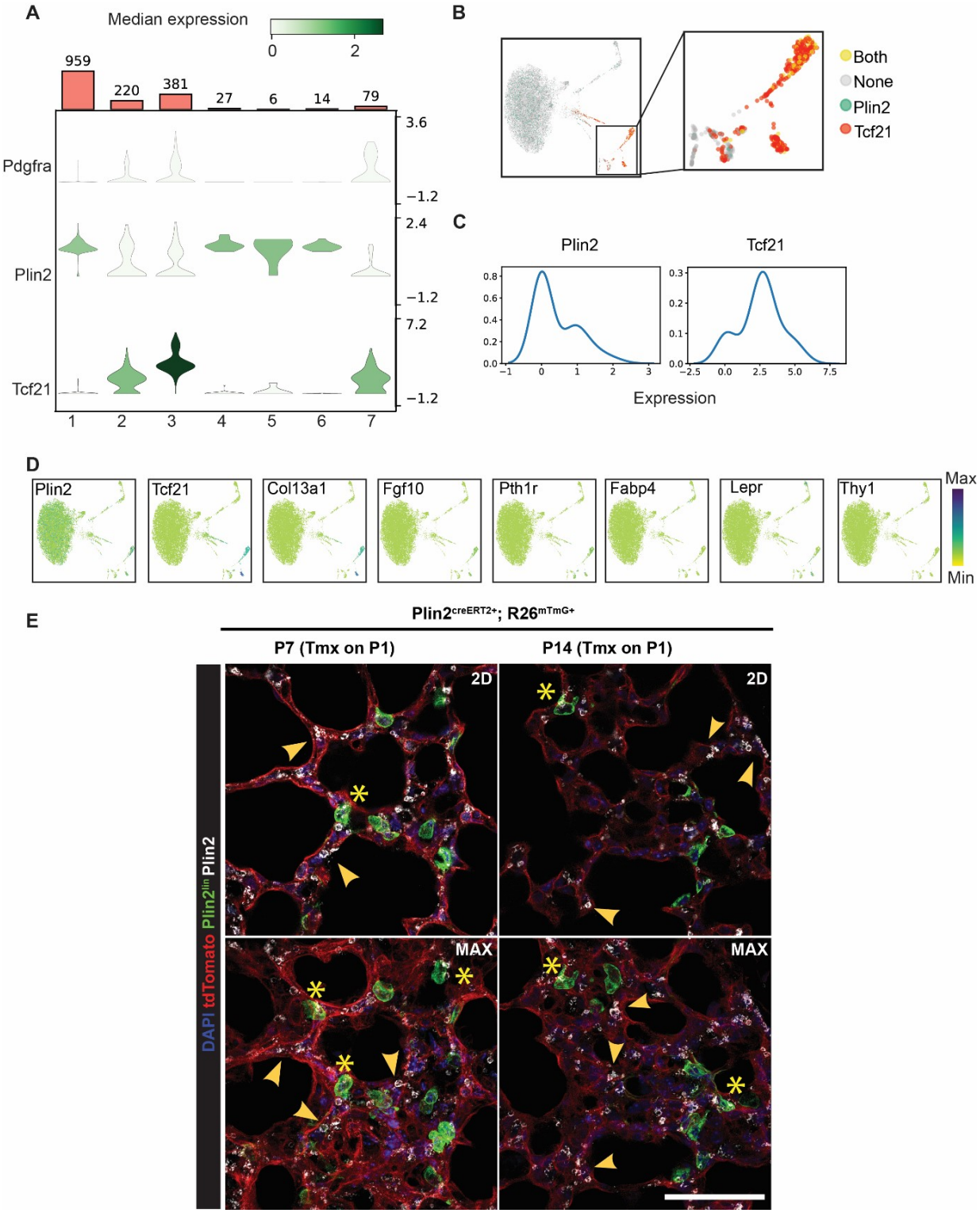

Figure 35. Molecular signatures and cellular localization of Plin2^{lin} derived lipofibroblasts during alveolarization. Data were generated by scRNAseq of Plin2^{lin} cells labeled at P1 and harvested at P7 and P14 from Plin2^{creERT2}; R26^{mTmG} mice. (A) Stacked violin plot displays expression of Pdgfrα, Plin2 and Tcf21. (B) UMAP indicates Plin2 expression (green), Tcf21 expression (red), Plin2 and Tcf21 co-expression (yellow) and expression of none of them (gray) (C) Density plot of Plin2 and Tcf21 in all cells. (D) LIF related genes were visualized by UMAPs in defined cell types. (E) Representative images of IF

staining of P7 and P14 PCLS from Plin$^{creERT2+}$; R26^{mTmG+} P7 and P14 mice injected with Tmx at P1 and stained with Plin2 antibody. 2D images and MAX of the same fields from P7 and P14 lungs demonstrated actual expression of Plin2 as white globe-shaped structures. Asterisks show Plin2 expression by Plin2^{lin} cells. Arrowheads point at Plin2 expression in non-Plin2^{lin} derived cells. Plin2^{lin} (green), tdTomato (red), Plin2 (white) and nuclear stain DAPI (blue). Scale bar = 50µ.

To review expression patterns of Plin2 and Tcf21, their density plots were drawn in cluster 3. Density plot is a smoothed version of the histogram. Density plot showed the density of cells expressing Tcf21 with an expression level of around 2.5; whereas this value for Plin2 was much lower (Figure. 35 C). To investigate the genetic signature of Plin2^{lin} derived LIFs, other insofar-acknowledged LIF markers were checked by UMAP projection. It was seen that Col13a1, Fgf10, Pth1r, and Lepr genes had a higher detection rate than Pparg, Fabp4, and Thy1 in annotated LIF populations. Interestingly, UMAPS depicted that all cells in cluster 3 were expressing Tcf21 and not Plin2 (Figure. 35 D). To validate Plin2 expression, IF staining was used and PCLS from Plin$^{creERT2+}$; R26^{mTmG+} P7 and P14 mice injected with Tmx at P1 were stained with Plin2 antibody. Plin2 is in fact amphiphilic protein that coats the neutral lipids in cells. Therefore, IF staining against Plin2 appears as tiny vesicles histologically. A portion of Plin2^{+} cells were negative for the Plin2^{lin} label GFP, others expressed the lineage label GFP at P7 and P14 (Figure. 35 E). In mice, Plin2 expression starts from embryonic day (E) 14.5 and continues up to adulthood. To analyze how Plin2 expression might alter within the Plin2^{lin} during alveolarization, Plin2-expressing cells were labeled at different time points. Plin$^{creERT2+}$; R26^{mTmG+} neonates were injected with Tmx at P3, P5 and P7 and lungs were harvested at P14. Immunofluorescent staining against Plin2 revealed similar outcomes as the data obtained from P1 labeled mice (Figure. 36). At a lower magnification (25X objective lens), Plin2 expression exhibited a widespread pattern throughout the lung (Figure. 36 A-C). At a higher resolution (60X objective lens), co-localization of Plin2 and Plin2^{lin} label GFP was better displayed (Figure. 36 D-F). Results showed that Plin2 expression was less abundant during the course of late lung development in Plin2^{lin} cells. (Figure. 36).

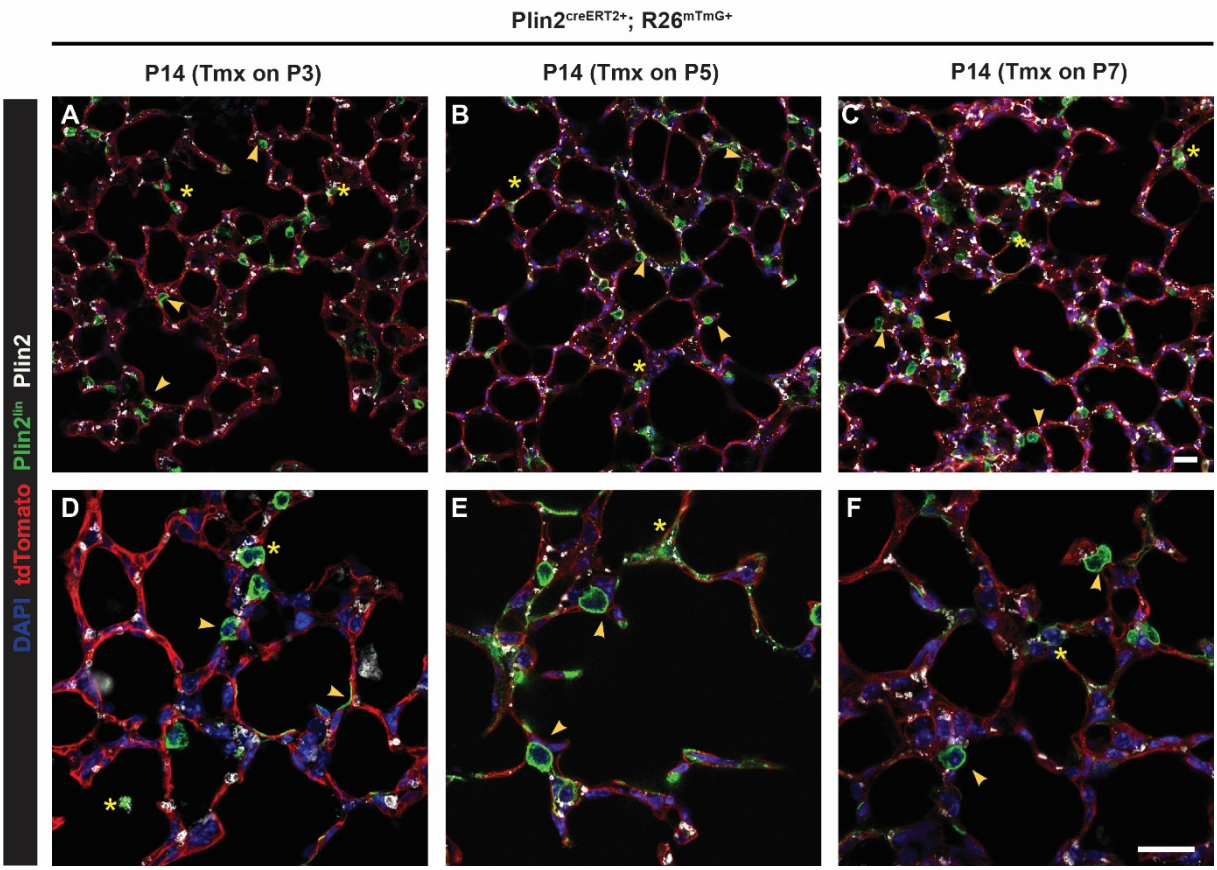

Figure 36. Plin2 expression in Plin2^{lin} cells during the course of late lung development. Representative images of IF staining of P7 and P14 PCLS from Plin$^{creERT2+}$; R26^{mTmG+} P7 and P14 mice injected with Tmx at P1 and stained with Plin2 antibody. (A-C) CLSM images with 25X objective lens. (D-F) CLSM images with 60X objective lens. Asterisks indicate Plin2 expression by Plin2^{lin} cells. Arrowheads indicate Plin2^{lin} cells, which are Plin2^{-}. Plin2^{lin} (green), tdTomato (red), Plin2 (white) and nuclear stain DAPI (blue). Scale bar = 20 µm.

Interestingly, it was observed that Tcf21 was highly expressed in a small discernible group of cells belonging to cluster 3 (Tcf21^{high}). However, its expression rate was low in the rest of cells of clusters, cluster 3 (Tcf21^{low}) (Figure. 37 A). In order to understand transcriptomic profiles of Tcf21^{high} and Tcf21^{low} cell populations, data was reanalyzed with higher resolution.

Reanalysis declared that the LIF cluster was composed of two different subsets. It was speculated that the difference between these subtypes could help to discover new potential markers for pulmonary LIFs. By higher resolution, the LIF cluster was split into two discernible smaller cluster 3 and cluster 11, respectively Tcf21^{low} and Tcf21^{high} (Figure. 36 A). Additionally, a volcano plot of Tcf21^{high} versus Tcf21^{low} was generated

to compare DEGs in both sub-clusters. Despite many common genes, there were 917 and 311 genes significantly upregulated in Tcf21^{low} versus Tcf21^{high} subtypes respectively.

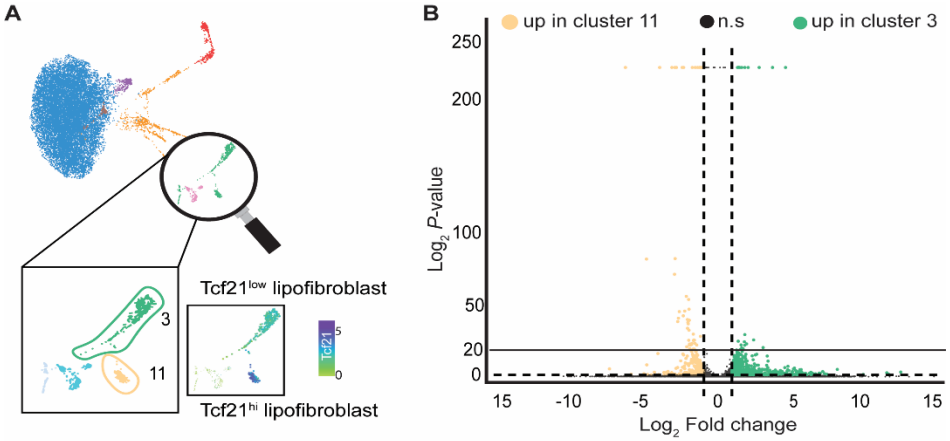

C

Gene name	Fold change	qvalue
Eln	-3.05	9.80E-90
Mfap4	-5.10	2.11E-89
Fhl1	-3.10	6.33E-78
Mgp	-2.25	2.57E-61
Gsn	-2.09	6.36E-59
Npnt	-2.06	1.35E-51
Col1a2	-2.37	3.20E-50
Fn1	-2.76	8.58E-50
Col1a1	-2.47	1.27E-46
Tcf21	-2.82	7.89E-45
Plxdc2	-2.17	8.61E-44
Pcolce2	-2.04	3.08E-43
Inmt	-2.87	2.78E-42
Bgn	-2.14	1.27E-41
Gpx3	-2.12	1.28E-40
Col3a1	-2.17	3.14E-37
Mxra8	-2.06	8.60E-36
Macf1	-1.75	8.34E-33
Limch1	-1.25	3.79E-31
Apoe	-1.72	2.23E-28
Serping1	-1.68	2.85E-28
Ogn	-2.08	3.56E-28
Col6a2	-1.74	5.07E-28
Fmo2	-1.64	6.72E-26
Colec12	-1.86	7.21E-26
Lbh	-2.02	2.39E-25
Scube2	-1.88	5.14E-25
Sod3	-2.03	1.17E-24
Mylk	-1.51	1.26E-24
Cdh11	-1.97	1.34E-24
Hsd11b1	-2.23	2.79E-23
Col6a3	-2.01	8.50E-22
Loxl1	-1.77	1.69E-21
Septin4	-1.68	1.82E-21
Itga8	-1.93	1.03E-20
Gyg	-1.54	3.04E-20
Col13a1	-1.87	8.31E-20

D

Gene name	Fold change	qvalue
Sftpc	1.92	1.83E-32
Rps19	2.55	1.98E-28
Eef1a1	1.45	1.75E-27
Rack1	1.89	5.06E-27
Gas5	2.04	1.78E-25
Tpt1	1.65	1.18E-24
Rps5	1.91	2.09E-24
Lyz2	3.22	1.07E-22
Rpl26	1.70	2.47E-22
Rplp0	1.80	8.12E-22
Rpl32	1.74	1.25E-21
Rps24	1.59	3.18E-21
Rpl23	1.34	6.69E-21
Rps14	1.36	2.32E-20
Rpl34	1.73	9.76E-20

Figure 37. Plin2^{lin} deciphers two LIF subpopulations during alveolarization. Data were generated by scRNAseq of Plin2^{lin} cells labeled at P1 and harvested at P7 and P14 from Plin2^{creERT2}; R26^{mTmG} mouse. (A) Reanalysis of scRNAseq data with higher resolution splits LIF (so far mentioned as cluster 3) into two LIF sub clusters (new cluster 3 and cluster 11). (B) DEGs between two sub clusters (Tcf21^{high} vs Tcf21^{low}) is shown as volcano plot. Genes with FDR < 0.05 (horizontal dash line) initially defined as

significantly up regulated genes in either of the groups. Black dots indicate not significantly changed expression between two groups. Tables show genes that are significantly up regulated in (C) cluster 11 ($Tcf21^{high}$) and (D) cluster 3 ($Tcf21^{low}$) over a manual cut-off (horizontal continues line) equal to log10 (10^{-20}).

Cluster $Tcf21^{high}$ was enriched in genes related to lung development such as Tcf21, Tbx2, Tbx4, Lox, Hsd11b1 and Mgp. In addition, genes related to extracellular matrix structural proteins e.g. collagen family members including Col1a1; Col1a2: Col3a1; Col6a2; Col6a3 and Col13a1 were expressed in the $Tcf21^{high}$ sub cluster. Top significantly up regulated genes (7.95E-91 ≤ FDR ≤ 1.13E-25) in $Tcf21^{high}$ and $Tcf21^{low}$ sub clusters are displayed in volcano plot (Figure. 37. B – D).

Moreover, to get an idea about functional attributes of identified cells, gene ontology enrichment was performed on top 30 significantly up regulated genes in each sub cluster (S 5 and S 6). Analysis did show that $Tcf21^{high}$ LIFs were mainly involved in extracellular matrix processes. They have regulatory functions through Tgfb1 and Pdgf signaling pathways and play a role in cell adhesion activities (S 5). On the other hand, $Tcf21^{low}$ LIFs were mainly engaged in ribosomal constituent, ribosomal binding in cytoplasm; thereby regulate translational activity (S4). Together, enrichment analysis indicated that $Tcf21^{high}$ and $Tcf21^{low}$ populations were associated with different biological processes and had various molecular functions. These observations strikingly claimed that $Plin2^{lin}$ comprises two subpopulations of LIFs: $Tcf21^{high}$ and $Tcf21^{low}$. Differentially expressed genes among these populations might serve as possible candidates to target LIF subpopulations. Expression of Plin2 in Tcf21 lineage traced cells has been demonstrated previously (Park et al., 2019).

In order to identify potential candidate genes to target the newly identified lipofibroblast cluster ($Tcf21^{high}$ cluster), an FDR cut-off between 9.80E-90 ≤ FDR ≤ 9.03E-05 was applied to up-regulated genes in the $Tcf21^{high}$ cluster. Furthermore, candidate genes showing (trans-) membrane localization in the cellular compartment were researched, while their specific expressions in the $Tcf21^{high}$ cluster was taken into consideration such as indolethylamine N-methyltransferase (Inmt) and CXC chemokine ligand 14 (CXCL14) (Figure. 38 A). Co-expression of listed genes with Tcf21 was examined by UMAP visualization. Results represented that overlap expression of most of these genes with Tcf21 was specific for the $Tcf21^{high}$ cluster (Figure. 38 B).

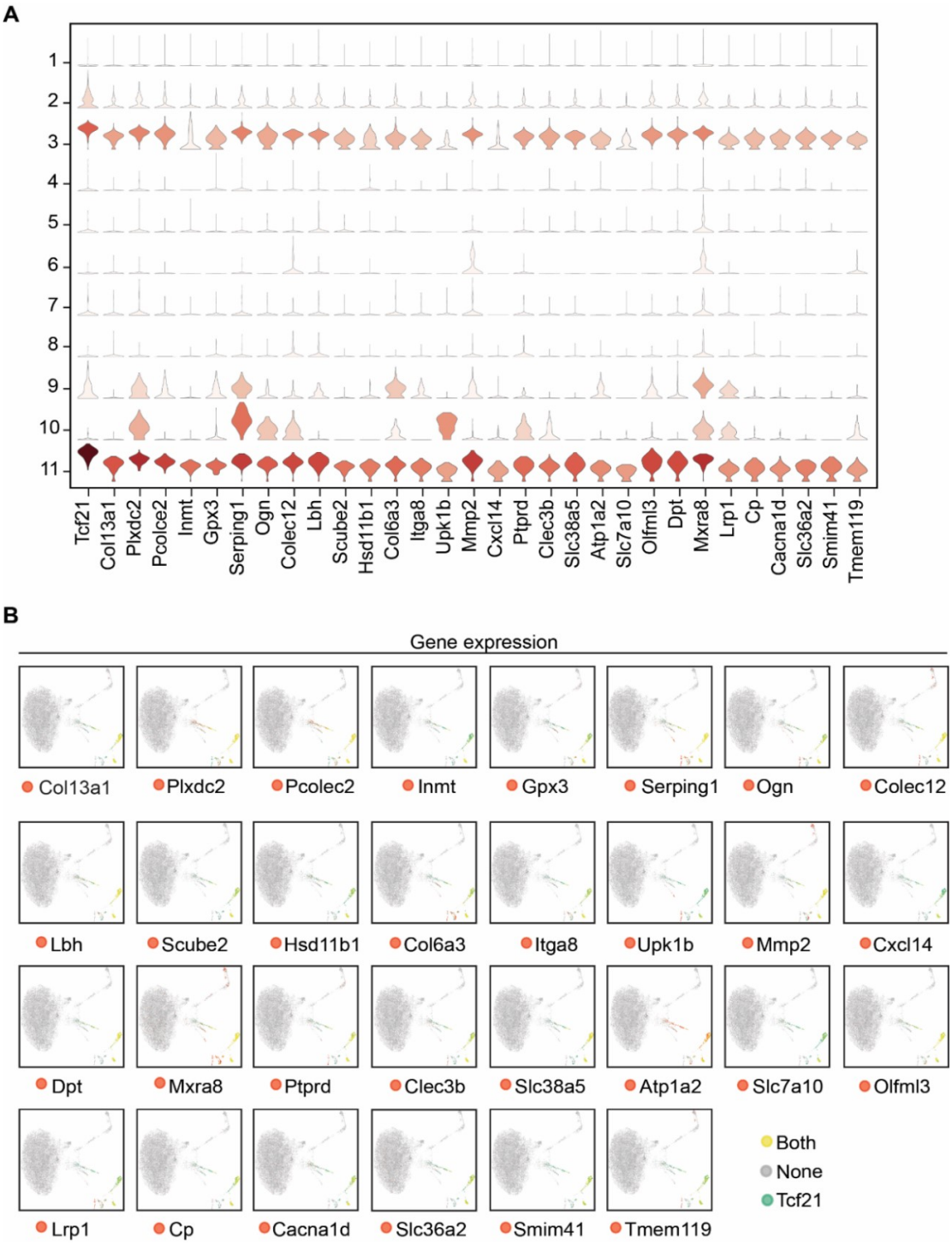

Figure 38. New potential candidates to target lipofibroblast populations. Data were generated by scRNAseq of Plin2^{lin} cells labeled at P1 and harvested at P7 and P14 from Plin2^{creERT2}; R26^{mTmG} mouse. scRNAseq data result were further analyzed to identify possible target candidates for LIF populations. (A) Stacked violin plot of selected genes amongst top 60 most significantly regulated genes in the Tcf21^{high} cluster. (B) UMAP embedding of clusters where individual cells are colored by Tcf21 expression (green), its co-expression with significantly regulated trans/membrane genes (yellow). Red dots represent only expression of significantly regulated (trans-) membrane genes. Gray indicates expression of none of them.

6 Discussion

6.1 Depletion of Plin2 expressing cells in mice during lung development and adulthood

First aim of the present study was to investigate function of $Plin2^{+}$ cells during postnatal lung development, in particular at the peak of alveolarization (secondary septation (P7)) and at the end of bulk alveolarization (P14) by induction of $Plin2^{+}$ cells depletion at P5 by Tmx injection of $Plin2^{creERT2+}$; $R26^{DTA+}$ mice. Impact of $Plin2^{+}$ cell ablation was investigated by morphological assessments, FACS and qPCR.

The findings revealed no changes in lung structure or the number of $Plin2^{+}$ cells. As Plin2 is known to be expressed in various organs, including the liver, kidney, and spleen (Ntokou et al., 2017), these organs were also assessed. Surprisingly, only the liver exhibited a significant effect of cell depletion on organ structure, with a steatosis-like morphology detected. Several studies have shown Plin2 is expressed in hepatocytes in the liver. (Chang et al., 2006; Najt et al., 2016; Straub et al., 2008). Hepatocytes are parenchymal cells of the liver responsible for mobilizing lipids for energy and storing excess lipids in the form of lipid droplets (Carr and Ahima, 2016). They constitute about 78-80 % of the liver tissue and perform critical functions such as metabolism, detoxification, protein synthesis/storage, and bile production and secretion (Bogdanos et al., 2013; Zhou et al., 2016). The $Plin2^{creERT2}$ driver used in this study is not a tissue specific cre driver, so it is likely that hepatocytes were also impacted. Diphtheria toxin A expression in Plin2-expressing hepatocytes may have triggered apoptosis and caused the destruction of these cells, leading to abnormal liver morphology and impaired function. This severe liver failure could have resulted in pathological symptoms in neonates. Results found that the structure of the lungs and the number of $Plin2^{+}$ cells ($mCherry^{+}$) were not affected by Tmx injection. One possible explanation for this is that the liver failure impeded Tmx metabolism, preventing cre recombination and $Plin2^{+}$ cell depletion in the lung.

Upon depletion, gene expression analysis in the lung showed upregulation of certain genes such as Plin2, Tcf21, Fabp4, and Lpl. This gene expression pattern in the lung was unexpected and may have been a response to the systemic effects of liver failure. Several studies have reported that liver failure could cause physiological complications in the lung. (Benz et al., 2020; Herrero et al., 2020; Martusewicz-Boros et al., 2013).

Up regulation of some genes like Plin2 and Tcf21 in the lungs might have been a reaction to this first hit. Furthermore, due to the limited time for cre recombination, depletion of Plin2-expressing cells could not be achieved, as DTA could not be expressed in the lung. Additionally, alterations in gene expression might suggest early changes in the lungs in response to liver failure. For instance, the upregulation of genes associated with lipid metabolism, including Fabp4 and Lpl, could be indicative of early lung damage. It has been shown by Tyler and collaborators that lung metabolic activation could be an early marker of acute respiratory distress syndrome (ARDS) (Wellman et al., 2016). Moreover, down-regulation of Arg1 could be an indication of initiation of inflammatory reactions in the lung. It has been described that the lungs are constantly exposed to the external environment, leading to a permanent basal inflammatory process. To maintain lung homeostasis, a delicate balance between pro-inflammatory and anti-inflammatory (pro-resolving) gene expression profile, in particular, M1 (pro-inflammatory) and M2 (Pro-resolving) macrophages (Bronte and Zanovello, 2005). Arg1 is one of the marker and effectors associated with M2 macrophages (Viola et al., 2019). Using this information, it could be hypothesize that the decrease in Arg1 expression could indicate an imbalance in the pro- and anti-inflammatory processes. This observation may also be consistent with metabolic alterations. On the contrary, the absence of significant changes in gene expression of other genes, such as Fgf10 and Thy1, could be attributed to differences in their expression patterns at different time points. Additionally, the lack of cell depletion could have contributed to the absence of significant changes in apoptosis-related markers, such as Parp1, Casp 3 and 8. Meanwhile, analysis of gene expression in the livers of the same neonates revealed downregulation of genes like Tcf21 and Lpl, while no significant changes were observed in other genes, such as Fabp4, Fgf10, Pparg, and Thy1. Drawing from a previous study on fetal liver, it could be postulated that the downregulation of Tcf21 is linked to activate hepatic stellate cells responding to an inflammatory stimulus. (Nakano et al., 2020). In contrast, research has indicated that Kupffer cells in the liver have a low capacity for synthesizing Lpl and instead, the liver obtains Lpl from the bloodstream (Camps et al., 1991). Additionally, it has been demonstrated that hepatocytes of the neonatal rat are the main Lpl-producing cell type in the liver (Burgaya et al., 1989; Enerbäck et al., 1988). These findings are consistent with our results and may provide an explanation for the observed reduction in Lpl

following cre recombination and potential hepatocyte depletion in the liver. However, additional evidence is needed to confirm this hypothesis. The observed upregulation of Tnfα and Parp1, which are upstream of the inflammatory and apoptotic cascades, respectively, suggest the onset of inflammatory and apoptotic processes in the liver. To summarize, the utilization of Plin2^{creERT2}; R26^{DTA} mice for Plin2-driven DTA expression did not result in the depletion of Plin2 cells in the lung, likely due to severe liver failure. As a result, an alternative approach was pursued to investigate the role of Plin2^{+} cells in alveolarization.

6.2 Lineage tracing of Plin2^{+} cells in mice in the adult lung and liver

Efforts to deplete Plin2^{+} cells in the lungs of both neonatal and adult mice using Plin2^{creERT2}; R26^{DTA} was unsuccessful. Therefore, it was necessary to re-evaluate the effectiveness of the Plin2^{creERT2} tool for targeting Plin2^{+} cells. In the same experimental setting used for depleting Plin2^{+} cells in adult mice, Plin2^{creERT2}; R26^{mTmG} adult mice were employed to label Plin2^{+} cells. The results showed the expression of GFP lineage label in the lung, as well as throughout the liver, as expected. These findings may provide evidence for Plin2-driven cre recombination in the liver of adult mice and further support the suitability of the Plin2^{creERT2} tool for targeting Plin2^{+} cells. It is worth noting that the lineage tracing of Plin2^{+} cells has previously been demonstrated in neonates. (Ntokou et al., 2017).

6.3 Molecular signatures and contribution of Plin2^{lin} cells during alveolarization

The objective of the current research was to investigate molecular characteristics of lipofibroblasts in the mouse lung, in order to gain new insights into their potential roles during the final stages of lung development. Lipofibroblasts in the lungs are a type of mesenchymal cell that contains lipids and is present in the alveolar niche, located at the base of the secondary septa, during murine lung alveolarization (Barkauskas et al., 2013; Brody and Kaplan, 1983; Burri, 1974; Kaplan et al., 1985; Ntokou et al., 2015a). In addition, lipofibroblasts have been shown to assist AECs II in production of surfactant (Rehan and Torday, 2003; Rehan et al., 2010; Torday and Rehan, 2002; Tordet et al., 1981). Lipofibroblasts express Plin2, which is a crucial component of cellular lipid droplets (Imamura et al., 2002; Rehan and Torday, 2003; Varisco et al., 2012; Wang et al., 2009) .

6.3.1 Identification of Plin2^{lin} derived cell clusters

FACS results indicated that Plin2^{lin} cells were present in both the green (GFP) and red channels at P7, however they were exclusively found in green channel at P14. The origin of red fluorescence was uncertain due to technical limitations, making it impossible to distinguish between mCherry and tdTomato fluorescent proteins in double-positive cells (i.e., cells that were both red^{+} and GFP^{+}) at P7. The number of GFP^{+} cells was higher at P14 compared to P7, potentially due to increased cre recombination in Plin2^{+} cells and proliferation of Plin2^{lin} progeny. (S 1). A clear lineage cell population could be collected successfully at P7 and P14 after Tmx induction at P1. The lineage label GFP was strongly expressed at both time points. By employing single cell sequencing, 7 distinct clones were identified at both time points. However, the distribution of these cells across the clusters differed between the two time points, which was anticipated due to the different cellular populations that reached their maximum levels at various stages during alveolarization. (Branchfield et al., 2016b). This finding highlights the dynamics of cell differentiation during alveolarization. Cluster 1 consisted of a similar proportion of cells from both P7 and P14, indicating that these cells might have committed to their cell fate during the early embryonic stages before P1. This assertion is in agreement with the fact that cluster 1 was later identified as AECs II, while AECs I differentiate during the initial stages of lung development. Conversely, cluster 5 was exclusively derived from P7 cells and not P14 cells. It is plausible that these cells possessed the potential to differentiate into other cell types after P7. Based on their transcriptional profile, these cells were categorized as less differentiated cells that may have differentiated later in development. According to Semrau et al., the emergence of embryonic stem cells with pluripotency markers signals the onset of lineage transition. (Semrau et al., 2017). Cell type identification was accomplished through unsupervised clustering and supervised annotation. The "Lega web portal" was utilized to determine the top regulated genes per cluster. This information was then combined with literature-based knowledge to achieve successful and precise cell type annotation. (Du et al., 2015; Du et al., 2017; Du et al., 2021). Although, initial aim of this investigation was to utilize Plin2^{creERT2}; R26^{mTmG} to describe mesenchymal LIF during alveolarization, but the outcomes were unforeseen as they revealed that not only mesenchymal cells but also non-mesenchymal cells originated from Plin2-expressing cells at P1. Furthermore, cluster 2 exhibited a composite

transcriptional profile, and its annotation to a specific cell type was unattainable. Cells in this cluster could be doublets formed during the 10X sequencer's process.

6.3.2 Non-mesenchymal cell clusters of P1 Plin2^{lin} cells during alveolarization

A high representation of epithelial cell clusters was observed, primarily composed of AECs I and II, which are specialized cells found in alveoli. AECs II produce surfactant, which reduces surface tension and prevents alveolar collapse during exhalation. Cluster 1 expressed surfactant protein genes, aligning with its AEC II characteristics. This suggests a potential role for epithelial Plin2^{lin} in surfactant production. Unexpectedly, AECs II and I showed a divergence from Plin2^{lin}, which was confirmed through protein level identification by IF staining and gene expression level identification by cell sorting and qPCR analyses. Although not all Sftpc^{+} and Pdpn^{+} cells were lineage labelled, Plin2^{lin} cells could label specific subpopulations of AECs, indicating a lineage relationship between Plin2^{lin} and AECs II and I. Previous research has shown that these cells originate from a common progenitor cell with bipotent properties during early lung development. (Desai et al., 2014; Treutlein et al., 2014). Due to their pluripotency, possibly, these progenitor cells might possess mesenchymal characteristics, suggesting that Plin2^{lin} cells could potentially label both populations of AECs. According to Desai et al. AECs II cells have been identified as progenitor cells for AECs I during homeostasis and after injury (Desai et al., 2014). Furthermore, AECs I transition into AECs II has been suggested (Jain et al., 2015). This finding might help to clarify that Plin2^{lin} derived AECs I could have originated from Plin2^{lin} derived AECs II, and might elucidate the close vicinity of these clusters (cluster 2 and 6). Existence of several subpopulations of AECs II has been reported (Chapman et al., 2011; Vaughan et al., 2015). Previous research has reported the existence of several subpopulations of AECs II, including a population of Integrin α6β4 expressing AECs II that does not express Prosurfactant protein C (SPC) (Chapman et al., 2011) . These publications supports the possibility, that Plin2^{lin} derived AECs II might also include an unrecognized subpopulation of AECs II and further explain the presence of two epithelial Plin2^{lin} subpopulations: (1) Plin2^{+} AECs II and (2) Plin2^{-} AECs II. Finally, Epithelial to mesenchymal transition (EMT) has been reported during disease conditions (Kim et al., 2006). However, the contribution of epithelial Plin2^{lin} cells to the plasticity and homeostasis of AECs1 and AECs2 during development, injury, and

regeneration remains to be explored. Contrary to this, result from a wild-type mouse at P1 in the present study indicate that Plin2^{+} AECs II already existed at this stage. Therefore, the EMT process of Plin2^{lin} during alveolarization needs to be elucidated.

It has been shown that all ECs could be traced by cre driver mouse lines such as Cdh5^{creERT2} and Pdgfb^{creERT2} mouse lines (Bazigou et al., 2011; Cai et al., 2016; Kalna et al., 2019). Additionally, different developmental origins of EC subtypes in the lung have been described, with cardiopulmonary progenitor cells being involved in early lung development, endothelial progenitor cells being involved later in development and already existing ECs contributing to the development of EC subtypes (Bolte et al., 2018; Liao et al., 2009; Peng et al., 2013). The present study demonstrated that Plin2^{creERT2} contributes to ECs during late alveolarization, possibly introducing a new origin for ECs in mice. Endothelial cells have been shown to play an important role in the alveolar secondary septum formation and were proposed to have a leading position in alveolarization and neo-alveolarization (Burri, 1974; Ding et al., 2011; Maksvytis et al., 1981; Yamamoto et al., 2007). Therefore, to better understand pulmonary diseases related to EC functions, it is crucial to explore the signature of pulmonary ECs, including Plin2^{lin}-derived ECs. To achieve this goal, conserved EC marker genes in mice and humans were analyzed in the present study. Data verified the heterogeneity of Plin2^{lin}-derived ECs based on the expression of EC markers. Although higher resolution analysis revealed two EC subpopulations (Cluster 6 and 8), the distinction of EC sub clusters based on conserved EC markers was not clear. Nevertheless, Plin2^{lin} contributed to a small EC population comprising arterial and capillary ECs. The transcriptional profile of endothelial Plin2^{lin} cells, alongside their localization in parenchyma and septal wall, confirmed that specific EC subpopulations were labeled. This raised the question where did this small Plin2^{lin}-driven EC population come from. Were they derived from endothelial cells that already existed at earlier developmental stages and expressed Plin2, or did they undergo some cell fate transition? Recently, mesenchymal-endothelial transition during cardiac neovascularization after heart injury has been suggested (Farbehi et al., 2019; Saraswati et al., 2019; Ubil et al., 2014). However, this dogma is still full of controversies and requires further investigation.

6.3.3 Contribution of Plin2^{lin} cells to mesenchymal cell populations during alveolarization

Among 7 identified cell clusters, cluster 3 and cluster 7 were annotated as mesenchymal clusters lipofibroblasts (cluster 3) and myofibroblasts (cluster 7). Plin2 has been demonstrated by multiple studies as a marker, which labels pulmonary mesenchymal lipid-laden fibroblast or so-called “Lipofibroblast” (Imamura et al., 2002; McGowan, 2019; McGowan and McCoy, 2014; Ntokou et al., 2015a; Varisco et al., 2012). Here, results provided evidence that Plin2^{lin} comprises different populations during alveolarization in addition to the identified non-mesenchymal. Based on the Vim expression as abundant but unspecific marker for mesenchymal cells (Ridge et al., 2022) cells with mesenchymal character were identified. Annotation of cluster specific gene expression revealed MFs and LIFs, at both, the peak and the end of bulk alveolarization.

According to the data, most of the Plin2-related myofibroblasts (MFs) were identified during the peak of alveolarization, at P7. Nonetheless, MFs were also identifiable at P14. Previous research has identified Acta2 as a standard marker for MFs in both developmental and pathological conditions in the lungs. (Jiang et al., 2021; Karvonen et al., 2013; Moiseenko et al., 2017). Results showed that only cluster 7, identified as MFs, and had high expression of Acta2 and Des. Furthermore, the co-expression of extracellular matrix components, such as elastin and transgelin, indicated that Plin2-derived MFs might have a role in producing the extracellular matrix. The protein level confirmation of Plin2-derived MF population was done using IF staining. Interestingly, the αSMA+ cells at the tip of secondary septa did not express the GFP lineage label. This suggests that MFs in the distal lung arise from different progenitors and may have distinct roles during late alveolarization, despite their phenotypic similarities. In addition, Pdgfrα expression was detected in both the identified mesenchymal LIF and MF populations, which supports their annotation as PDGFRα serves as a progenitor marker for both MFs and LIFs during lung development and neo-alveolarization. (Bostrom et al., 1996; Chen et al., 2012; Li et al., 2018b; Lindahl et al., 1997; McGowan and McCoy, 2011). Differential gene expression analysis identified many shared genes between the two mesenchymal populations, indicating a potential common ancestor during early developmental stages. However, up-regulated genes in either of these two mesenchymal subpopulations demonstrated their unique myo- and lipo-fibroblastic phenotype, and provided new insights into their particular molecular signatures.

Overall, the lack of specific markers to target mesenchymal fibroblast subpopulations limits our understanding of their biological and pathological functions in the lung. (Cardoso and Whitsett, 2008; Xie et al., 2018). Comparing expression levels of certain surface proteins may help to distinguish MF and LIF populations from each other. As such, data set was searched for surface genes in the MF and LIF clusters. Significantly regulated genes in either of the MF and LIF populations demonstrated a transcriptional profile similar to already available mouse lung single cell cohorts of MFs and LIFs and new candidates. Therefore, this study identified new potential surface candidates to target MFs and LIFs.

The current dataset showed that Plin2^{lin} cells expressed suggested LIF markers, such as Plin2 and Tcf21. Additionally, Tcf21 expression was found to be restricted to mesenchymal cells. Furthermore, the data suggested that Plin2 expression levels in LIFs were lower compared to Tcf21 expression levels, which is consistent with previous studies. (Liu et al., 2021; McGowan and McCoy, 2014). Therefore, Tcf21 represents a more specific marker for targeting LIFs during late lung development, as previously suggested by Park and collaborators (Park et al., 2019). However, the low detection rate of other known LIF markers, such as Thy1, Pparg, and Fgf10 by the defined LIF population might be due to their complete differentiation, as these genes mainly act during LIF differentiation and regulate differentiation (Al Alam, 2013; Varisco, 2012). As expected, Plin2 expression at protein level confirmed previous studies and showed widespread expression in distal alveolar regions. Surprisingly, the strongest expression of Tcf21 and Collagen (Col) 13a1 was detected in the lipofibroblast cluster, which aligns with findings of Park et al. They used genetic tracing techniques to characterize the Tcf21 cell lineage and showed that pulmonary LIFs are derived from the Tcf21 lineage. They reported that Col13a1 expression is not only expressed in the Tcf21 lineage (Tcf21^{lin}) but is also found in other lipid-laden cell types (Park et al., 2019). Additionally, Green et al. identified Col13a1 expression as one of the genes differentially expressed in the Pdgfrα^{+} population (Green et al., 2016). Higher resolution analyses of the generated scRNAseq data demonstrated two LIF sub clusters. One cluster expressed higher level of Tcf21 (Tcf21^{high}) and appeared only at P14. The second LIF cluster showed lower Tcf21 expression (Tcf21^{low}) and appeared at P7 (Figure. 23 C). Differential expression analysis between the two LIF clusters showed a striking difference in the expression of ribosomal protein genes (PPGs) in the Tcf21^{low}

cluster. Petibon et al. conducted a review on the regulation of RPGs, providing an overview of how changes in growth conditions and cellular status are responsible for regulating the expression of ribosomal protein genes through two overlapping regulatory circuits. These circuits are (1) the classical general ribosomal-producing program and (2) gene-specific features that fine-tune the amount of ribosomal proteins produced from each individual ribosomal gene (Petibon et al., 2021). The combination of these two circuits might explain the presence of different member of ribosomal protein family at earlier time point (P7). Therefore, cells in the Tcf21^{low} population might be able to meet cellular basic needs while allowing functional specialization and divergence. Whereas, cells of the Tcf21^{high} cluster might already be committed to their final fate and express genes that are more specific. Differential expressed genes between these two LIF subpopulations were further searched for a set of surface proteins with similar expression pattern as Tcf21 amongst significantly upregulated genes in the Tcf21^{high} cluster. Surface protein candidates, which were exclusively express in Tcf21^{high} cluster and are either absent or low-expressed in the other Plin2^{lin}-derived clusters except Tcf21^{low}. However, only a couple of genes were exclusively expressed in the Tcf21^{high} compare to the Tcf21^{low} cluster were of great interest. Luckily, only few genes were exclusively expressed in the Tcf21^{high} cluster in comparison with the Tcf21^{low} cluster such as Indolethylamine N-methyltransferase (Inmt), Chemokine (C-X-C motif) ligand 14 (Cxcl14) and Solute carrier family 7 , member 10 (Slc7a10). Cxcl14 is a relatively novel chemokine that its contribution into EMT has been demonstrated in cancer cell biology and idiopathic pulmonary fibrosis (Chang et al., 2023; Jia et al., 2017; Rodriguez et al., 2018). On the other hand, Slc7a10 is a protein that plays a key role in neutral amino acid transport across the cellular membrane. It has been shown to be involved in adipocyte lipid storage in both humans and mice. Additionally, Slc7a10 expression has been reported in collagen-producing lung fibroblasts. (Jersin et al., 2021; Tsukui et al., 2020). Finally, Inmt is an enzyme and its activity was first reported in the rabbit lung (Chu et al., 2014). In a single cell study on resident lung mesenchymal stromal cells in BPD, Inmt expression in Co13a1 expressing fibroblasts was demonstrated (Mizikova et al., 2022). Furthermore, Inmt has been reported to be involved in lung cancer biology (Zhou et al., 2022). Taken together genes identified in the present study might serve as potential candidates to target Tcf21^{high}

lipofibroblasts to further elucidate distinct functions during secondary septation and alveolarization.

7 Conclusion

The present study aimed to characterize cells of Plin2 cell lineage ($Plin2^{lin}$) using a depletion and a lineage tracing approach. Generated data of this study demonstrated that Plin2 driven diphtheria toxin A expression using $Plin2^{creERT2}$; $R26^{DTA}$ mice lead to strong liver failure and thus failed to deplete pulmonary cells of the $Plin2^{lin}$ in postnatal and adult mice. Liver failure provoked systemic pathologic conditions in murine neonates and adult mice, which hindered further analyses on lung samples due to the lack of depletion in the lung. Furthermore, $Plin2^{creERT2}$ mice could successfully be used to label cells of the $Plin2^{lin}$. Using $Plin2^{creERT2}$; $R26^{mTmG}$ mice in a single cell RNA sequencing approach, $Plin2^{lin}$ cells were found to contribute to non-mesenchymal and mesenchymal mouse lung cell populations during alveolarization. Cells of the $Plin2^{lin}$ from postnatal day (P) 1 comprised epithelial and endothelial cell clusters as well as mesenchymal myo- and lipo-fibroblast populations during the peak of secondary septation (P7) and the end of bulk secondary septation (P14). It was unexpected, that the $Plin2^{lin}$ labeled non-mesenchymal cell populations. However, immunofluorescence staining of respective lung sections and imaging using confocal laser scanning microscopy confirmed the existence of $Plin2^{lin}$ driven alveolar epithelial cells (AECs) and endothelial cells. Lipofibroblasts derived from P1 Plin2 positive ($^{+}$) cells displayed similar molecular signatures to previously performed studies characterizing pulmonary lipofibroblasts. Deeper analyses of generated scRNAseq data revealed two distinct lipofibroblast populations based on the level of Tcf21 expression. Based on Tcf21 expression, one lipofibroblast population expressed Tcf1 to a high extend ($Tcf21^{high}$) and the other lipofibroblast population demonstrated low expression of Tcf21 ($Tcf21^{low}$). Analysis of differentially expressed genes among these sub clusters revealed new potential target candidates to better target lipofibroblast populations during alveolarization in the future. Inmt, Slc7a10 and Cxcl14 were identified as possible candidates. Future studies will elucidate which marker might serve as most suitable candidate to target the $Tcf21^{high}$ population. Targeting the $Tcf21^{high}$ lipofibroblast population, possible functions of the newly identified lipofibroblast populations can be elucidated.

8 Summary

Disrupted alveolar morphology characterizes various pulmonary structural diseases, such as bronchopulmonary dysplasia, chronic obstructive pulmonary disease and lung fibrosis. Understanding the process of lung alveolarization might help to develop new therapeutic strategies for pulmonary structural diseases. Cells expressing the protein Perilipin2 (Plin2); synonym: Adipocyte differentiation-related protein (ADRP, synonym), known as lipofibroblasts have been demonstrated to participate in lung alveolarization. Aim of the present study was 1) to analyze function of cells of the Plin2 cell lineage ($Plin2^{lin}$) during alveolarization using a cell depletion approach in transgenic mice and (2) to characterize molecular signatures of $Plin2^{lin}$ cells during alveolarization using a single cell sequencing approach of murine lineage traced cells of the $Plin2^{lin}$ cell lineage. Using a cre-recombinase (cre) stop loxP Diphtheria toxin A (DTA) system in mice, the current work demonstrated that tamoxifen administration and following cell specific cre recombination in order to ablate Plin2-expressing cells during alveolarization caused to a strong liver failure. Ablation of $Plin2^{lin}$ cells in the lung could not be detected. In contrast, using a cre driven cell specific activation of the reporter gene green fluorescent protein (GFP), $Plin2^{lin}$ cells in the lung could be labelled successfully. To elucidate molecular signatures and contribution of $Plin2^{lin}$ cells to mouse lung cell populations during alveolarization, single-cell RNA sequencing (scRNAseq) of lineage-traced cells was achieved. ScRNAseq was performed on about 8791 and 9095 $Plin2^{lin}$ cells from postnatal day (P) 1 at P7 and P14. Seven major clusters from the $Plin2^{lin}$ were identified. Strikingly, these clusters of the $Plin2^{lin}$ were annotated as epithelial, mesenchymal and vascular cell populations. High-quality imaging on 150 µm precision-cut lung slices from P7 and P14 lungs confirmed cell type markers of annotated cell types. Moreover, two subpopulations of lipofibroblasts were identified: Transcription factor 21 (Tcf21) -low expressing and Tcf21-high expressing mesenchymal lipofibroblasts. Comparison of differentially expressed genes of the two different identified lipofibroblast subpopulations revealed possible target candidate genes, which might contribute to better targeting and better understanding of lipofibroblast subtypes during alveolarization. Generated data serve as an important basis for further studies to gain insights into possible functions of lipofibroblast populations in alveolarization.

9 Zusammenfassung

Ein zentrales Merkmal struktureller Lungenerkrankungen wie beispielsweise der bronchopulmonalen Dysplasie, der chronisch obstruktiven Lungenerkrankung und der Lungenfibrose ist eine gestörte alveoläre Lungenstruktur. Das Verständnis über den Prozess der Lungenalveolarisierung könnte zur Entwicklung neuer therapeutischer Strategien für strukturelle Lungenerkrangungen beitragen. Zellen, die das Protein Perilipin2 (Plin2); Synonym: Adipocyte differentiation-related protein (ADRP) exprimieren wurden als Lipofibroblasten identifiziert, die an der Lungenalveolarisierung teilnehmen. Das Ziel der vorliegenden Arbeit war es (1) die Funktion der Plin2 Zelllinie in der Alveolarisierung durch einen Ansatz der Zelldepletion zu untersuchen und (2) durch die Anwendung der Einzelzell-RNA-Sequenzierungsmethode molekulare Signaturen der Plin2 Zelllinie in der Alveolarisierung und deren Beitrag zu Zellpopulationen während der Alveolarisierurng zu analysieren. In der vorliegenden Arbeit wurde in transgenen Mäusen gezeigt, dass die zellspezifische Aktivierung des Cre-Rekombinase (Cre)-stop loxP Diphteria toxin A (DTA) Systems mittels Tamoxifen in Zellen der Plin2 Zell-linie mit dem Ziel der Zelldepletion während der Alveolisierung zu einer starken Leberinsuffizienz führte. In der Lunge konnte keine Zelldepletion nachgewiesen werden. Allerdings konnte mit Cre vermitteler Aktivierung des Reportergens Green fluorescence protein (GFP) eine klare Markierung von Zellen der Plin2 Zelllinie in der Lunge erreicht werden. Mittels Einzelzell-RNA-Sequenzierung (scRNAseq) wurden molekulare Signaturen dieser Zellen und ihr Beitrag zu Zellpopulationen in der Alveolarisierung der murinen Lunge analysiert. Die scRNAseq Analyse wurde an etwa 8791 und 9095 Zellen der Plin2 Zell-linie ($Plin2^{lin}$) von postnatal Tag (P) 1 an P7 und P14 durchgeführt, So wurden sieben Zellcluster der $Plin2^{lin}$ identifiziert. Erstaunlicherweise wurden diese Cluster als epitheliale, mesenchymale und vaskuläre Zellpopulationen an Hand Ihrer Genexpressionmuster charakterisiert. Hochqualitative Bildgebung an 150 µm präzisionsgeschnittenen Lungenschnitten von P7- und P14-Lungen bestätigte die Zelltypmerkmale der identifizierten Zellcluster. Darüber hinaus wurden zwei Subpopulationen von Lipofibroblasten identifiziert: Transcriptionsfaktor 21 (Tcf21) gering exprimierende und Tcf21-hoch exprimierende mesenchymale Lipofibroblasten. Durch den Vergleich der differentiel exprimierten Gene beider Subpopulationen waurden mögliche Zielgene identifiziert, die dazu beitragen könnten,

Lipofibroblastensubpopulationen während der Alveolisation selektiv zu treffen, um deren Funktion besser analysieren zu können. Die generierten Daten stellen eine wichtige Basis für zukünftige Studien dar, um weiter Einblicke in mögliche Funktionen von Lipofibroblastenpopulationen in der Alveolarisierung zu gewinnen.

10 Bibliography

Al Alam, D.E.A., E.:Sakurai, R.:Kheirollahi, V.:Moiseenko, A.:Danopoulos, S.:Shrestha, A.:Schmoldt, C.:Quantius, J.:Herold, S.:Chao, C. M.:Tiozzo, C.:De Langhe, S.:Plikus, M. V.:Thornton, M.:Grubbs, B.:Minoo, P.:Rehan, V. K.:Bellusci, S., 2015. Evidence for the involvement of fibroblast growth factor 10 in lipofibroblast formation during embryonic lung development. Development (Cambridge, England) 142, 4139-4150.

Al Alam, D.E.A., Elie:Danopoulos, Soula:Rehan, Virender:Bellusci, Saverio, 2013. FGF10 identifies early lipofibroblast progenitors and controls their fate during embryonic lung development. 42, P4880.

Alanis, D.M., Chang, D.R., Akiyama, H., Krasnow, M.A., Chen, J., 2014. Two nested developmental waves demarcate a compartment boundary in the mouse lung. Nature Communications 5, 3923.

Annoni, R., Lanças, T., Tanigawa, R.Y., Matsushita, M.d.M., Fernezlian, S.d.M., Bruno, A., Silva, L.F.F.d., Roughley, P.J., Battaglia, S., Dolhnikoff, M., Hiemstra, P.S., Sterk, P.J., Rabe, K.F., Mauad, T., 2012. Extracellular matrix composition in COPD. European Respiratory Journal 40, 1362-1373.

Awonusonu, F., Srinivasan, S., Strange, J., Al-Jumaily, W., Bruce, M.C., 1999. Developmental shift in the relative percentages of lung fibroblast subsets: role of apoptosis postseptation. American Journal of Physiology-Lung Cellular and Molecular Physiology 277, L848-L859.

Barkauskas, C.E., Cronce, M.J., Rackley, C.R., Bowie, E.J., Keene, D.R., Stripp, B.R., Randell, S.H., Noble, P.W., Hogan, B.L., 2013. Type 2 alveolar cells are stem cells in adult lung. J Clin Invest 123, 3025-3036.

Barnes, P.J., 2014. Cellular and Molecular Mechanisms of Chronic Obstructive Pulmonary Disease. Clinics in Chest Medicine 35, 71-86.

Barnes, P.J., 2016. Inflammatory mechanisms in patients with chronic obstructive pulmonary disease. Journal of Allergy and Clinical Immunology 138, 16-27.

Barnes, P.J., 2017. Cellular and molecular mechanisms of asthma and COPD. Clin Sci (Lond) 131, 1541-1558.

Basil, M.C., Morrisey, E.E., 2020. Lung regeneration: a tale of mice and men. Semin Cell Dev Biol 100, 88-100.

Bazigou, E., Lyons, O.T.A., Smith, A., Venn, G.E., Cope, C., Brown, N.A., Makinen, T., 2011. Genes regulating lymphangiogenesis control venous valve formation and maintenance in mice. The Journal of Clinical Investigation 121, 2984-2992.

Benz, F., Mohr, R., Tacke, F., Roderburg, C., 2020. Pulmonary Complications in Patients with Liver Cirrhosis. J Transl Int Med 8, 150-158.

Bickel, P.E., Tansey, J.T., Welte, M.A., 2009. PAT proteins, an ancient family of lipid droplet proteins that regulate cellular lipid stores. Biochim Biophys Acta 1791, 419-440.

Bogdanos, D.P., Gao, B., Gershwin, M.E., 2013. Liver immunology. Compr Physiol 3, 567-598.

Bolte, C., Whitsett, J.A., Kalin, T.V., Kalinichenko, V.V., 2018. Transcription Factors Regulating Embryonic Development of Pulmonary Vasculature, in: Parthasarathi, K. (Ed.), Molecular and Functional Insights Into the Pulmonary Vasculature. Springer International Publishing, Cham, pp. 1-20.

Bostrom, H., Willetts, K., Pekny, M., Leveen, P., Lindahl, P., Hedstrand, H., Pekna, M., Hellstrom, M., Gebre-Medhin, S., Schalling, M., Nilsson, M., Kurland, S., Tornell, J., Heath, J.K., Betsholtz, C., 1996. PDGF-A signaling is a critical event in lung alveolar myofibroblast development and alveogenesis. Cell 85, 863-873.

Boström, H., Willetts, K., Pekny, M., Levéen, P., Lindahl, P., Hedstrand, H., Pekna, M., Hellström, M., Gebre-Medhin, S., Schalling, M., Nilsson, M., Kurland, S., Törnell, J., Heath, J.K., Betsholtz, C., 1996. PDGF-A Signaling Is a Critical Event in Lung Alveolar Myofibroblast Development and Alveogenesis. Cell 85, 863-873.

Branchfield, K., Li, R., Lungova, V., Verheyden, J.M., McCulley, D., Sun, X., 2016a. A three-dimensional study of alveologenesis in mouse lung. Developmental Biology 409, 429-441.

Branchfield, K., Li, R., Lungova, V., Verheyden, J.M., McCulley, D., Sun, X., 2016b. A three-dimensional study of alveologenesis in mouse lung. Dev Biol 409, 429-441.

Brody, J.S., 1985. Cell-to-cell interactions in lung development. Pediatr Pulmonol 1, S42-48.

Brody, J.S., Kaplan, N.B., 1983. Proliferation of alveolar interstitial cells during postnatal lung growth. Evidence for two distinct populations of pulmonary fibroblasts. Am Rev Respir Dis 127, 763-770.

Bronte, V., Zanovello, P., 2005. Regulation of immune responses by L-arginine metabolism. Nature Reviews Immunology 5, 641-654.

Burgaya, F., Peinado, J., Vilaró, S., Llobera, M., Ramírez, I., 1989. Lipoprotein lipase activity in neonatal-rat liver cell types. Biochem J 259, 159-166.

Burri, P.H., 1974. The postnatal growth of the rat lung. 3. Morphology. Anat Rec 180, 77-98.

Burri, P.H., 1985. Development and Growth of the Human Lung, Comprehensive Physiology, pp. 1-46.

Burri, P.H., 2006. Structural aspects of postnatal lung development - alveolar formation and growth. Biol Neonate 89, 313-322.

Cai, Y., Bolte, C., Le, T., Goda, C., Xu, Y., Kalin, T.V., Kalinichenko, V.V., 2016. FOXF1 maintains endothelial barrier function and prevents edema after lung injury. Science Signaling 9, ra40-ra40.

Camps, L., Reina, M., Llobera, M., Bengtsson-Olivecrona, G., Olivecrona, T., Vilaró, S., 1991. Lipoprotein lipase in lungs, spleen, and liver: synthesis and distribution. J Lipid Res 32, 1877-1888.

Cardoso, W.V., Whitsett, J.A., 2008. Resident cellular components of the lung: developmental aspects. Proc Am Thorac Soc 5, 767-771.

Carr, R.M., Ahima, R.S., 2016. Pathophysiology of lipid droplet proteins in liver diseases. Experimental cell research 340, 187-192.

Carvalho, O., Gonçalves, C., 2011. Comparative Physiology of the Respiratory System in the Animal Kingdom. The Open Biology Journal 4.

Chambers, D.C., Carew, A.M., Lukowski, S.W., Powell, J.E., 2019. Transcriptomics and single-cell RNA-sequencing. Respirology 24, 29-36.

Chanda, D., Kurundkar, A., Rangarajan, S., Locy, M., Bernard, K., Sharma, N.S., Logsdon, N.J., Liu, H., Crossman, D.K., Horowitz, J.C., De Langhe, S., Thannickal, V.J., 2016. Developmental Reprogramming in Mesenchymal Stromal Cells of Human Subjects with Idiopathic Pulmonary Fibrosis. Sci Rep 6, 37445.

Chang, B.H., Li, L., Paul, A., Taniguchi, S., Nannegari, V., Heird, W.C., Chan, L., 2006. Protection against fatty liver but normal adipogenesis in mice lacking adipose differentiation-related protein. Mol Cell Biol 26, 1063-1076.

Chang, T.M., Chiang, Y.C., Lee, C.W., Lin, C.M., Fang, M.L., Chi, M.C., Liu, J.F., Kou, Y.R., 2023. CXCL14 promotes metastasis of non-small cell lung cancer through ACKR2-depended signaling pathway. Int J Biol Sci 19, 1455-1470.

Chao, C.-M., Moiseenko, A., Zimmer, K.-P., Bellusci, S., 2016. Alveologenesis: key cellular players and fibroblast growth factor 10 signaling. Molecular and Cellular Pediatrics 3, 17.

Chao, C.-M.E.A., Elie:Tiozzo, Caterina:Minoo, Parviz:Bellusci, Saverio, 2015. A Breath of Fresh Air on the Mesenchyme: Impact of Impaired Mesenchymal Development on the Pathogenesis of Bronchopulmonary Dysplasia.

Chapman, H.A., Li, X., Alexander, J.P., Brumwell, A., Lorizio, W., Tan, K., Sonnenberg, A., Wei, Y., Vu, T.H., 2011. Integrin α6β4 identifies an adult distal lung epithelial population with regenerative potential in mice. The Journal of Clinical Investigation 121, 2855-2862.

Chen, L., Acciani, T., Le Cras, T., Lutzko, C., Perl, A.K., 2012. Dynamic regulation of platelet-derived growth factor receptor alpha expression in alveolar fibroblasts during realveolarization. Am J Respir Cell Mol Biol 47, 517-527.

Chu, U.B., Vorperian, S.K., Satyshur, K., Eickstaedt, K., Cozzi, N.V., Mavlyutov, T., Hajipour, A.R., Ruoho, A.E., 2014. Noncompetitive Inhibition of Indolethylamine-N-methyltransferase by N,N-Dimethyltryptamine and N,N-Dimethylaminopropyltryptamine. Biochemistry 53, 2956-2965.

Chung, M.I., Bujnis, M., Barkauskas, C.E., Kobayashi, Y., Hogan, B.L.M., 2018. Niche-mediated BMP/SMAD signaling regulates lung alveolar stem cell proliferation and differentiation. Development (Cambridge, England) 145.

Ciechanowicz, A., 2019. Stem Cells in Lungs. Adv Exp Med Biol 1201, 261-274.

Cupello, C., Hirasawa, T., Tatsumi, N., Yabumoto, Y., Gueriau, P., Isogai, S., Matsumoto, R., Saruwatari, T., King, A., Hoshino, M., Uesugi, K., Okabe, M., Brito, P.M., 2022. Lung evolution in vertebrates and the water-to-land transition. eLife 11, e77156.

deMello, D.E., Reid, L.M., 2000. Embryonic and early fetal development of human lung vasculature and its functional implications. Pediatr Dev Pathol 3, 439-449.

Desai, T.J., Brownfield, D.G., Krasnow, M.A., 2014. Alveolar progenitor and stem cells in lung development, renewal and cancer. Nature 507, 190-194.

Ding, B.S., Nolan, D.J., Guo, P., Babazadeh, A.O., Cao, Z., Rosenwaks, Z., Crystal, R.G., Simons, M., Sato, T.N., Worgall, S., Shido, K., Rabbany, S.Y., Rafii, S., 2011. Endothelial-derived angiocrine signals induce and sustain regenerative lung alveolarization. Cell 147, 539-553.

Dirami, G., Massaro, G.D., Clerch, L.B., Ryan, U.S., Reczek, P.R., Massaro, D., 2004. Lung retinol storing cells synthesize and secrete retinoic acid, an inducer of alveolus formation. Am J Physiol Lung Cell Mol Physiol 286, L249-256.

Dobin, A., Davis, C.A., Schlesinger, F., Drenkow, J., Zaleski, C., Jha, S., Batut, P., Chaisson, M., Gingeras, T.R., 2013. STAR: ultrafast universal RNA-seq aligner. Bioinformatics 29, 15-21.

Doherty, D.F., Roets, L., Krasnodembskaya, A.D., 2023. The role of lung resident mesenchymal stromal cells in the pathogenesis and repair of chronic lung disease. Stem Cells.

Du, Y., Guo, M., Whitsett, J.A., Xu, Y., 2015. 'LungGENS': a web-based tool for mapping single-cell gene expression in the developing lung. Thorax 70, 1092-1094.

Du, Y., Kitzmiller, J.A., Sridharan, A., Perl, A.K., Bridges, J.P., Misra, R.S., Pryhuber, G.S., Mariani, T.J., Bhattacharya, S., Guo, M., Potter, S.S., Dexheimer, P., Aronow, B., Jobe, A.H., Whitsett, J.A., Xu, Y., 2017. Lung Gene Expression Analysis (LGEA): an integrative web portal for comprehensive gene expression data analysis in lung development. Thorax 72, 481-484.

Du, Y., Ouyang, W., Kitzmiller, J.A., Guo, M., Zhao, S., Whitsett, J.A., Xu, Y., 2021. Lung Gene Expression Analysis Web Portal Version 3: Lung-at-a-Glance. American Journal of Respiratory Cell and Molecular Biology 64, 146-149.

Edvardsson, U., Ljungberg, A., Lindén, D., William-Olsson, L., Peilot-Sjögren, H., Ahnmark, A., Oscarsson, J., 2006. PPARalpha activation increases triglyceride mass and adipose differentiation-related protein in hepatocytes. J Lipid Res 47, 329-340.

Eenjes, E., Tibboel, D., Wijnen, R.M.H., Rottier, R.J., 2022. Lung epithelium development and airway regeneration. Frontiers in Cell and Developmental Biology 10.

El Agha, E.M., Alena:Kheirollahi, Vahid:De Langhe, Stijn:Crnkovic, Slaven:Kwapiszewska, Grazyna:Szibor, Marten:Kosanovic, Djuro:Schwind, Felix:Schermuly, Ralph T.:Henneke, Ingrid:MacKenzie, BreAnne:Quantius, Jennifer:Herold, Susanne:Ntokou, Aglaia:Ahlbrecht, Katrin:Braun, Thomas:Morty, Rory E.:Günther, Andreas:Seeger, Werner:Bellusci, Saverio, 2017. Two-Way Conversion between Lipogenic and Myogenic Fibroblastic Phenotypes Marks the Progression and Resolution of Lung Fibrosis. Cell stem cell 20, 261-273.e263.

Endale, M., Ahlfeld, S., Bao, E., Chen, X., Green, J., Bess, Z., Weirauch, M.T., Xu, Y., Perl, A.K., 2017. Temporal, spatial, and phenotypical changes of PDGFRα expressing fibroblasts during late lung development. Developmental Biology 425, 161-175.

Enerbäck, S., Semb, H., vernier, J.T., Bjursell, G., Olivecrona, T., 1988. Tissue-specific regulation of guinea pig lipoprotein lipase; effects of nutritional state and of tumor necrosis factor on mRNA levels in adipose tissue, heart and liver. Gene 64, 97-106.

Farbehi, N., Patrick, R., Dorison, A., Xaymardan, M., Janbandhu, V., Wystub-Lis, K., Ho, J.W., Nordon, R.E., Harvey, R.P., 2019. Single-cell expression profiling reveals

dynamic flux of cardiac stromal, vascular and immune cells in health and injury. Elife 8.

Farese, R.V., Walther, T.C., 2009. Lipid Droplets Finally Get a Little R-E-S-P-E-C-T. Cell 139, 855-860.

Fehrenbach, H., 2001. Alveolar epithelial type II cell: defender of the alveolus revisited. Respir Res 2, 33-46.

Gabbiani, G., 1992. The biology of the myofibroblast. Kidney International 41, 530-532.

Gabbiani, G., Ryan, G.B., Majne, G., 1971. Presence of modified fibroblasts in granulation tissue and their possible role in wound contraction. Experientia 27, 549-550.

Glass, D.S., Grossfeld, D., Renna, H.A., Agarwala, P., Spiegler, P., DeLeon, J., Reiss, A.B., 2022. Idiopathic pulmonary fibrosis: Current and future treatment. Clin Respir J 16, 84-96.

Green, J., Endale, M., Auer, H., Perl, A.K., 2016. Diversity of Interstitial Lung Fibroblasts Is Regulated by Platelet-Derived Growth Factor Receptor α Kinase Activity. Am J Respir Cell Mol Biol 54, 532-545.

Harkema, J.R., Nikula, K.J., Haschek, W.M., 2013. Chapter 51 - Respiratory System, in: Haschek, W.M., Rousseaux, C.G., Wallig, M.A. (Eds.), Haschek and Rousseaux's Handbook of Toxicologic Pathology (Third Edition). Academic Press, Boston, pp. 1935-2003.

Heid, H.W., Moll, R., Schwetlick, I., Rackwitz, H.R., Keenan, T.W., 1998. Adipophilin is a specific marker of lipid accumulation in diverse cell types and diseases. Cell Tissue Res 294, 309-321.

Herrero, R., Sánchez, G., Asensio, I., López, E., Ferruelo, A., Vaquero, J., Moreno, L., de Lorenzo, A., Bañares, R., Lorente, J.A., 2020. Liver–lung interactions in acute respiratory distress syndrome. Intensive Care Medicine Experimental 8, 48.

Herring, M.J., Putney, L.F., Wyatt, G., Finkbeiner, W.E., Hyde, D.M., 2014. Growth of alveoli during postnatal development in humans based on stereological estimation. American Journal of Physiology-Lung Cellular and Molecular Physiology 307, L338-L344.

Hinz, B., Phan, S.H., Thannickal, V.J., Galli, A., Bochaton-Piallat, M.L., Gabbiani, G., 2007. The myofibroblast: one function, multiple origins. Am J Pathol 170, 1807-1816.

Hinz, B., Phan, S.H., Thannickal, V.J., Prunotto, M., Desmoulière, A., Varga, J., De Wever, O., Mareel, M., Gabbiani, G., 2012. Recent Developments in Myofibroblast Biology: Paradigms for Connective Tissue Remodeling. The American Journal of Pathology 180, 1340-1355.

Imamura, M., Inoguchi, T., Ikuyama, S., Taniguchi, S., Kobayashi, K., Nakashima, N., Nawata, H., 2002. ADRP stimulates lipid accumulation and lipid droplet formation in murine fibroblasts. Am J Physiol Endocrinol Metab 283, E775-783.

Isaacson, D., Shen, J., McCreedy, D., Calvert, M., Cunha, G., Baskin, L., 2017. Dichotomous Branching of Human Fetal Lung Demonstrated with Light Sheet Fluorescence Microscopy. American journal of respiratory and critical care medicine 196, 1476-1477.

Islam, S., Kjällquist, U., Moliner, A., Zajac, P., Fan, J.B., Lönnerberg, P., Linnarsson, S., 2011. Characterization of the single-cell transcriptional landscape by highly multiplex RNA-seq. Genome Res 21, 1160-1167.

Jain, R., Barkauskas, C.E., Takeda, N., Bowie, E.J., Aghajanian, H., Wang, Q., Padmanabhan, A., Manderfield, L.J., Gupta, M., Li, D., Li, L., Trivedi, C.M., Hogan, B.L.M., Epstein, J.A., 2015. Plasticity of Hopx(+) type I alveolar cells to regenerate type II cells in the lung. Nat Commun 6, 6727.

Jersin, R., Tallapragada, D.S.P., Madsen, A., Skartveit, L., Fjære, E., McCann, A., Lawrence-Archer, L., Willems, A., Bjune, J.I., Bjune, M.S., Våge, V., Nielsen, H.J., Thorsen, H.L., Nedrebø, B.G., Busch, C., Steen, V.M., Blüher, M., Jacobson, P., Svensson, P.A., Fernø, J., Rydén, M., Arner, P., Nygård, O., Claussnitzer, M., Ellingsen, S., Madsen, L., Sagen, J.V., Mellgren, G., Dankel, S.N., 2021. Role of the Neutral Amino Acid Transporter SLC7A10 in Adipocyte Lipid Storage, Obesity, and Insulin Resistance. Diabetes 70, 680-695.

Jia, G., Chandriani, S., Abbas, A.R., DePianto, D.J., N'Diaye, E.N., Yaylaoglu, M.B., Moore, H.M., Peng, I., DeVoss, J., Collard, H.R., Wolters, P.J., Egen, J.G., Arron, J.R., 2017. CXCL14 is a candidate biomarker for Hedgehog signalling in idiopathic pulmonary fibrosis. Thorax 72, 780-787.

Jiang, D., Dey, T., Liu, G., 2021. Recent developments in the pathobiology of lung myofibroblasts. Expert Rev Respir Med 15, 239-247.

Jiang, H.P., Serrero, G., 1992. Isolation and characterization of a full-length cDNA coding for an adipose differentiation-related protein. Proc Natl Acad Sci U S A 89, 7856-7860.

Joshi, S., Kotecha, S., 2007. Lung growth and development. Early Human Development 83, 789-794.

Joyce, N.G., Alexander, D.V., 2018. Pulmonary Vascular Endothelial Cells, in: Helena, L. (Ed.), Endothelial Dysfunction. IntechOpen, Rijeka, p. Ch. 12.

Kalna, V., Yang, Y., Peghaire, C.R., Frudd, K., Hannah, R., Shah, A.V., Almagro, L.O., Boyle, J.J., Göttgens, B., Ferrer, J., Randi, A.M., Birdsey, G.M., 2019. The Transcription Factor ERG Regulates Super-Enhancers Associated With an Endothelial-Specific Gene Expression Program. Circulation Research 124, 1337-1349.

Kaplan, N.B., Grant, M.M., Brody, J.S., 1985. The lipid interstitial cell of the pulmonary alveolus. Age and species differences. Am Rev Respir Dis 132, 1307-1312.

Karvonen, H.M., Lehtonen, S.T., Harju, T., Sormunen, R.T., Lappi-Blanco, E., Mäkinen, J.M., Laitakari, K., Johnson, S., Kaarteenaho, R.L., 2013. Myofibroblast expression in airways and alveoli is affected by smoking and COPD. Respiratory Research 14, 84.

Kaushik, S., Cuervo, A.M., 2016. AMPK-dependent phosphorylation of lipid droplet protein PLIN2 triggers its degradation by CMA. Autophagy 12, 432-438.

Kim, K.K., Kugler, M.C., Wolters, P.J., Robillard, L., Galvez, M.G., Brumwell, A.N., Sheppard, D., Chapman, H.A., 2006. Alveolar epithelial cell mesenchymal transition develops in vivo during pulmonary fibrosis and is regulated by the extracellular matrix. 103, 13180-13185.

Kimani, P.W., Holmes, A.J., Grossmann, R.E., McGowan, S.E., 2009. PDGF-Rα gene expression predicts proliferation, but PDGF-A suppresses transdifferentiation of neonatal mouse lung myofibroblasts. Respiratory Research 10, 119.

Kimmel, A.R., Sztalryd, C., 2016. The Perilipins: Major Cytosolic Lipid Droplet-Associated Proteins and Their Roles in Cellular Lipid Storage, Mobilization, and Systemic Homeostasis. Annu Rev Nutr 36, 471-509.

Kinsella, J.P., Greenough, A., Abman, S.H., 2006. Bronchopulmonary dysplasia. The Lancet 367, 1421-1431.

Klein, A.M., Mazutis, L., Akartuna, I., Tallapragada, N., Veres, A., Li, V., Peshkin, L., Weitz, D.A., Kirschner, M.W., 2015. Droplet barcoding for single-cell transcriptomics applied to embryonic stem cells. Cell 161, 1187-1201.

Knust, J., Ochs, M., Gundersen, H.J., Nyengaard, J.R., 2009. Stereological estimates of alveolar number and size and capillary length and surface area in mice lungs. Anat Rec (Hoboken) 292, 113-122.

Kugler, M.C., Loomis, C.A., Zhao, Z., Cushman, J.C., Liu, L., Munger, J.S., 2017. Sonic Hedgehog Signaling Regulates Myofibroblast Function during Alveolar Septum Formation in Murine Postnatal Lung. American journal of respiratory cell and molecular biology 57, 280-293.

Leland McInnes, J.H., Nathaniel Saul, and Lukas, Großberger, 2018. UMAP: Uniform Manifold Approximation and Projection. The journal of Open Source Software.

Li, R., Bernau, K., Sandbo, N., Gu, J., Preissl, S., Sun, X., 2018a. Pdgfra marks a cellular lineage with distinct contributions to myofibroblasts in lung maturation and injury response. eLife 7, e36865.

Li, R., Bernau, K., Sandbo, N., Gu, J., Preissl, S., Sun, X., 2018b. Pdgfra marks a cellular lineage with distinct contributions to myofibroblasts in lung maturation and injury response. Elife 7.

Liao, W.P., Uetzmann, L., Burtscher, I., Lickert, H., 2009. Generation of a mouse line expressing Sox17-driven Cre recombinase with specific activity in arteries. genesis 47, 476-483.

Lignelli, E., Palumbo, F., Myti, D., Morty, R.E., 2019. Recent advances in our understanding of the mechanisms of lung alveolarization and bronchopulmonary dysplasia. Am J Physiol Lung Cell Mol Physiol 317, L832-l887.

Lindahl, P., Karlsson, L., Hellström, M., Gebre-Medhin, S., Willetts, K., Heath, J.K., Betsholtz, C., 1997. Alveogenesis failure in PDGF-A-deficient mice is coupled to lack of distal spreading of alveolar smooth muscle cell progenitors during lung development. Development (Cambridge, England) 124, 3943-3953.

Lingampally, A., Jones, M.R., Bagari, S., Chen, C., Rivetti, S., Bellusci, S., 2020. Use of the Reversible Myogenic to Lipogenic Transdifferentiation Switch for the Design of Pre-clinical Drug Screening in Idiopathic Pulmonary Fibrosis. Frontiers in Bioengineering and Biotechnology 8.

Liu, X., Rowan, S.C., Liang, J., Yao, C., Huang, G., Deng, N., Xie, T., Wu, D., Wang, Y., Burman, A., Parimon, T., Borok, Z., Chen, P., Parks, W.C., Hogaboam, C.M., Weigt, S.S., Belperio, J., Stripp, B.R., Noble, P.W., Jiang, D., 2021. Categorization of lung mesenchymal cells in development and fibrosis. iScience 24, 102551.

Löfdahl, M., Kaarteenaho, R., Lappi-Blanco, E., Tornling, G., Sköld, M.C., 2011. Tenascin-C and alpha-smooth muscle actin positive cells are increased in the large airways in patients with COPD. Respiratory Research 12, 48.

Lowe, R., Shirley, N., Bleackley, M., Dolan, S., Shafee, T., 2017. Transcriptomics technologies. PLoS Comput Biol 13, e1005457-e1005457.

Luecken, M.D., Theis, F.J., 2019. Current best practices in single-cell RNA-seq analysis: a tutorial. Molecular Systems Biology 15, e8746.

Lv, Y.-Q., Dhlamini, Q., Chen, C., Li, X., Bellusci, S., Zhang, J.-S., 2021. FGF10 and Lipofibroblasts in Lung Homeostasis and Disease: Insights Gained From the Adipocytes. Frontiers in Cell and Developmental Biology 9.

Macosko, Evan Z., Basu, A., Satija, R., Nemesh, J., Shekhar, K., Goldman, M., Tirosh, I., Bialas, Allison R., Kamitaki, N., Martersteck, Emily M., Trombetta, John J., Weitz, David A., Sanes, Joshua R., Shalek, Alex K., Regev, A., McCarroll, Steven A., 2015. Highly Parallel Genome-wide Expression Profiling of Individual Cells Using Nanoliter Droplets. Cell 161, 1202-1214.

Maksvytis, H.J., Niles, R.M., Simanovsky, L., Minassian, I.A., Richardson, L.L., Hamosh, M., Hamosh, P., Brody, J.S., 1984. In vitro characteristics of the lipid-filled interstitial cell associated with postnatal lung growth: evidence for fibroblast heterogeneity. J Cell Physiol 118, 113-123.

Maksvytis, H.J., Vaccaro, C., Brody, J.S., 1981. Isolation and characterization of the lipid-containing interstitial cell from the developing rat lung. Lab Invest 45, 248-259.

Mammoto, A., Mammoto, T., 2019. Vascular Niche in Lung Alveolar Development, Homeostasis, and Regeneration. Frontiers in Bioengineering and Biotechnology 7.

Martin, S., Parton, R.G., 2006. Lipid droplets: a unified view of a dynamic organelle. Nature Reviews Molecular Cell Biology 7, 373-378.

Martusewicz-Boros, M.M., Boros, P.W., Wiatr, E., 2013. Respiratory system involvement in chronic liver diseases. Pol Arch Med Wewn 123, 635-642.

Massaro, G.D., Massaro, D., 1996. Formation of pulmonary alveoli and gas-exchange surface area: quantitation and regulation. Annu Rev Physiol 58, 73-92.

Masuda, Y., Itabe, H., Odaki, M., Hama, K., Fujimoto, Y., Mori, M., Sasabe, N., Aoki, J., Arai, H., Takano, T., 2006. ADRP/adipophilin is degraded through the proteasome-dependent pathway during regression of lipid-storing cells. J Lipid Res 47, 87-98.

McGowan, S.E., 2014. Chapter 4 - The Formation of Pulmonary Alveoli, in: Harding, R., Pinkerton, K.E. (Eds.), The Lung (Second Edition). Academic Press, Boston, pp. 65-84.

McGowan, S.E., 2019. The lipofibroblast: more than a lipid-storage depot. American Journal of Physiology-Lung Cellular and Molecular Physiology 316, L869-L871.

McGowan, S.E., Grossmann, R.E., Kimani, P.W., Holmes, A.J., 2008. Platelet-Derived Growth Factor Receptor-Alpha-Expressing Cells Localize to the Alveolar Entry Ring and Have Characteristics of Myofibroblasts During Pulmonary Alveolar Septal Formation. The Anatomical Record 291, 1649-1661.

McGowan, S.E., Harvey, C.S., Jackson, S.K., 1995. Retinoids, retinoic acid receptors, and cytoplasmic retinoid binding proteins in perinatal rat lung fibroblasts. Am J Physiol 269, L463-472.

McGowan, S.E., McCoy, D.M., 2011. Fibroblasts expressing PDGF-receptor-alpha diminish during alveolar septal thinning in mice. Pediatr Res 70, 44-49.

McGowan, S.E., McCoy, D.M., 2013. Platelet-derived growth factor-A and sonic hedgehog signaling direct lung fibroblast precursors during alveolar septal formation. American Journal of Physiology-Lung Cellular and Molecular Physiology 305, L229-L239.

McGowan, S.E., McCoy, D.M., 2014. Regulation of fibroblast lipid storage and myofibroblast phenotypes during alveolar septation in mice. American Journal of Physiology-Lung Cellular and Molecular Physiology 307, L618-L631.

McQualter, J.L., Brouard, N., Williams, B., Baird, B.N., Sims-Lucas, S., Yuen, K., Nilsson, S.K., Simmons, P.J., Bertoncello, I., 2009. Endogenous fibroblastic progenitor cells in the adult mouse lung are highly enriched in the sca-1 positive cell fraction. Stem Cells 27, 623-633.

McQualter, J.L., McCarty, R.C., Van der Velden, J., O'Donoghue, R.J., Asselin-Labat, M.L., Bozinovski, S., Bertoncello, I., 2013. TGF-β signaling in stromal cells acts upstream of FGF-10 to regulate epithelial stem cell growth in the adult lung. Stem Cell Res 11, 1222-1233.

Meyerholz, D.K., Suarez, C.J., Dintzis, S.M., Frevert, C.W., 2018. 9 - Respiratory System, in: Treuting, P.M., Dintzis, S.M., Montine, K.S. (Eds.), Comparative Anatomy and Histology (Second Edition). Academic Press, San Diego, pp. 147-162.

Mizikova, I., Lesage, F., Cyr-Depauw, C., Cook, D.P., Hurskainen, M., Hanninen, S.M., Vadivel, A., Bardin, P., Zhong, S., Carpen, O., Vanderhyden, B.C., Thebaud, B., 2022. Single-Cell RNA Sequencing-Based Characterization of Resident Lung Mesenchymal Stromal Cells in Bronchopulmonary Dysplasia. Stem Cells 40, 479-492.

Moiseenko, A., Kheirollahi, V., Chao, C.M., Ahmadvand, N., Quantius, J., Wilhelm, J., Herold, S., Ahlbrecht, K., Morty, R.E., Rizvanov, A.A., Minoo, P., El Agha, E., Bellusci, S., 2017. Origin and characterization of alpha smooth muscle actin-positive cells during murine lung development. Stem Cells 35, 1566-1578.

Morimoto, M., Liu, Z., Cheng, H.-T., Winters, N., Bader, D., Kopan, R., 2010. Canonical Notch signaling in the developing lung is required for determination of arterial smooth muscle cells and selection of Clara versus ciliated cell fate. Journal of Cell Science 123, 213-224.

Mund, S.I., Stampanoni, M., Schittny, J.C., 2008. Developmental alveolarization of the mouse lung. Dev Dyn 237, 2108-2116.

Muzumdar, M., Tasic, B., Miyamichi, K., Li, L., Luo, L., 2007. A Global double-fluorescent Cre reporter mouse. Genesis (New York, N.Y. : 2000) 45, 593-605.

Najt, C.P., Senthivinayagam, S., Aljazi, M.B., Fader, K.A., Olenic, S.D., Brock, J.R.L., Lydic, T.A., Jones, A.D., Atshaves, B.P., 2016. Liver-specific loss of Perilipin 2 alleviates diet-induced hepatic steatosis, inflammation, and fibrosis. American Journal of Physiology-Gastrointestinal and Liver Physiology 310, G726-G738.

Nakano, Y., Kamiya, A., Sumiyoshi, H., Tsuruya, K., Kagawa, T., Inagaki, Y., 2020. A Deactivation Factor of Fibrogenic Hepatic Stellate Cells Induces Regression of Liver Fibrosis in Mice. Hepatology 71, 1437-1452.

Nikolić, M.Z., Sun, D., Rawlins, E.L., 2018. Human lung development: recent progress and new challenges. Development (Cambridge, England) 145.

Noguchi, A., Reddy, R., Kursar, J., Parks, W., Mecham, R., 1989. Smooth Muscle Isoactin and Elastin in Fetal Bovine Lung. Experimental lung research 15, 537-552.

Ntokou, A., Klein, F., Dontireddy, D., Becker, S., Bellusci, S., Richardson, W.D., Szibor, M., Braun, T., Morty, R.E., Seeger, W., Voswinckel, R., Ahlbrecht, K., 2015a. Characterization of the platelet-derived growth factor receptor-alpha-positive cell lineage during murine late lung development. Am J Physiol Lung Cell Mol Physiol 309, L942-958.

Ntokou, A., Szibor, M., Rodríguez-Castillo, J.A., Quantius, J., Herold, S., El Agha, E., Bellusci, S., Salwig, I., Braun, T., Voswinckel, R., Seeger, W., Morty, R.E., Ahlbrecht, K., 2017. A novel mouse Cre-driver line targeting Perilipin 2-expressing cells in the neonatal lung. genesis 55, e23080.

O'Hare, K.H., Sheridan, M.N., 1970. Electron microscopic observations on the morphogenesis of the albino rat lung, with special reference to pulmonary epithelial cells. American Journal of Anatomy 127, 181-205.

Pakshir, P., Noskovicova, N., Lodyga, M., Son, D.O., Schuster, R., Goodwin, A., Karvonen, H., Hinz, B., 2020. The myofibroblast at a glance. Journal of Cell Science 133.

Park, J., Ivey, M.J., Deana, Y., Riggsbee, K.L., Sörensen, E., Schwabl, V., Sjöberg, C., Hjertberg, T., Park, G.Y., Swonger, J.M., Rosengreen, T., Morty, R.E., Ahlbrecht, K., Tallquist, M.D., 2019. The Tcf21 lineage constitutes the lung lipofibroblast population. 316, L872-L885.

Peng, T., Tian, Y., Boogerd, C.J., Lu, M.M., Kadzik, R.S., Stewart, K.M., Evans, S.M., Morrisey, E.E., 2013. Coordination of heart and lung co-development by a multipotent cardiopulmonary progenitor. Nature 500, 589-592.

Petibon, C., Malik Ghulam, M., Catala, M., Abou Elela, S., 2021. Regulation of ribosomal protein genes: An ordered anarchy. Wiley Interdiscip Rev RNA 12, e1632.

Plantier, L., Boczkowski, J., Crestani, B., 2007. Defect of alveolar regeneration in pulmonary emphysema: role of lung fibroblasts. Int J Chron Obstruct Pulmon Dis 2, 463-469.

Plopper, C.G., Hyde, D.M., 2008. The non-human primate as a model for studying COPD and asthma. Pulmonary Pharmacology & Therapeutics 21, 755-766.

Rehan, V., Torday, J., 2003. Hyperoxia augments pulmonary lipofibroblast-to-myofibroblast transdifferentiation. Cell Biochem Biophys 38, 239-250.

Rehan, V.K., Sakurai, R., Corral, J., Krebs, M., Ibe, B., Ihida-Stansbury, K., Torday, J.S., 2010. Antenatally administered PPAR-gamma agonist rosiglitazone prevents hyperoxia-induced neonatal rat lung injury. Am J Physiol Lung Cell Mol Physiol 299, L672-680.

Rehan, V.K., Torday, J.S., 2007. Exploiting the PTHrP signaling pathway to treat chronic lung disease. Drugs Today (Barc) 43, 317-331.

Rehan, V.K., Wang, Y., Patel, S., Santos, J., Torday, J.S., 2006. Rosiglitazone, a peroxisome proliferator-activated receptor-γ agonist, prevents hyperoxia-induced neonatal rat lung injury in vivo. Pediatric Pulmonology 41, 558-569.

Rehan, V.K.S., Sharon:Wang, Ying:Santos, Jamie:Romero, Sonia:Dasgupta, Chiranjib:Keane, Michael P.:Stahlman, Mildred T.:Torday, John S., 2006. Evidence for the presence of lipofibroblasts in human lung. Experimental lung research 32, 379-393.

Rehan, V.K.T., John S., 2014. The lung alveolar lipofibroblast: an evolutionary strategy against neonatal hyperoxic lung injury. Antioxidants & redox signaling 21, 1893-1904.

Riccetti, M.R., Ushakumary, M.G., Waltamath, M., Green, J., Snowball, J., Dautel, S.E., Endale, M., Lami, B., Woods, J., Ahlfeld, S.K., Perl, A.T., 2022. Maladaptive functional changes in alveolar fibroblasts due to perinatal hyperoxia impair epithelial differentiation. JCI Insight 7.

Richeldi, L., Collard, H.R., Jones, M.G., 2017. Idiopathic pulmonary fibrosis. Lancet 389, 1941-1952.

Ridge, K.M., Eriksson, J.E., Pekny, M., Goldman, R.D., 2022. Roles of vimentin in health and disease. Genes & Development 36, 391-407.

Rippa, A.L., Alpeeva, E.V., Vasiliev, A.V., Vorotelyak, E.A., 2021. Alveologenesis: What Governs Secondary Septa Formation. Int J Mol Sci 22.

Rodríguez-Castillo, J.A.P., David Bravo., Ntokou, Aglaia., Seeger, Werner., Morty, Rory E., Ahlbrecht, Katrin.,2018. Respiratory Research, 2018. Understanding alveolarization to induce lung regeneration. 19, 148.

Rodriguez, L.R., Emblom-Callahan, M., Chhina, M., Bui, S., Aljeburry, B., Tran, L.H., Novak, R., Lemma, M., Nathan, S.D., Grant, G.M., 2018. Global Gene Expression Analysis in an in vitro Fibroblast Model of Idiopathic Pulmonary Fibrosis Reveals Potential Role for CXCL14/CXCR4. Scientific Reports 8, 3983.

Roth-Kleiner, M., Berger, T.M., Tarek, M.R., Burri, P.H., Schittny, J.C., 2005. Neonatal dexamethasone induces premature microvascular maturation of the alveolar capillary network. Dev Dyn 233, 1261-1271.

Saraswati, S., Marrow, S.M.W., Watch, L.A., Young, P.P., 2019. Identification of a pro-angiogenic functional role for FSP1-positive fibroblast subtype in wound healing. Nature Communications 10, 3027.

Schittny, J.C., 2017. Development of the lung. Cell and tissue research 367, 427-444.

Schniedermann, J., Rennecke, M., Buttler, K., Richter, G., Städtler, A.-M., Norgall, S., Badar, M., Barleon, B., May, T., Wilting, J., Weich, H.A., 2010. Mouse lung contains endothelial progenitors with high capacity to form blood and lymphatic vessels. BMC Cell Biology 11, 50.

Schultz, C.J., Torres, E., Londos, C., Torday, J.S., 2002. Role of adipocyte differentiation-related protein in surfactant phospholipid synthesis by type II cells. American Journal of Physiology-Lung Cellular and Molecular Physiology 283, L288-L296.

Schultz, C.J.T., E.:Londos, C.:Torday, J. S., 2002. Role of adipocyte differentiation-related protein in surfactant phospholipid synthesis by type II cells. American Journal of Physiology-Lung Cellular and Molecular Physiology 283, L288-L296.

Semrau, S., Goldmann, J.E., Soumillon, M., Mikkelsen, T.S., Jaenisch, R., van Oudenaarden, A., 2017. Dynamics of lineage commitment revealed by single-cell transcriptomics of differentiating embryonic stem cells. Nature Communications 8, 1096.

Senoo, H., Kojima, N., Sato, M., 2007. Vitamin A-storing cells (stellate cells). Vitam Horm 75, 131-159.

Silva, D.M., Nardiello, C., Pozarska, A., Morty, R.E., 2015. Recent advances in the mechanisms of lung alveolarization and the pathogenesis of bronchopulmonary dysplasia. Am J Physiol Lung Cell Mol Physiol 309, L1239-1272.

Simon, D.M., Mariani, T.J., 2007. Role of PPARs and Retinoid X Receptors in the Regulation of Lung Maturation and Development. PPAR research 2007, 91240-91240.

Skalli, O., Ropraz, P., Trzeciak, A., Benzonana, G., Gillessen, D., Gabbiani, G., 1986. A monoclonal antibody against alpha-smooth muscle actin: a new probe for smooth muscle differentiation. The Journal of Cell Biology 103, 2787 - 2796.

Smith, S.K., Burkhard, T.T., Phelps, S.M., 2021. A comparative characterization of laryngeal anatomy in the singing mouse. J Anat 238, 308-320.

Straub, B.K., Stoeffel, P., Heid, H., Zimbelmann, R., Schirmacher, P., 2008. Differential pattern of lipid droplet-associated proteins and de novo perilipin expression in hepatocyte steatogenesis. Hepatology 47, 1936-1946.

Suarez, C.J., Dintzis, S.M., Frevert, C.W., 2012. 9 - Respiratory, in: Treuting, P.M., Dintzis, S.M. (Eds.), Comparative Anatomy and Histology. Academic Press, San Diego, pp. 121-134.

Suki, B., Stamenović, D., Hubmayr, R., 2011. Lung parenchymal mechanics. Comprehensive Physiology 1, 1317-1351.

Tang, F., Barbacioru, C., Wang, Y., Nordman, E., Lee, C., Xu, N., Wang, X., Bodeau, J., Tuch, B.B., Siddiqui, A., Lao, K., Surani, M.A., 2009. mRNA-Seq whole-transcriptome analysis of a single cell. Nat Methods 6, 377-382.

Tatsumi, T., Takayama, K., Ishii, S., Yamamoto, A., Hara, T., Minami, N., Miyasaka, N., Kubota, T., Matsuura, A., Itakura, E., Tsukamoto, S., 2018. Forced lipophagy reveals that lipid droplets are required for early embryonic development in mouse. Development (Cambridge, England) 145.

Testa, U., Saulle, E., Castelli, G., Pelosi, E., 2016. Endothelial progenitor cells in hematologic malignancies. Stem Cell Investigation 3, 26-26.

Thiam, A.R., Farese Jr, R.V., Walther, T.C., 2013. The biophysics and cell biology of lipid droplets. Nature Reviews Molecular Cell Biology 14, 775-786.

Thurlbeck, W.M., 1982. Postnatal human lung growth. Thorax 37, 564-571.

Tomashefski, J.F., Farver, C.F., 2008. Anatomy and Histology of the Lung, in: Tomashefski, J.F., Cagle, P.T., Farver, C.F., Fraire, A.E. (Eds.), Dail and Hammar's Pulmonary Pathology: Volume I: Nonneoplastic Lung Disease. Springer New York, New York, NY, pp. 20-48.

Torday, J.S., Rehan, V.K., 2002. Stretch-stimulated surfactant synthesis is coordinated by the paracrine actions of PTHrP and leptin. Am J Physiol Lung Cell Mol Physiol 283, L130-135.

Torday, S.E.M.a.J.S., 1997. THE PULMONARY LIPOFIBROBLAST (LIPID INTERSTITIAL CELL) AND ITS CONTRIBUTIONS TO ALVEOLAR DEVELOPMENT. Annual Review of Physiology 59, 43-62.

Tordet, C., Marin, L., Dameron, F., 1981. Pulmonary di-and-triacylglycerols during the perinatal development of the rat. Experientia 37, 333-334.

Traag, V.A., Waltman, L., van Eck, N.J., 2019. From Louvain to Leiden: guaranteeing well-connected communities. Scientific Reports 9, 5233.

Trapnell, B.C., Nakata, K., Bonella, F., Campo, I., Griese, M., Hamilton, J., Wang, T., Morgan, C., Cottin, V., McCarthy, C., 2019. Pulmonary alveolar proteinosis. Nature Reviews Disease Primers 5, 16.

Travaglini, K.J., Nabhan, A.N., Penland, L., Sinha, R., Gillich, A., Sit, R.V., Chang, S., Conley, S.D., Mori, Y., Seita, J., Berry, G.J., Shrager, J.B., Metzger, R.J., Kuo, C.S., Neff, N., Weissman, I.L., Quake, S.R., Krasnow, M.A., 2020. A molecular cell atlas of the human lung from single-cell RNA sequencing. Nature 587, 619-625.

Treutlein, B., Brownfield, D.G., Wu, A.R., Neff, N.F., Mantalas, G.L., Espinoza, F.H., Desai, T.J., Krasnow, M.A., Quake, S.R., 2014. Reconstructing lineage hierarchies of the distal lung epithelium using single-cell RNA-seq. Nature 509, 371-375.

Tsai, T.H., Chen, E., Li, L., Saha, P., Lee, H.J., Huang, L.S., Shelness, G.S., Chan, L., Chang, B.H., 2017. The constitutive lipid droplet protein PLIN2 regulates autophagy in liver. Autophagy 13, 1130-1144.

Tschanz, S.A., Salm, L.A., Roth-Kleiner, M., Barré, S.F., Burri, P.H., Schittny, J.C., 2014. Rat lungs show a biphasic formation of new alveoli during postnatal development. Journal of Applied Physiology 117, 89-95.

Tsukui, T., Sun, K.H., Wetter, J.B., Wilson-Kanamori, J.R., Hazelwood, L.A., Henderson, N.C., Adams, T.S., Schupp, J.C., Poli, S.D., Rosas, I.O., Kaminski, N., Matthay, M.A., Wolters, P.J., Sheppard, D., 2020. Collagen-producing lung cell atlas identifies multiple subsets with distinct localization and relevance to fibrosis. Nat Commun 11, 1920.

Ubil, E., Duan, J., Pillai, I.C.L., Rosa-Garrido, M., Wu, Y., Bargiacchi, F., Lu, Y., Stanbouly, S., Huang, J., Rojas, M., Vondriska, T.M., Stefani, E., Deb, A., 2014. Mesenchymal–endothelial transition contributes to cardiac neovascularization. Nature 514, 585-590.

Ushakumary, M.G., Riccetti, M., Perl, A.-K.T., 2021. Resident interstitial lung fibroblasts and their role in alveolar stem cell niche development, homeostasis, injury, and regeneration. STEM CELLS Translational Medicine 10, 1021-1032.

Vaccaro, C., Brody, J.S., 1978. Ultrastructure of developing alveoli. I. The role of the interstitial fibroblast. Anat Rec 192, 467-479.

Varisco, B.M., Ambalavanan, N., Whitsett, J.A., Hagood, J.S., 2012. Thy-1 signals through PPARgamma to promote lipofibroblast differentiation in the developing lung. Am J Respir Cell Mol Biol 46, 765-772.

Varisco, B.M.A., Namasivayam:Whitsett, Jeffrey A.:Hagood, James S., 2012. Thy-1 signals through PPARγ to promote lipofibroblast differentiation in the developing lung. American journal of respiratory cell and molecular biology 46, 765-772.

Vaughan, A.E., Brumwell, A.N., Xi, Y., Gotts, J.E., Brownfield, D.G., Treutlein, B., Tan, K., Tan, V., Liu, F.C., Looney, M.R., Matthay, M.A., Rock, J.R., Chapman, H.A., 2015. Lineage-negative progenitors mobilize to regenerate lung epithelium after major injury. Nature 517, 621-625.

Vila Ellis, L., Chen, J., 2021. A cell-centric view of lung alveologenesis. Dev Dyn 250, 482-496.

Viola, A., Munari, F., Sánchez-Rodríguez, R., Scolaro, T., Castegna, A., 2019. The Metabolic Signature of Macrophage Responses. Frontiers in Immunology 10.

Voehringer, D., Liang, H.E., Locksley, R.M., 2008. Homeostasis and effector function of lymphopenia-induced "memory-like" T cells in constitutively T cell-depleted mice. J Immunol 180, 4742-4753.

Wang, G., Wen, B., Deng, Z., Zhang, Y., Kolesnichenko, O.A., Ustiyan, V., Pradhan, A., Kalin, T.V., Kalinichenko, V.V., 2022. Endothelial progenitor cells stimulate neonatal lung angiogenesis through FOXF1-mediated activation of BMP9/ACVRL1 signaling. Nature Communications 13, 2080.

Wang, Y., Santos, J., Sakurai, R., Shin, E., Cerny, L., Torday, J.S., Rehan, V.K., 2009. Peroxisome proliferator-activated receptor gamma agonists enhance lung maturation in a neonatal rat model. Pediatr Res 65, 150-155.

Weibel, E.R., 1979. Morphometry of the human lung: the state of the art after two decades. Bull Eur Physiopathol Respir 15, 999-1013.

Weibel, E.R., Gomez, D.M., 1962. Architecture of the Human Lung. Science 137, 577-585.

Wellman, T.J., de Prost, N., Tucci, M., Winkler, T., Baron, R.M., Filipczak, P., Raby, B., Chu, J.-H., Harris, R.S., Musch, G., Dos Reis Falcao, L.F., Capelozzi, V., Venegas, J.G., Vidal Melo, M.F., 2016. Lung Metabolic Activation as an Early Biomarker of Acute Respiratory Distress Syndrome and Local Gene Expression Heterogeneity. Anesthesiology 125, 992-1004.

Wolf, F.A., Angerer, P., Theis, F.J., 2018. SCANPY: large-scale single-cell gene expression data analysis. Genome Biology 19, 15.

Wu, X., Yang, B., Udo-Inyang, I., Ji, S., Ozog, D., Zhou, L., Mi, Q.-S., 2018. Research Techniques Made Simple: Single-Cell RNA Sequencing and its Applications in Dermatology. J Invest Dermatol 138, 1004-1009.

Xie, T., Wang, Y., Deng, N., Huang, G., Taghavifar, F., Geng, Y., Liu, N., Kulur, V., Yao, C., Chen, P., Liu, Z., Stripp, B., Tang, J., Liang, J., Noble, P.W., Jiang, D., 2018. Single-Cell Deconvolution of Fibroblast Heterogeneity in Mouse Pulmonary Fibrosis. Cell reports 22, 3625-3640.

Xie, T.W., Yizhou:Deng, Nan:Huang, Guanling:Taghavifar, Forough:Geng, Yan:Liu, Ningshan:Kulur, Vrishika:Yao, Changfu:Chen, Peter:Liu, Zhengqiu:Stripp, Barry:Tang, Jie:Liang, Jiurong:Noble, Paul W.:Jiang, Dianhua, 2018. Single-Cell Deconvolution of Fibroblast Heterogeneity in Mouse Pulmonary Fibrosis. Cell Reports 22, 3625-3640.

Yamada, M., Kurihara, H., Kinoshita, K., Sakai, T., 2005. Temporal expression of alpha-smooth muscle actin and drebrin in septal interstitial cells during alveolar maturation. J Histochem Cytochem 53, 735-744.

Yamamoto, H., Yun, E.J., Gerber, H.P., Ferrara, N., Whitsett, J.A., Vu, T.H., 2007. Epithelial-vascular cross talk mediated by VEGF-A and HGF signaling directs primary septae formation during distal lung morphogenesis. Dev Biol 308, 44-53.

Yang, J., Hernandez, B.J., Martinez Alanis, D., Narvaez del Pilar, O., Vila-Ellis, L., Akiyama, H., Evans, S.E., Ostrin, E.J., Chen, J., 2016. The development and plasticity of alveolar type 1 cells. Development (Cambridge, England) 143, 54-65.

Yuan, T.V., Thomas:Chanda,Diptiman:Thannickal,Victor J.:Langhe,Stijn P. De, 2018. Fgf10 Signaling in Lung Development, Homeostasis, Disease, and Repair After Injury. Frontiers in Genetics 9.

Zeltner, T.B., Burri, P.H., 1987. The postnatal development and growth of the human lung. II. Morphology. Respiration Physiology 67, 269-282.

Zepp, J.A., Morrisey, E.E., 2019. Cellular crosstalk in the development and regeneration of the respiratory system. Nature reviews. Molecular cell biology 20, 551-566.

Zepp, J.A., Zacharias, W.J., Frank, D.B., Cavanaugh, C.A., Zhou, S., Morley, M.P., Morrisey, E.E., 2017. Distinct Mesenchymal Lineages and Niches Promote Epithelial Self-Renewal and Myofibrogenesis in the Lung. Cell 170, 1134-1148.e1110.

Zhang, X., Lan, Y., Xu, J., Quan, F., Zhao, E., Deng, C., Luo, T., Xu, L., Liao, G., Yan, M., Ping, Y., Li, F., Shi, A., Bai, J., Zhao, T., Li, X., Xiao, Y., 2018. CellMarker: a manually curated resource of cell markers in human and mouse. Nucleic Acids Research 47, D721-D728.

Zhou, X., Zou, B., Wang, J., Wu, L., Tan, Q., Ji, C., 2022. Low expression of INMT is associated with poor prognosis but favorable immunotherapy response in lung adenocarcinoma. Front Genet 13, 946848.

Zhou, Z., Xu, M.-J., Gao, B., 2016. Hepatocytes: a key cell type for innate immunity. Cellular & Molecular Immunology 13, 301-315.

11 Appendix

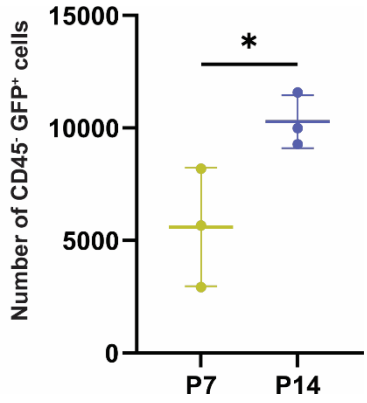

Figure S 1. Successful labeling of Plin2 lineage cells in Plin2$^{creERT2+}$; R26^{mTmG+} neonatal mouse lungs. Plin2$^{creERT2+}$; R26^{mTmG+} inducible reporter mice received an i.p. Tmx injection at P1. Lungs were harvested at P7 and P14. Using hematopoietic exclusion marker, CD45^{-}GFP^{+} cell number was quantified by flow cytometry analysis.

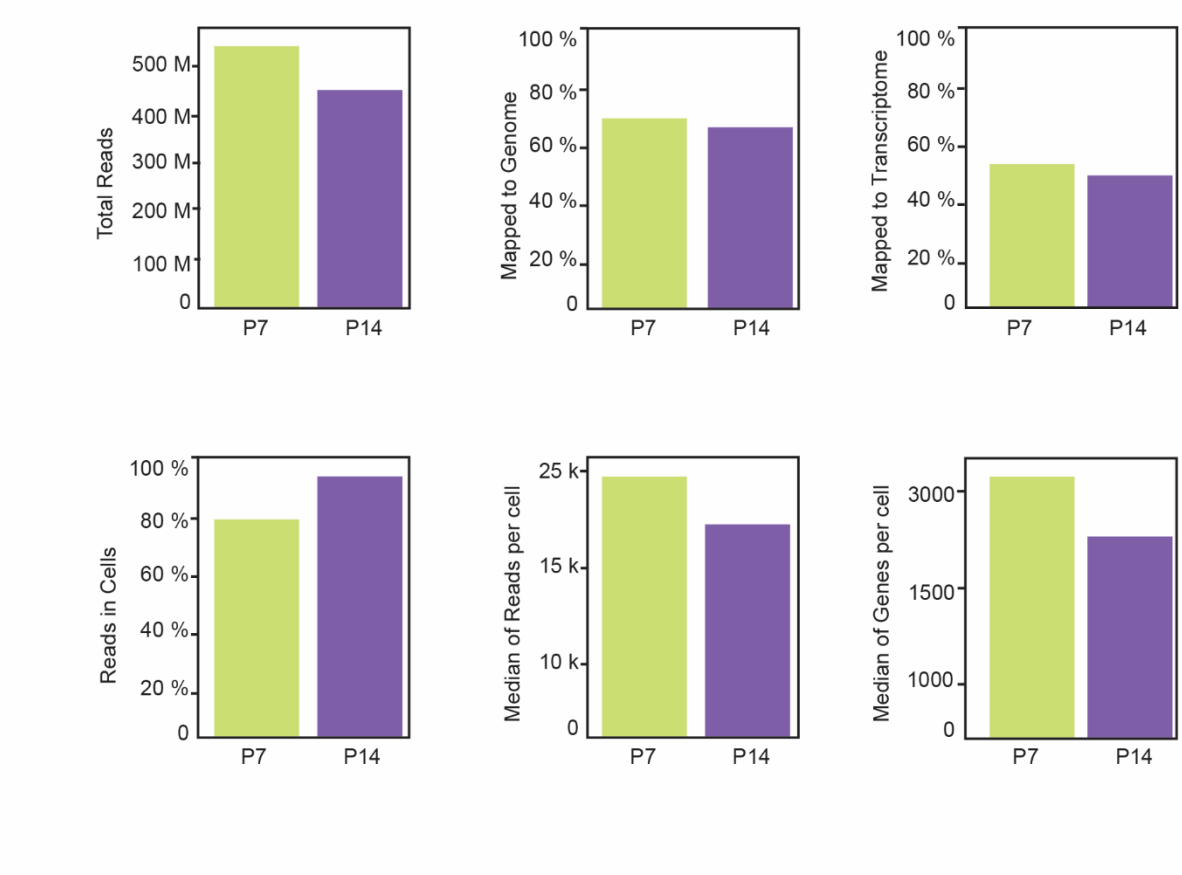

Figure S 2. General sequencing quality control metrics for scRNAseq data from P7 and P14 lungs. Data were generated by scRNAseq of Plin2^{lin} cells labeled at P1. Plin2$^{creERT2+}$; R26^{mTmG+} mice were injected with an i.p. Tmx injection at P1. Lungs were harvested at P7 and P14 and subjected to scRNAseq. Total Reads represent the number of reads per time-points. Mapped to genome states percentage of unique mapped reads (> 60 %). Mapped to transcriptome shows percentage of unique mapped reads to transcripts (low percentage hint for genomic contamination). Reads per cells demonstrates percentage of reads found in valid data-points (expected to be > 40 %; low amounts are hint for ambient RNA). Reads per cell is also the average number of read per data-point.

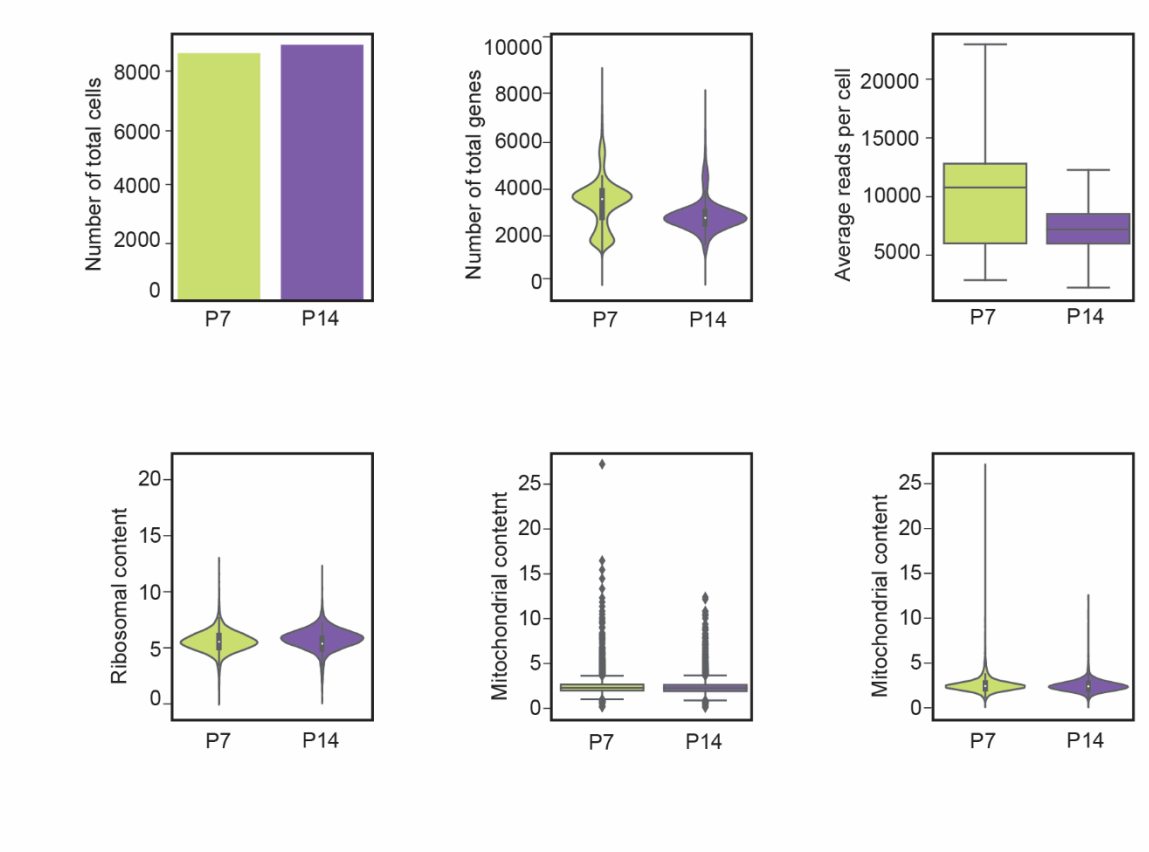

Figure S 3. StarSolo metrics of the dataset. Data were generated by scRNAseq of Plin2^{lin} cells labeled at P1. Plin2$^{creERT2+}$; R26^{mTmG+} mice were injected with an i.p. Tmx injection at P1. Lungs were harvested at P7 and P14 and subjected to scRNAseq. Total Cells represents the number of valid data-points (detected cells). Number of total genes shows the distribution of detected genes per cell by violin plot. Average reads per cell displays the distribution of obtained reads per cell by boxplots. Ribosomal content expresses the percentage of reads associated with ribosomal genes (high content indicates criteria for bad quality or cell death). Mitochondrial Content stands for percentage of reads associated with mitochondrial genes (high content indicates criteria for bad quality or cell death).

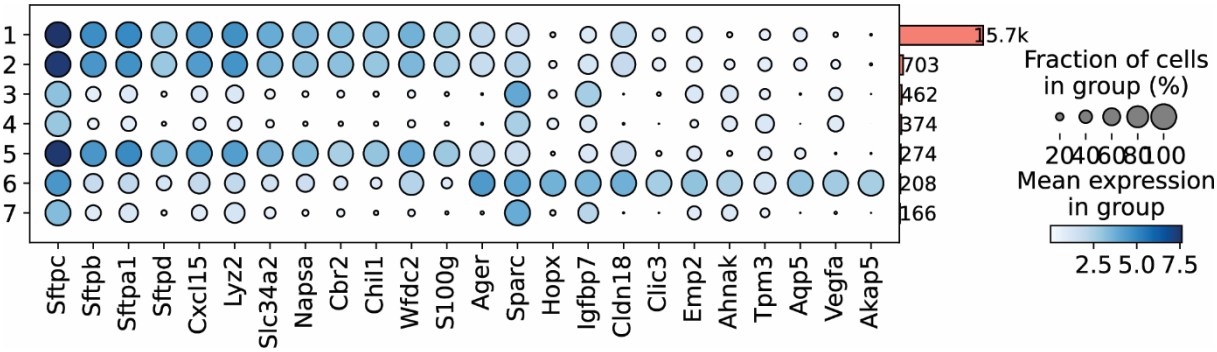

Figure S 4. Dot-plot representation of alveolar epithelial markers in 7 identified clusters. Flow cytometry on single cell suspensions from P1 labeled Plin2$^{creERT2+}$; R26^{mTmG+} mouse lungs at P7 and P14. Dot-plot represents top significantly regulated genes (q-value = 0) for identified AECs II and AECs I. The size of dots represents the relative gene expression in percentage of expressing cells for each cluster. The biggest size equals a value of 100 % that means that each cell within this cluster expressed this gene. Colors indicate the average expression level for indicated gene per cluster.

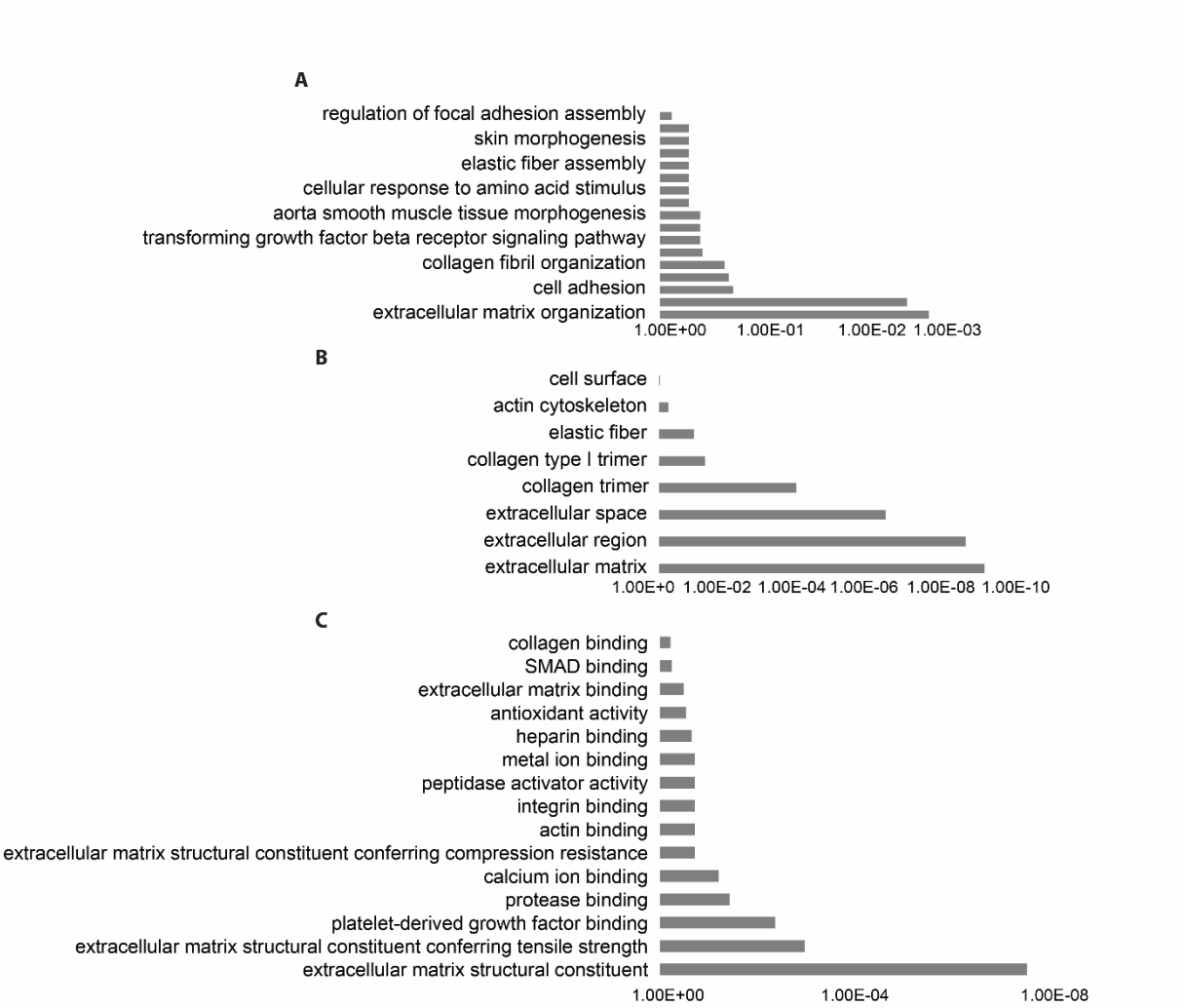

Figure S 5. Gene ontology enrichment of top 30 significantly up regulated genes in Tcf21^{high} lipofibroblast. Data were generated by scRNAseq of Plin2^{lin} cells labeled at P1 and harvested at P7 and P14 using a Plin2^{creERT2}; R26^{mTmG} mouse. Reanalysis of scRNAseq data of Plin2^{lin} cells with higher resolution revealed 11 clusters. Cluster 3 and 11 were identified as Tcf21^{low} and Tcf21^{high} lipofibroblast. (B) DEGs between Tcf21^{low} vs Tcf21^{high} were defined with FDR < 0.05. Gene ontology enrichment was performed on top 30 up regulated genes. (A) Biological process (B) Cellular compartments (C) Molecular function.

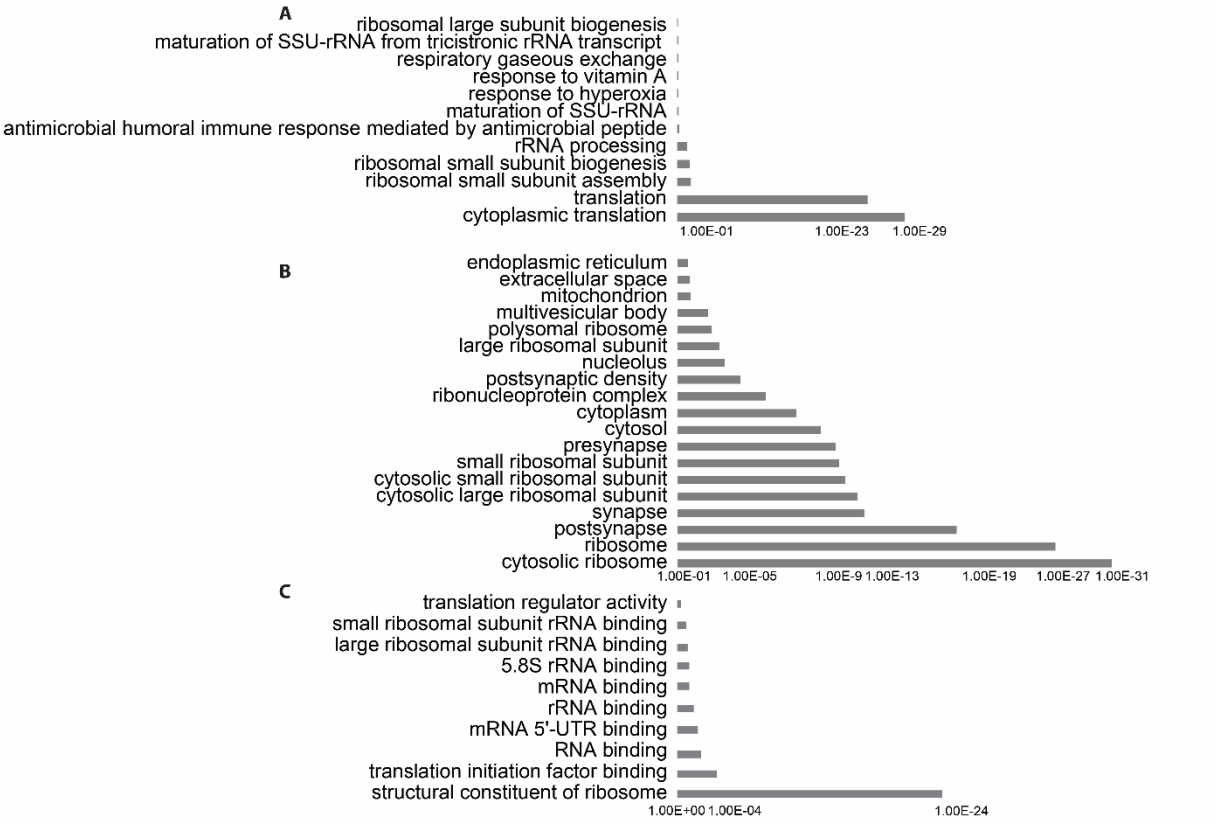

Figure S 6. Gene ontology enrichment of top 30 significantly up regulated genes in Tcf21^{low} lipofibroblast. Data were generated by scRNAseq of Plin2^{lin} cells labeled at P1 and harvested at P7 and P14 using a Plin2^{creERT2}; R26^{mTmG} mouse. Reanalysis of scRNAseq data of Plin2^{lin} cells with higher resolution revealed 11 clusters. Cluster 3 and 11 were identified as Tcf21^{low} and Tcf21^{high} lipofibroblasts. (B) DEGs between the Tcf21^{low} vs Tcf21^{high} cluster were defined with FDR < 0.05. Gene ontology enrichment was performed on top 30 up regulated genes. (A) Biological process (B) Cellular compartments (C) Molecular function. (A) Biological process (B) Cellular compartments (C) Molecular function.

12 List of figures

Figure 1. Lung development. 7
Figure 2. Schematic illustration of diseases with aberrant morphology of the alveolar region. Adopted from 9
Figure 3. Interstitial lung fibroblasts and their role in alveolar septation and epithelial niche formation..... 11
Figure 4. Mesenchymal cell-types in distal lung during alveolarization. 15
Figure 5. Construct of Plin2$^{tm1.1\ (Cre/ERT2)\ Mort}$ mice. 27
Figure 6. Schematic diagram of the mTmG construct before and after Cre activation..... 28
Figure 7. Scheme of induction of cre-recombination in a depleter mouse. 29
Figure 8. Scheme of induction of cre-recombination in a reporter mouse. 29
Figure 9. Assessment of structural changes in neonatal mouse lung of Plin2^{+} cell depleted and control mice..... 41
Figure 10. Assessment of structural changes in neonatal mouse liver Plin2^{+} cell depleted and control mice. 42
Figure 11. Assessment of structural changes in neonatal mouse kidney of Plin2^{+} cell depleted and control mice. 43
Figure 12. Assessment of structural changes in neonatal mouse spleen of Plin2^{+} cell depleted and control mice. 44
Figure 13. Quantification of mCherry^{+} cells from lungs of postnatal Plin2+ cell depleted and control mice. significant. 45
Figure 14. Assessment of fibroblast-related gene expression in postnatal lungs of Plin2^{+} cell depleted and control mice. 46
Figure 15. Assessment of gene expression of inflammatory and apoptotic processes in postnatal lungs of Plin2^{+} cell depleted and control mice. 47
Figure 16. Assessment of fibroblast-related gene expression in postnatal livers of Plin2^{+} cell depleted and control mice. 49
Figure 17. Assessment of gene expression of inflammatory and apoptotic processes in postnatal livers of Plin2^{+} cell depleted and control mice.. 50
Figure 18. Macroscopic phenotype of adult mouse organs after Tmx injection in Plin2^{+} cell depleted and control mice. Plin2^{cre+}; R26^{DTA+} and 51
Figure 19. Assessment of elastin deposition in the adult mouse lung of Plin2^{+} cell depleted and control mice 52
Figure 20. Assessment of structural changes in organs of Plin2^{+} cell depleted and control adult mice. 53
Figure 21. Cre recombination in Plin2$^{creERT2+}$; R26^{mTmG+} adult mice.. 54

Figure 22. Experimental design for lineage tracing of Plin2 cells of the Plin2 cell lineage during alveolarization. 55
Figure 23. Single cell RNA sequencing of cells of the Plin2 cell lineage during alveolarization. 57
Figure 24. Classification of postnatal Plin2^{lin} cells by scRNAseq....58
Figure 25. Contribution of the Plin2^{lin} to alveolar epithelial cell populations in the lung during alveolarization. 60
Figure 26. Confirmation of Plin2^{lin} cell contribution to alveolar epithelial type II cells during alveolarization. 61
Figure 27. Confirmation of Plin2^{lin} cell contribution to alveolar epithelial type I cells during alveolarization. 62
Figure 28. Expression of alveolar epithelial cell markers by Plin2^{lin} cells during the course of late lung development. 63
Figure 29. Existence of Plin2-expressing alveolar epithelial cells in a wild type lung at P1. ..65
Figure 30. Gene expression analysis of Plin2^{lin} cells at the peak of alveolarization. 66
Figure 31. Gene expression analysis of non-mesenchymal Plin2^{lin} derived endothelial and epithelial populations during alveolarization. 67
Figure 32. Plin2^{lin} comprises endothelial cell populations during alveolarization. 69
Figure 33. Plin2^{lin} contributed to a myofibroblast population during alveolarization. 72
Figure 34. Localization of Plin2^{lin} derived myofibroblasts in the postnatal lung....73
Figure 35. Molecular signatures and cellular localization of Plin2^{lin} derived lipofibroblasts during alveolarization. 74
Figure 36. Plin2 expression in Plin2^{lin} cells during the course of late lung development....76
Figure 37. Plin2^{lin} deciphers two LIF subpopulations during alveolarization. 77
Figure 38. New potential candidates to target lipofibroblast populations. 79
Figure S 1. Successful labeling of Plin2 lineage cells in Plin2$^{creERT2+}$; R26^{mTmG+} neonatal mouse lungs. 108
Figure S 2. General sequencing quality control metrics for scRNAseq data from P7 and P14 lungs. 109
Figure S 3. StarSolo metrics of the dataset. 110
Figure S 4. Dot-plot representation of alveolar epithelial markers in 7 identified clusters. ...111
Figure S 5. Gene ontology enrichment of top 30 significantly up regulated genes in Tcf21^{high} lipofibroblast. 112
Figure S 6. Gene ontology enrichment of top 30 significantly up regulated genes in Tcf21^{low} lipofibroblast. 113

13 List of tables

Table. 1. Comparative respiratory system in human and mice. 6
Table 2. Commonly used markers to distinguish different populations of fibroblasts during alveolarization. 14
Table 3. Name of equipment, devices, and manufacturer 21
Table 4. Name of consumables and the manufacturer 22
Table 5. Name of reagents, drugs and the manufacturer. 23
Table 6. Name of the software and the manufacturer 25
Table 7. Name of primary/secondary antibodies, catalog number, host, conjugate and company name. 26
Table 8. Primers used to amplify genomic DNA for genotyping. 30
Table 9. Components used to amplify genomic DNA for genotyping. 31
Table 10. PCR cycling protocols for genotyping transgenic mice 32
Table 11. Reverse transcription procedure to prepare cDNA from mRNA 34
Table 12. PCR reaction mix used to prepare cDNA for gene expression analysis 34
Table 13. RT-qPCR cycling conditions 35
Table 14. List of primers used for RT-qPCR analysis 35

14 List of gene names

Acta2	Actin alpha 2
Apln	Apelin
Aspm	Abnormal spindle microtubule assembly
Aspn	Asporin
Car4	Carbonic anhydrase 4
Casp3	Cysteine-aspartic acid protease 3
Casp8	Cysteine-aspartic acid protease 8
CD31	Platelet endothelial cell adhesion molecule
CD45	Protein tyrosine phosphatase, receptor type C
Cdh1	Cadherin 1
Cdh5	Cadherin 5 (CDH5)
Col13a1	Collagen, type XIII, alpha 1
Col1a1	Colagen type 1 α 1
Cxcl14	Chemokine (C-X-C motif) ligand 14
Des	Desmin
Eln	Elastin
Epcam	Epithelial cell adhesion molecule
Fabp4	Fatty acid binding protein4
FGF10	Fibroblast growth factor 10
Fn1	Fibronectin 1
G0s2	G0/G1 switch gene 2
Gli1	Fibroblast growth factor 10
Hipp	Heavy metal binding protein HIPP-like
Hsd11b1	Hydroxysteroid 11-beta dehydrogenase 1
Icam2	Intercellular adhesion molecule 2
Inmt	Indolethylamine N-methyltransferase
Lox	Lysyl oxidase
Lpl	Lipoprotein lipase
Mgp	Matrix Gla protein
Mustn1	Musculoskeletal, embryonic nuclear protein 1
Parp1	Poly ADP-Ribose polymerase 1
Pdgf	Platelet-derived growth factor binding
Pdgfa	Platelet derived growth factor A
Pdgfra(α)	Platelet derived growth factor receptor A
Pdpn	Podoplanin
Plin2	Perilipin 2
Polr2A	RNA polymerase II
Pparg	Peroxisome proliferator activated receptor gamma
Pthrp	Parathyroid hormone-related protein
Ptprc	Protein tyrosine phosphatase receptor type C
Sftpc	Surfactant associated protein C
Shh	Sonic hedgehog
Slc7a10	Solute carrier family 7 , member 10

Tagln	Transgelin
Tbx2	T-box 2
Tbx4	T-box 4
Tcf21	Transcription factor 21
TGF	Transforming growth factors
TGFBR	Transforming growth factor-beta receptor
TGF-β	Transforming growth factor-beta
Thy1	Thymus cell antigen 1
Tnc	Tenascin C
Vegfa	Vascular endothelial growth factor A
Vim	Vimentin
Wnt	Wingless-type MMTV integration site family
Zfp423	Zinc finger protein 423
α-SMA	α-smooth muscle actin (Acta2)

15 Abbreviations

AEC	Alveolar epithelial cells
AECs	Alveolar epithelial cells
APC	Allophycocyanin
bp	Base pairs
BPD	Bronchopulmonary dysplasia
BSA	Bovine serum albumin
BW	Body weight
CD	Cluster of differentiation
cDNA	Complementary DNA
CLSM	Confocal laser scanning microscopy
CMV	Cytomegalovirus enhance
COPD	Chronic obstructive pulmonary disease
Cre	Cre recombinase
Ct	Cycle threshold
Cy7	Cyanine®7
DAPI	4′,6 Diamidino-2-phenylindole
ddH2O	Double distilled water
DEG	Differentially expressed gene
DNA	Deoxyribonucleic acid
DNase	Deoxyribonuclease I from bovine pancreas
dNTP	Deoxynucleotide triphosphates
DTA	Diphtheria toxin A
E	Embryonic day
EC	Endothelial cell
ECM	Extracellular matrix
eGFP	Endogenous green fluorescent protein
Etbr	Ethidium bromide
FACS	Fluorescent activated cell sorting
FC	Fold change
FCS	Fetal calf serum
FITC	Fluorescein isothiocyanate
FMO	Fluorescence minus one
FSC-A	Forward scatter area
FSC-H	Forward scatter height
g	Gram
h	Hours
HEPES	4-(2-Hydroxyethyl)-1-piperazineethanesulfonic acid
i.p.	Intraperitoneal
IF	Immunoflourescent
ILD	Interstitial lung disease
IPF	Idiopathic pulmonary fibrosis
kg	Kilogram
LIF	Lipofibroblast

LIFs	Lipofibroblasts
loxP	Locus of X-over P1 bacteriophage
MAX	Maximun intensity projection
MF	Myofibroblast
MFs	Myofibroblasts
mg	Milligram
mG	N-terminal membrane-tagged enhanced green fluorescent protein
min	Minute
ml	Milliliter
mM	Millimolar
M-MLV	Moloney Murine Leukemia Virus
mRNA	Messenger RNA
mT	N-terminal membrane-tagged tdTomato
Mut	Mutant
ng	Nanogram
P	Postnatal day
P/S	Penicillin-Streptomycin
PA	Polyadenylation signal
PBS	Phosphate buffered saline
PCA	CMV enhancer/chicken beta-actin core promoter
PCLS	Precision-cut lung slices
PE	Phycoerythrin
PFA	Paraformaldehyde
QC	Quality control
qPCR	Quantitative polymerase chain reaction
RNA	Ribonucleic acid
RPG	Robosomal protein gene
RT	Room temperature
RTqPCR	Real time qPCR
s	Second
S	Supplementary
scRNAseq	Single cell RNA sequencing
SD	Standard deviation
SMCs	Smooth muscle cells
SSC-A	Side scatter area
T2A	Thosea asigna virus 2A
tdTomato	tandem dimer tomato
Tmx	Tamoxifen
U	Unit
UMAP	Uniform manifold approximation and projection
UMI	Unique molecular identifier
vs	Versus
Wt	Wild type
ΔCt	Difference in Ct values
(-)	Negative
(+)	Positive

°C	Degree celsius
µl	Microliter
µM	Micromolar
2D	2 Dimension
3D	3 Dimension

The curriculum vitae was removed from the electronic version of the paper.

Der Lebenslauf wurde aus der elektronischen Version der Arbeit entfernt.

16 Acknowledgments

Throughout this incredible journey, I have been fortunate to encounter remarkable people whose assistance, encouragement, and advice have made the successful completion of this endeavor possible.

Foremost, I express my deep gratitude to my esteemed academic supervisor, Dr. Katrin Ahlbrecht. Her invaluable guidance, patience and support have been instrumental in navigating the challenges of my research project.

I would also like to extend my sincere thanks to Prof. Dr. Rory E. Morty for graciously allowing me to join his esteemed lab and providing me with the opportunity to conduct my research. Additionally, I am immensely grateful to Prof. Dr. Werner Seeger for granting approval for this project.

Furthermore, I am indebted to Prof. Dr. Ivan Manzini for kindly accepting the role of my thesis supervisor, offering valuable insights throughout the process.

Acknowledgment is due to the dedicated staff of the animal facility, particularly Kevin Wilson and Tanja Enders. Their sustained support and cooperation have been vital to the success of my work. I am also thankful to Ann Atzberger and Kikhi Khrievono for their invaluable technical assistance with flow cytometry.

I would like to extend my gratitude to all current and former colleagues and friends from the Morty lab, whose support has been immeasurable. A special thanks to Alberto, Despoina, Claudio, Francisco, David Bravo, Ettore, Francesco, and Reshma. I consider myself incredibly fortunate to have had such exceptional individuals as my lab mates throughout this challenging yet rewarding journey. I will deeply miss the cherished moments we shared together.

My heartfelt appreciation goes to my parents, whose emotional support and encouragement have been invaluable throughout my Ph.D. journey. Their guidance and trust in me have played an irreplaceable role in my achievements.

Behnam, my beloved husband, your love and unwavering support have been a constant source of strength and motivation. Despite being physically distant, you have been present with me in every moment; holding my hand through the most difficult times, instilling hope within me, and helping me rise above challenges. I am eternally grateful for your presence in my life. Du bist mein ein und alles und ich liebe dich.

17 Declaration

I declare that I have completed this dissertation single-handedly without the unauthorized help of a second party and only with the assistance acknowledged therein. I have appropriately acknowledged and referenced all text passages that are derived literally from or are based on the content of published or unpublished work of others, and all information that relates to verbal communications. I have abided by the principles of good scientific conduct laid down in the charter of the Justus Liebig University of Giessen in carrying out the investigations described in the dissertation.

Solmaz Khaghani Raziabad